

Thesis for Degree of Doctor of Philosophy

**Synthesis and Characterization of Flattened  
CNTs and Graphene Nanoribbons and the  
FET-Device Fabrication**

(平坦化カーボンナノチューブおよびグラフェン  
ナノリボンの合成および評価と FET デバイス作製)

Qing WANG

王 青

Department of Chemistry  
Graduate School of Science  
Nagoya University

2015



## Abstract

Size and shape can strongly affect the properties of nanomaterials. It was found that reduction of graphene width down to several tens of nanometers by the fabrication of graphene nanoribbons (GNRs) can open the bandgap of graphene. The development of simple, low-cost mass-produced GNRs is highly necessary for the application of graphene in nanoelectronic devices. For this purpose, a mass production method of GNR analogs, fully flattened carbon nanotubes (FNTs), has been developed. In this method, solution-based extraction of large-diameter carbon nanotubes (CNTs) from multi-wall CNTs was used to produce FNTs, which were formed by spontaneous collapsing of large-diameter (most outer) CNTs. FNTs can be obtained on a bulk scale with a high yield, and the structure and surface morphology of FNTs were fully investigated. We also observed the opening of bandgaps at room temperature and the appearance of subband in the electronic structure of FNT at 9 K.

FNTs possess a unique low-dimensional inner space with a barbell-like cross section that is expressively different from cylindrical inner space of CNTs. Atoms or molecules in this new kind of inner space are enabled to align not only in one-dimensional fashion but also in two-dimensional fashion. A brand new class of FNT-based hybrid nanostructures (FNT peapods) is thus produced. The synthesis of FNT-based  $C_{60}$  nanopeapods,  $C_{60}$ @FNTs, and transmission electron microscopy (TEM)-based structural characterization of a low-dimensional array of  $C_{60}$  were performed with consistent images simulation on the basis of the multi-slice method. Furthermore, the proposed findings indicate that varieties of atoms and molecules can be intercalated in FNTs, providing the potential of preparing a new class of novel hybrid materials based on FNTs with promising properties.

The combination of precise structural characterization and electronic property measurement is essential for complete understanding of the intrinsic properties of GNRs. New experimental techniques for the fabrication of freestanding GNR devices

have been developed, leading to the simultaneous characterization of GNRs' electronic properties and atomic structure. The freestanding devices were assembled in our home-developed TEM holder for in-situ characterization, including Joule heating to purify the graphene and electronic measurements. Using electron beam sculpting and Joule heating in TEM,  $\sim 10$  nm wide GNR structures can be obtained. During the narrowing process, the conductance of GNRs behaved nonlinearly as a function of width, indicating the opening of the bandgap. The observed transport gap of 400 meV is the largest among GNRs measured through transport measurements, and this method can be used to study the intrinsic electronic properties of GNRs. The presented methodology could be used in the future to correlate the electronic properties with a known structure in two dimensional materials such as transition metal dichalcogenides.

# Contents

## Chapter 1 General Introduction

1.1 Graphene .....	1
1.1.1 Electronic structure of graphene.....	2
1.1.2 Preparation of graphene .....	4
1.2 Graphene nanoribbon .....	6
1.2.1 Calculated electronic structure of GNRs .....	7
1.2.2 Preparation and properties of GNRs.....	9
1.3 Collapsing (Flattening) of CNTs .....	11
1.4 Overview .....	13

## Chapter 2 Preparation and Characterization of Fully Flattened Carbon Nanotubes (FNTs)

2.1 Preparation of FNTs.....	20
2.1.1 Preparation method.....	20
2.1.2 Transmission electron microscope .....	21
2.2 Characterization of FNTs .....	23
2.2.1 AFM characterization of FNTs .....	24
2.2.2 Raman measurement of FNTs.....	26
2.3 H <sub>2</sub> plasma treatment of FNTs .....	28
2.3.1 Purification of FNTs .....	29
2.3.2 Edges control of FNTs.....	31
2.3 Electronic characterization of FNTs .....	34

2.3.1 Preparation of marks.....	34
2.3.3 Preparation of FNTs devices.....	35
2.3.4 Electrical measurement of FNTs devices .....	37
2.4 Conclusions .....	40

### **Chapter 3 Synthesis and TEM Structural Characterization of C<sub>60</sub>-Flattened CNT Nanopeapods**

3.1 Preparation of FNTs and inner space investigation .....	44
3.1.1 Preparation of FNTs .....	44
3.1.2 Investigation of inner space of FNTs .....	45
3.2 Encapsulation of C <sub>60</sub> in FNTs.....	47
3.2.1 Encapsulation conditions .....	47
3.2.2 H <sub>2</sub> plasma treatment.....	48
3.3 Structure analysis .....	49
3.3.1 One dimensional packing.....	49
3.3.2 Two dimensional packing .....	51
3.3.3 Other kinds of packing.....	54
3.4 Conclusions .....	55

### **Chapter 4 Fabrication and In-situ TEM Characterization of Freestanding Graphene Nanoribbons Devices**

4.1 Fabrication of freestanding graphene devices .....	59
4.1.1 Preparation of graphene .....	59
4.1.2 Patterning on graphene .....	62
4.2 Fabrication of graphene devices .....	64

4.3 Preparation of freestanding structures.....	66
4.3.1 Laser etching .....	66
4.3.2 HF etching.....	68
4.4 In-situ TEM characterization of freestanding structures.....	73
4.4.1 Preparation for in-situ TEM characterization .....	73
4.4.2 Focused electron beam sculpting .....	74
4.4.3 Joule heating and electrical measurement.....	77
4.5 Conclusions .....	79
<b>Conclusions .....</b>	<b>84</b>
<b>Acknowledgments .....</b>	<b>86</b>
<b>List of Publications .....</b>	<b>88</b>



# Chapter 1

## General Introduction

Carbon is the fourth most abundant element in the universe by mass after hydrogen, helium, and oxygen. Several allotropes of carbon exist, and the physical properties of carbon vary widely with the allotropic form. Zero-dimensional (0D) fullerene, one-dimensional (1D) carbon nanotubes, two-dimensional (2D) graphene and three-dimensional (3D) diamonds and graphite constitute the entire carbon material family. The existence of graphene has been theoretically proposed for decades until it was first measurably produced by A. K. Geim and K. S. Novoselov in 2004 [1]. Because of their groundbreaking experiments on the two-dimensional graphene materials, the Nobel Prize in Physics was awarded to them in 2010. In the following decade, graphene has attracted intense interest because of its extraordinary properties, such as strength that is approximately 200 times higher than steel, remarkably efficient thermal and electric conductivities and near transparency.

### 1.1 Graphene

Graphene is an atomic-scale carbon film with hexagonal lattice in which one atom forms each vertex. It can be considered as the basic structural element of the other graphitic allotropes such as graphite, carbon nanotubes, and fullerenes [2]. The intrinsic graphene has the ideal 2D crystalline structure in which every carbon atom is densely packed with the other three carbon atoms by very tight  $\sigma$  bonds. The C-C bonds make the graphene layer structure very rigid and strong. The carbon atoms of graphene contribute to the non-bonding  $\pi$  electron that forms the  $\pi$  orbital in the direction perpendicular to the plane. The  $\pi$  electron freely moves in the crystal, giving rise to the highly efficient electric conductivity of graphene.

The carbon-based 2D crystal graphene can be considered to be the basic unit of  $sp^2$

hybrid carbon materials, which can then be used to build 0D fullerene, 1D carbon nanotube and 3D graphite. Graphene can be wrapped up into 0D fullerene if there are more than 12 pentagonal crystal lattices or rolled into 1D nanotube or stacked into 3D graphite through the interactions of planar hexagonal meshes.

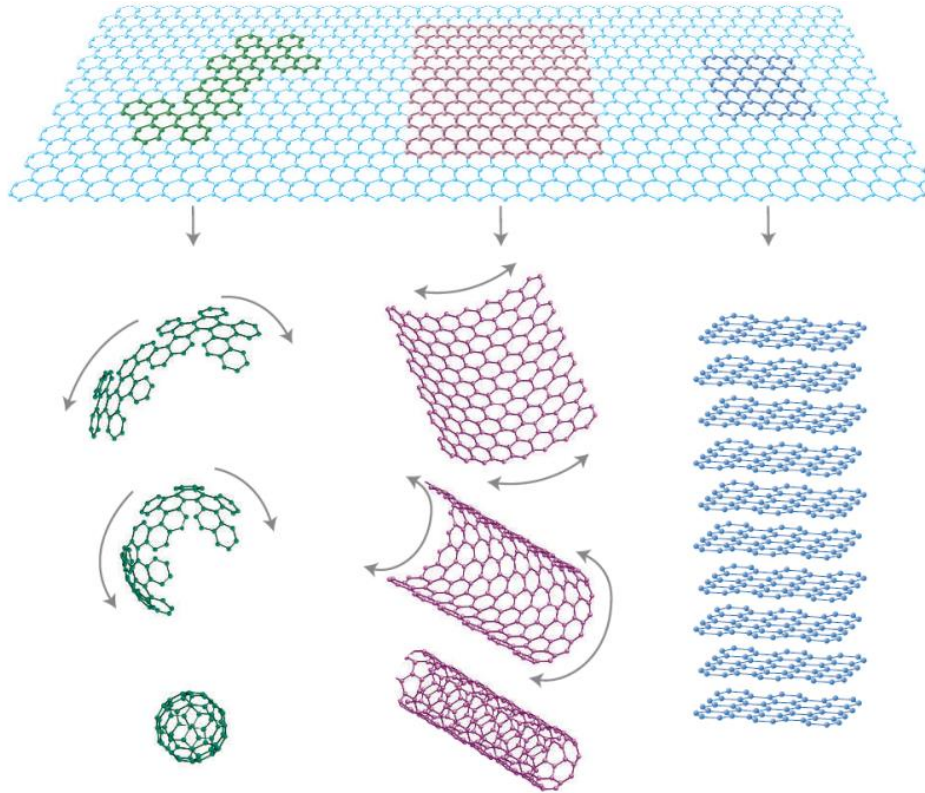


**Figure 1.1** Mother of all graphitic forms. Graphene is a two-dimensional building material for carbon materials of all other dimensionalities [2].

### 1.1.1 Electronic structure of graphene

The electronic band structure of graphene exhibits a linear dispersion around the points in the Brillouin zone where the valence band ( $\pi$ ) touches the conduction band ( $\pi^*$ ) touch [3]. These points are known as the Dirac points. In the momentum space of graphene, there are six locations (the Dirac points) found on the edge of the Brillouin zone, and two non-equivalent sets of three points are defined in the six Dirac points. The two sets are labeled K and K' as shown in Figure 1.2, which shows the energy

dispersion of graphene obtained within the tight-binding approximation.

Graphene is a zero-gap semiconductor and has unique carrier characteristics. The interaction between its electron and lattice-periodic potential of the honeycomb crystal produces a zero density of Dirac fermions (massless Dirac fermions), a type of quasiparticles with characteristics similar to photons. At room temperature, graphene has 10 times higher carrier mobility than commercial silicon, has ballistic transport properties, and is weakly influenced by temperature and doping [1, 4].

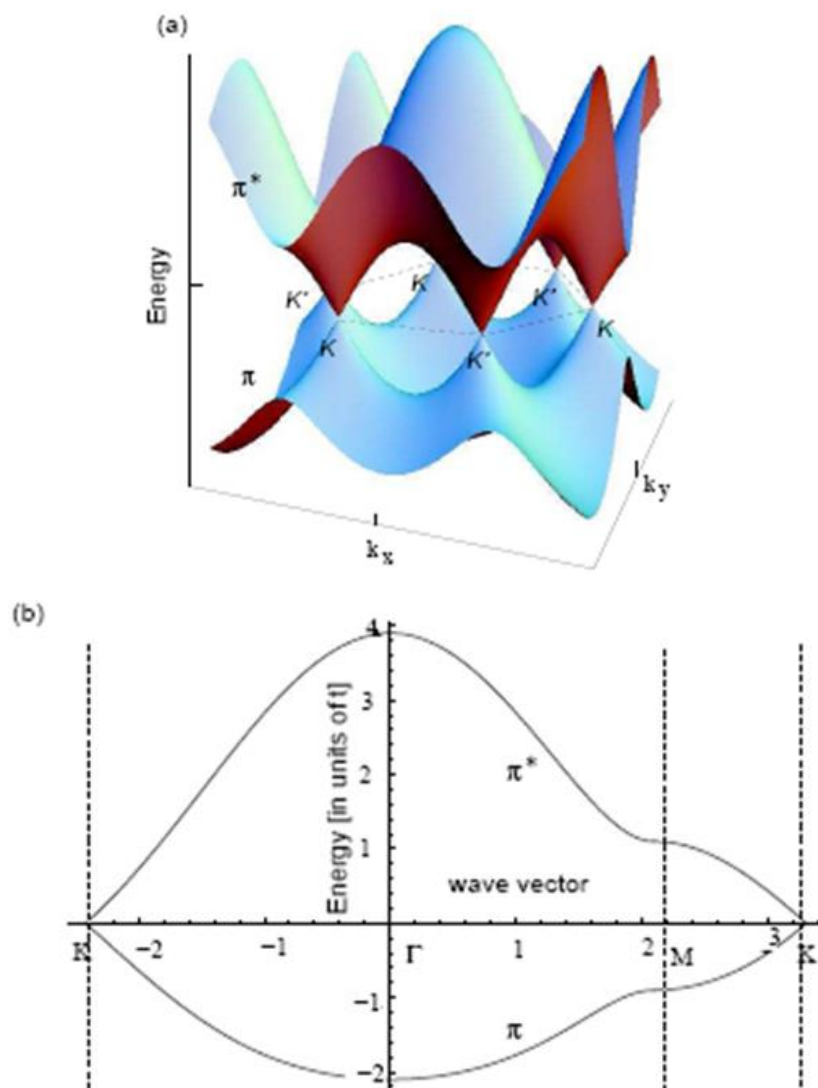


**Figure 1.2** (a) Energy dispersion as a function of the wave-vector components  $k_x$  and  $k_y$ ; (b) Cut through the energy dispersion along characteristic lines [3].

The unique band structure of graphene gives rise to hole and electron separation, generating the irregular quantum hall effect and other fascinating electronic effects. K. S. Novoselov *et al.* first reported the room temperature quantum hall effect of graphene, which expanded the original temperature range of the effect by a factor of 10 [5]. N. Tombro *et al.* studied the electronic spin transport and Larmor precession over micrometer-scale distances in graphene and observed clear bipolar spin signal, which slightly changed at 4.7K, 77K and room temperature. They extracted a spin relaxation length of 1.5 to 2 $\mu$ m and showed that is weakly dependent on charge density, enabling possible applications of graphene high-frequency transistors [6]. Furthermore, H. B. Heersche *et al.* observed a supercurrent at zero charge density, demonstrating that graphene has unique superconducting properties [7]. While graphene is clearly a remarkable material that impacts on basic science and applications its zero-bandgap prevents its possible application in nanoelectronics.

### **1.1.2 Preparation of graphene**

Graphene was first experimentally produced by mechanical exfoliation in 2004, using Scotch tape and highly oriented pyrolytic graphite (HOPG) [1]. This pioneering work opened the door to experimental studies of graphene's favorable properties and its limitations. However, it is difficult to control the size and the layers number of graphene using mechanical exfoliation. In later studies, graphene was prepared using the inductively coupled radio-frequency plasma-enhanced chemical vapor deposition method on different types of substrates on the basis of adjustments of the synthesis conditions of CNTs [8]. For example, a microwave-enhanced chemical vapor phase method was used to grow graphene on Ni-coated Si substrates [9]. In another study, taking advantage of the low solubility of carbon in copper, X. Li *et al.* produced large, continuous and controllable monolayer graphene on copper surface by chemical vapor deposition (CVD) [10]. This method is currently used for the fabrication of graphite in a wide range of laboratories.

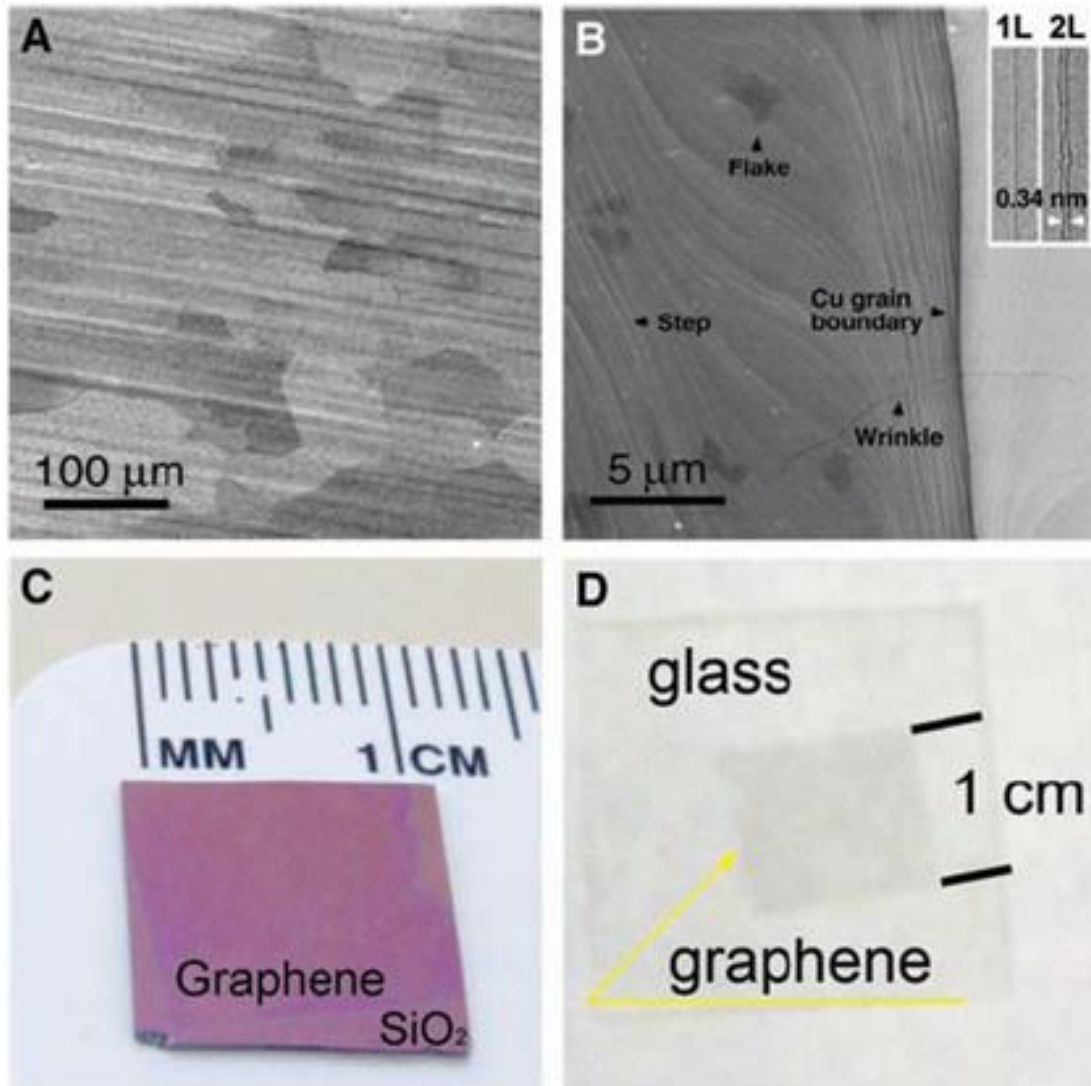


**Figure 1.3** (A) and (B) SEM images of graphene on a copper foil; (C) and (D) Graphene films transferred onto a  $\text{SiO}_2/\text{Si}$  substrate and a glass plate, respectively [10].

Epitaxial graphene was obtained by surface decomposition of SiC substrates under high vacuum heating [11]. This type of graphene exhibits high mobility but is also strongly affected by SiC substrates [12]. The organic synthesis method was also used to prepare graphene [13]. Furthermore, graphene oxide was obtained following the arc discharge of graphite, and final reduction to graphene was then performed in a suitable colloidal suspension agent [14]. The successful preparation of graphene provides the potential further study on this unique material.

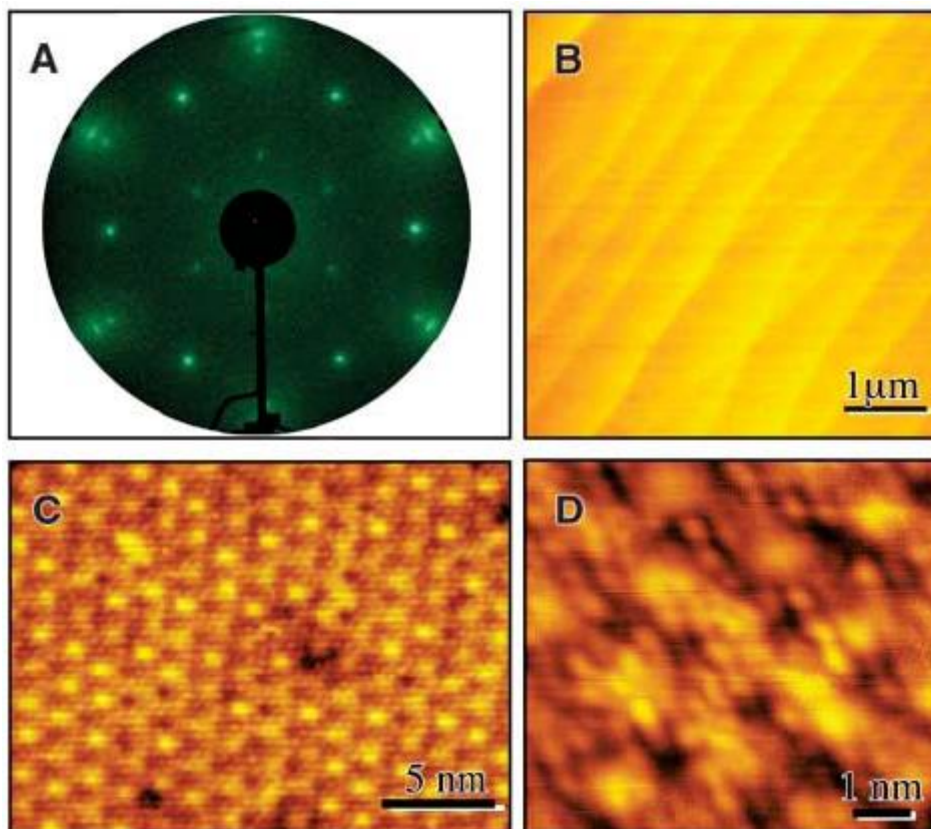


**Figure 1.4** Production and characterization of epitaxial graphene. (A) LEED pattern (71 eV) of three monolayers of epitaxial graphene on 4H-SiC (C-terminated face); (B) AFM image of graphitized 4H-SiC; (C) and (D) STM images of one monolayer of epitaxial graphene [12].

## 1.2 Graphene nanoribbon

While graphene exhibits intriguing electrical, optical, and mechanical properties and a high carrier mobility of  $>10,000\text{cm}^2\text{V}^{-1}\text{s}^{-1}$  at room temperature, the main issue for use in electronic application is the fact that graphene is a zero-gap semiconductor. Therefore, the opening of a sizable and well-defined bandgap is the prime problem for the application of graphene-based electronics. Of the several methods proposed to open the bandgap in graphene [15, 16], the narrowing of the graphene width to several tens of nanometers, i.e., the fabrication of graphene nanoribbons (GNRs), is considering to be the most promising approach to obtain a nonzero bandgap [17, 18].

The existence of bandgap is the reason why GNRs attract a wide range of attention and is also the reason for the focus of this work on GNRs.

### 1.2.1 Calculated electronic structure of GNRs

GNRs are ribbons of graphene with ultra-thin width ( $\sim 100$  nm) that can be simply visualized by cutting two straight parallel lines along the graphene sheet. Cutting along the lateral or vertical directions produces armchair GNRs (ac-GNRs) or zigzag GNRs (zz-GNRs) that exhibit armchair or zigzag side edges, respectively. The GNR width is defined as the number of dimer lines (in ac-GNRs) or zigzag chains (in zz-GNRs) denoted by  $N$  [19].

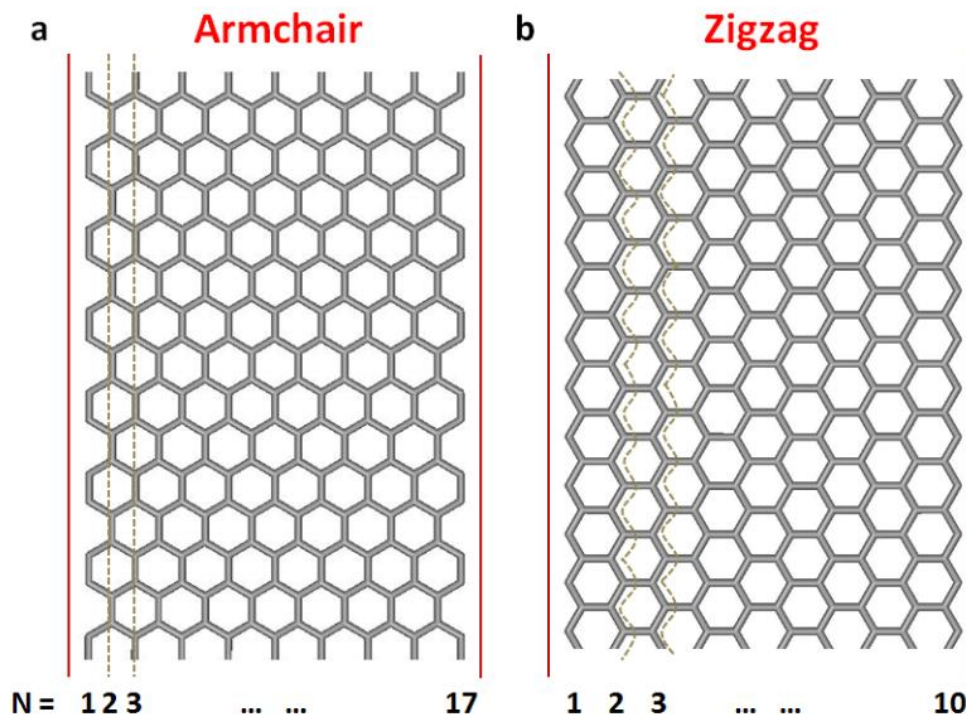


**Figure 1.5** Schematic diagrams of (a) armchair-GNR ( $N = 17$ ) and (b) zigzag-GNR ( $N = 10$ ). The dimer lines (ac-GNR) and zigzag chains (zz-GNR) were indicated by dashed grey lines.

The electronic states of GNRs largely depend on their edge structures (*i.e.* armchair,

zigzag). According to a tight-binding band calculation, ac-GNRs can be metallic or semiconducting depending on their width ( $N$ ). GNRs of size  $N$  are divided into three groups, characterized by  $N = 3M - 1$ ,  $3M$ , and  $3M + 1$ , where  $M$  is a positive integer. The calculation predicted that ac-GNRs are metallic when  $N = 3M - 1$  and other ac-GNRs are semiconducting, as shown in Figure 1.6a [19]. However, the energy bands of zz-GNRs are almost flat at the Fermi level because of a state localized on the zigzag edges and thereby give rise to a sharp peak in the density of states. The highest valence band state and the lowest conduction band for zz-GNRs are always degenerate at  $k = \pi$ , which does not originate from the intrinsic band structure of two-dimensional graphene and leads to the metallic behavior of zz-GNRs, as shown in Figure 1.6b [19].

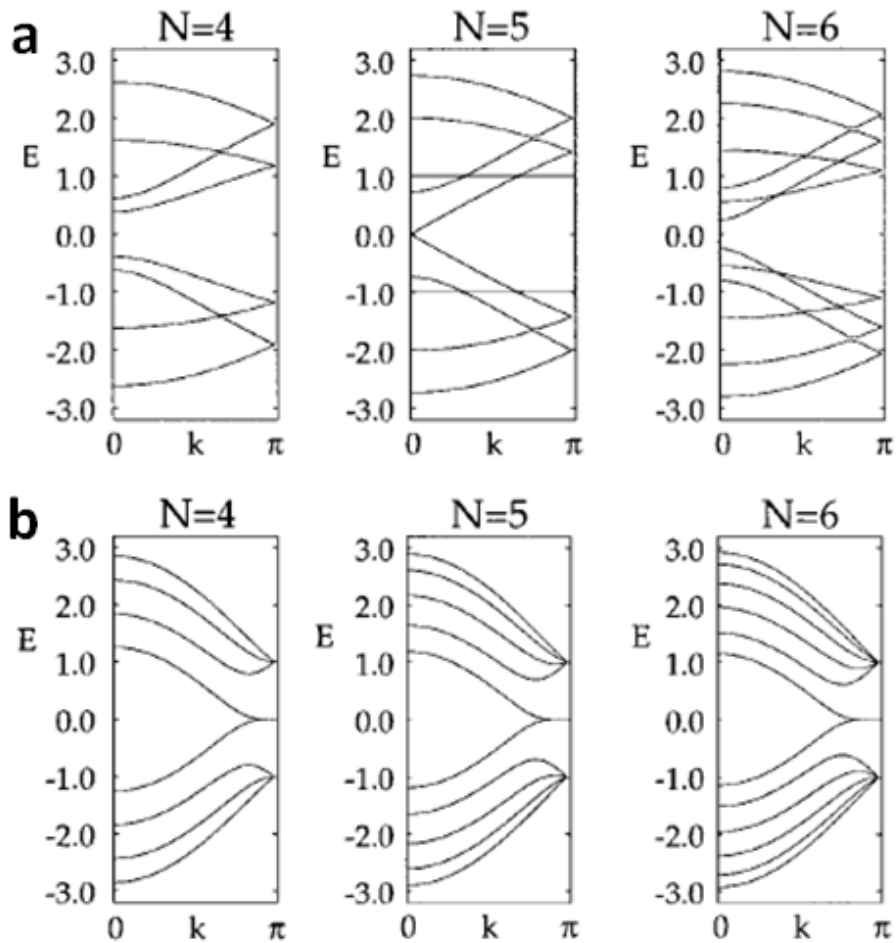


**Figure 1.6** Calculated band structure of (a) ac-GNRs and (b) zz-GNRs of various

width  $N = 4, 5, 6$  [19].

However, density functional theory (DFT) calculations show that ac-GNRs with widths of up to 8 nm are semiconducting with a possible maximum bandgap of 0.05 eV [20]. First-principles calculations show that GNRs with homogeneous armchair or zigzag edges have energy gaps that decrease with increasing width of the system [21].

## 1.2.2 Preparation and properties of GNRs

In 2007, M. Y. Han *et al.* reported energy bandgap engineering of GNRs using electron beam lithography (EBL)-patterned exfoliated graphene ribbon structures and found that the energy gap scales inversely with the ribbon width [17]. They then used the same method to study length- and width-dependent resistance scaling in GNRs [22]. Temperature- and electric field-dependent transport characteristics indicate that charge transport in the transport gap of disordered GNRs is dominated by localized states where the Coulomb charging effects play an important role.

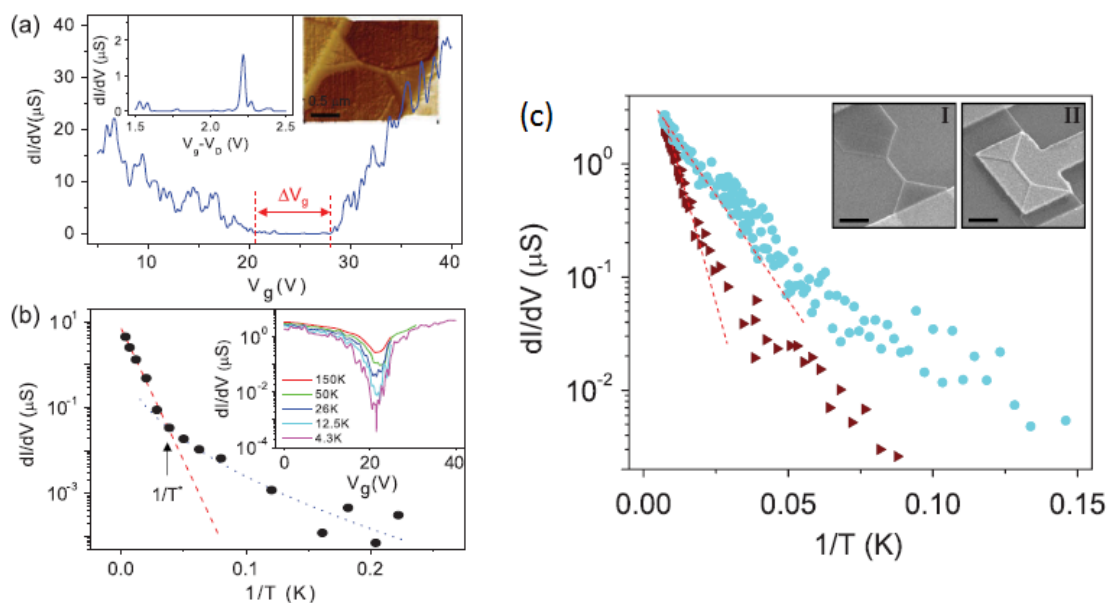


**Figure 1.7** (a)  $dI/dV$  of a GNR with Width = 36 nm and Length = 500 nm, plotted as a function of  $V_g$ . Right inset shows an AFM image of the device. Left inset shows a close-up of  $dI/dV$  within the gap regime; (b) Temperature dependence of the

minimum conductance of the same GNR in (a); (c) Temperature dependence of the minimum conductance for dual gated (circles) and back gated (triangles) GNRs with similar width and length [22].

Unzipping of CNTs is another effective method for the synthesis of GNRs by chemical reaction or sonication [23-25]. As shown in Figure 1.8, highly crystalline multi-wall carbon nanotubes were unzipped to form GNRs with ordered edges and lower defects than EBL-patterned GNRs. A large intrinsic energy bandgap of  $\sim 50$  meV was observed in GNRs with widths of  $\sim 100$  nm, which were verified to exhibit a low defect density by transmission electron microscopy (TEM) and Raman measurement [25].

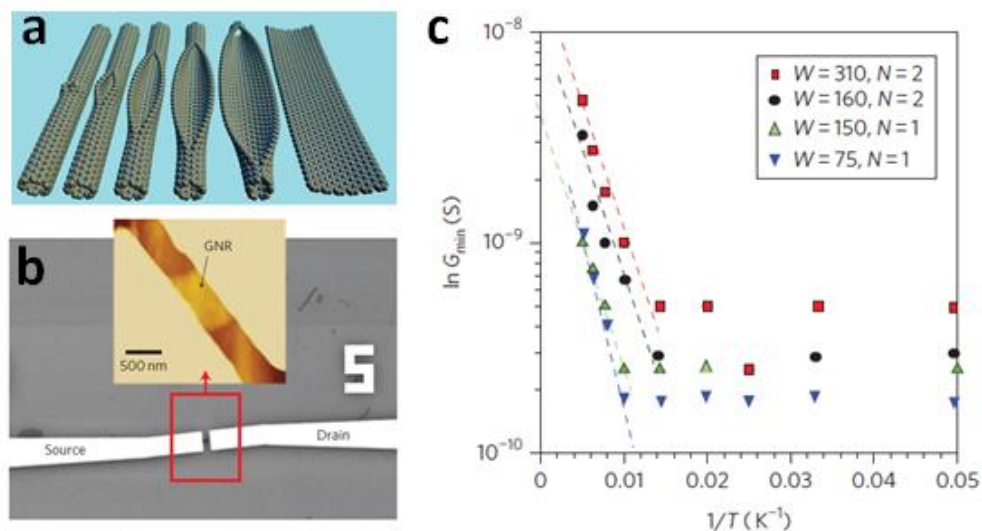


**Figure 1.8** (a) Schematic diagram of unzipping of CNTs [23]; (b) SEM and AFM images of a GNR FET device; (c) Arrhenius plot for minimum conductance versus temperature of different widths GNRs [25].

Z. J. Qi *et al.* reported correlations between atomic structure and transport in suspended GNRs [26]. They prepared EBL-patterned CVD-grown graphene for field effect transistor (FET) devices and used focused electron beam to sculpt graphene into nanoribbons in TEM. Freestanding GNRs with widths as small as 0.7 nm were studied in aberration-corrected TEM for lattice-resolution imaging and electrical

transport characterization, as shown in Figure 1.9.

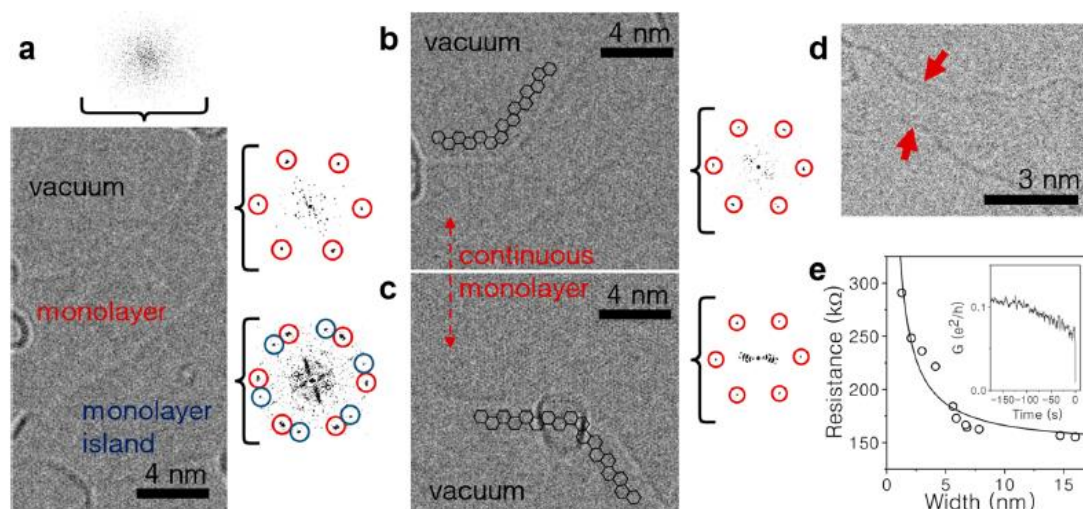


**Figure 1.9** (a) TEM image of a single-layer GNR edge immediately after nano-sculpting; (b) and (c) Evolution of (a) after current annealing; (d) TEM image of an isolated single-layer GNR ( $w = 1.3$  nm); (e) Resistance as a function of width for monolayer GNR [26].

Scanning tunneling microscope (STM) lithography was used to prepare GNRs with well-defined widths and predetermined crystallographic orientations and a so-prepared 2.5 nm wide armchair GNRs with an energy gap about 0.5 eV was reported at room temperature [27]. In addition, there are many other reports on the fabrication methods for GNRs, such as nanowire etching mask, templated growth on SiC, surface-assisted coupling of molecular precursors into linear polyphenylenes and diamond-edge-induced nanotomy of graphite [28-31].

However, the mass production of GNRs with a high yield and investigations of the intrinsic properties, such as the bandgap, for GNRs with known structures are still the main problems in the field of graphene studies.

### 1.3 Collapse (Flattening) of CNTs

The spontaneous collapse of large diameter carbon nanotubes (CNTs) has been

reported theoretically and experimentally [32-37]. It has already been predicted that the energy of hollow cylinder CNTs is higher than that of collapsed structure CNTs when the diameter tends to be near the threshold regime. The collapsed state of large-radius CNTs is stable because of the low-energy electronic properties and carbon-carbon van der Waals interaction [33]. Classical molecular dynamics simulations were used to demonstrate the limited stability for single-wall CNTs of critical diameter between 4.2 and 6.9 nm at atmospheric pressure [36].

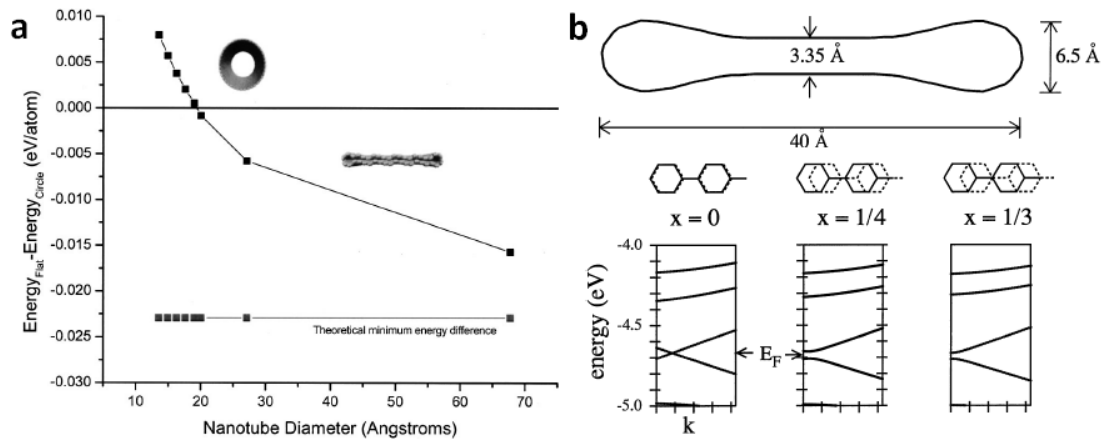


**Figure 1.10** (a) Energy difference between the round and flat configuration as a function of nanotube diameter [36]; (b) Cross section of a collapsed (20, 20) tube under zero external force as determined by tight-binding total-energy techniques, and the band structure of the collapsed tube with different lattice offsets  $\chi$  shown on the top [33].

This type of collapsed CNTs can be produced by a CVD process [38, 39]. TEM characterization of a bundle of CNTs showed a clear barbell-like cross section of collapsed CNTs that are obviously different from the round CNTs shown in Figure 1.11A [38]. Experimental and computational studies found that the energy equivalence point values (diameter at which the energies of the round and collapsed CNTs are the same) are 2.6 and 4.0 nm for the single- and double-wall CNTs shown in Figure 1.11B and 1.11C respectively [39].

The geometry of the collapsed CNTs is different from that of CNTs. Collapsed

single-wall CNTs can be considered as bilayer GNRs with smooth closed edges. The middle flat parts of collapsed CNTs are essentially similar to few-layer graphene with different stacking. Thus, collapsed CNTs are a type of GNR analog and are the same as few-layer GNRs if the closed edges are removed.

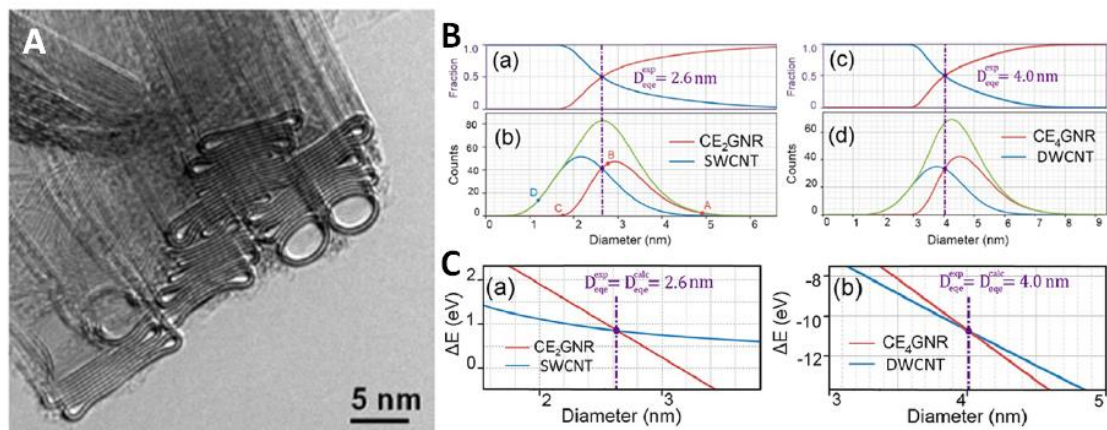


**Figure 1.11** (A) TEM image of a bundle of CNTs containing round and collapsed CNTs [38]; (B) and (C) Experimental and calculated energy equivalence point values (diameter at which the energies of the round and collapsed CNTs are the same) are 2.6 and 4.0 nm for single- and double-wall CNTs respectively [39].

## 1.4 Overview

The preparation method and intrinsic properties of GNRs have attracted intense interest in the past decade because of the edge-dependent electronic properties of GNRs. The opened bandgaps of GNRs make them promising for future applications in graphene-based electronics. Therefore, we focused on the preparation and characterization of GNRs, their analogs, and hybrid structures.

The development of simple, low-cost mass-produced GNRs is highly necessary for the application of GNRs. The fully flattened CNTs (FNTs) that are analogs of GNRs were produced by a simple solution process, as discussed in Chapter 2. The properties of FNTs were fully characterized, and the differences between FNTs and round CNTs and graphene were determined. We also used  $H_2$  plasma for purification and edge

structure control of FNTs, obtaining edge-etched FNTs with structures similar to those of few-layer GNRs. Electrical investigation of FNTs showed the opening of bandgaps and a presence of subband at very low temperatures.

FNTs have a barbell-like cross section and provide a unique low-dimensional nanospace that is dramatically different from the cylindrical inner space of CNTs. This new kind of nanospace enables atoms or molecules to align in one-dimensional and 2D fashion, producing a brand new class of FNT-based hybrid nanostructures such as FNT peapods. In Chapter 3, we demonstrated the synthesis of FNTs-based  $C_{60}$  nanopeapods ( $C_{60}@FNTs$ ) and described the structural characterization of low-dimensional  $C_{60}$  arrays on the basis of TEM observations.

The electronic structure of GNRs, including the bandgap and localized edge states, strongly depends on their width and edge structure: width-dependent bandgap and gapless edge states arise from zigzag edges. The combination of precise structural characterization and electronic property measurement is therefore essential for full understanding of the intrinsic properties of GNRs. In Chapter 4, we describe how high power laser and focused electron beam were used to narrow down freestanding graphene to a nanoribbon. The freestanding devices were assembled in a home-developed TEM holder for in-situ characterization, including Joule heating to purify the graphene and electronic measurements.

## References

1. K. S. Novoselov, A. K. Geim, S. V. Morozov, D. Jiang, Y. Zhang, S. V. Dubonos, I. V. Grigorieva, and A. A. Firsov. Electric field effect in atomically thin carbon films. *Science* **2004**, 306, 666-669.
2. A. K. Geim and K. S. Novoselov. The rise of graphene. *Nature Materials* **2007**, 6, 183-191.
3. M. O. Goerbig. Electronic properties of graphene in a strong magnetic field. *Reviews of Modern Physics* **2011**, 83, 1193-1243.
4. J. R. Williams, L. DiCarlo, C. M. Marcus. Quantum hall effect in a gate-controlled *p-n* junction of graphene. *Science* **2007**, 317, 638-641.
5. K. S. Novoselov, Z. Jiang, Y. Zhang, S. V. Morozov, H. L. Stormer, U. Zeitler, J. C. Maan, G. S. Boebinger, P. Kim, A. K. Geim. Room-temperature quantum hall effect in graphene. *Science* **2007**, 315, 1379.
6. N. Tombros, C. Jozsa, M. Popinciuc, H. T. Jonkman, B. J. van Wees. Electronic spin transport and spin precession in single graphene layers at room temperature. *Nature* **2007**, 448, 571-574.
7. H. B. Heersche, P. Jarillo-Herrero, J. B. Oostinga, L. M. K. Vandersypen, A. F. Morpurgo. Bipolar supercurrent in graphene. *Nature* **2007**, 446, 56-59.
8. J. Wang, M. Zhu, R. A. Outlaw, X. Zhao, D. M. Manos, B. C. Holloway. Synthesis of carbon nanosheets by inductively coupled radio-frequency plasma enhanced chemical vapor deposition. *Carbon* **2004**, 42, 2867-2872.
9. S. K. Srivastava, A. K. Shukla, V. D. Vankar, V. Kumar. Growth, structure and field emission characteristics of petal like carbon nano-structured thin film. *Thin Solid Films* **2005**, 492, 124-130.
10. X. Li, W. Cai, J. An, S. Kim, J. Nah, D. Yang, R. Piner, A. Velamakanni, I. Jung, E. Tutuc, et al. Large-area synthesis of high-quality and uniform graphene films on copper foils. *Science* **2009**, 324, 1312-1314.
11. C. Berger, Z. Song, T. Li, X. Li, A. Y. Ogbazghi, R. Feng, Z. Dai, A. N. Marchenkov, E. H. Conard, P. N. First, et al. Ultrathin epitaxial graphite: 2D electron

gas properties and a route toward graphene-based nanoelectronics. *The Journal of Physical Chemistry B* **2004**, 108, 19912-19916.

12. C. Berger, Z. Song, X. Li, X. Wu, N. Brown, C. Naud, D. Mayou, T. Li, J. Hass, A. N. Marchenkov, et al. Electronic confinement and coherence in patterned epitaxial graphene. *Science* **2006**, 312, 1191-196.

13. X. Yang, X. Dou, A. Rouhanipour, L. Zhi, H. J. Rader, K. Mullen. Two-dimensional graphene nanoribbons. *Journal of the American Chemical Society* **2008**, 130, 4216-4217.

14. S. Park, R. S. Ruoff. Chemical methods for the production of graphenes. *Nature Nanotechnology* **2009**, 4, 217-224.

15. T. Ohta, A. Bostwick, T. Seyller, K. Horn, E. Rotenberg. Controlling the electronic structure of bilayer graphene. *Science* **2006**, 313, 951-954.

16. S. Y. Zhou, G. -H. Gweon, A. V. Fedorov, P. N. First, W. A. de Heer, D. -H. Lee, F. Guinea, A. H. Castro Neto, A. Lanzara. Substrate-induced bandgap opening in epitaxial graphene. *Nature Materials* **2007**, 6, 770-775.

17. M. Y. Han, B. Ozyilmaz, Y. B. Zhang, P. Kim. Energy band-gap engineering of graphene nanoribbons. *Physical Review Letters* **2007**, 98, 206805.

18. Y. W. Son, M. L. Cohen, S. G. Louie. Energy gaps in graphene nanoribbons. *Physical Review Letters* **2006**, 97, 216803.

19. K. Nakada, M. Fujita, G. Dresselhaus, M. S. Dresselhaus. Edge state in graphene ribbons: Nanometer size effect and edge shape dependence. *Physical Review B* **1996**, 54 (24), 17954-17961.

20. V. Barone, O. Hod, G. E. Scuseria. Electronic structure and stability of semiconducting graphene nanoribbons. *Nano Letters* **2006**, 6 (12), 2748-2754.

21. Y. -W. Son, M. L. Cohen, S. G. Louie. Energy Gaps in Graphene Nanoribbons. *Physical Review Letters* **2006**, 97, 216803.

22. M. Y. Han, J. C. Brant, P. Kim. Electron transport in disordered graphene nanoribbons. *Physical Review Letters* **2010**, 104, 056801.

23. D. V. Kosynkin, A. L. Higginbotham, A. Sinitskii, J. R. Lomeda, A. Dimiev, B. K. Price, J. M. Tour. Longitudinal unzipping of carbon nanotubes to form graphene

- nanoribbons. *Nature* **2009**, 458, 872-875.
24. L. Y. Jiao, L. Zhang, X. R. Wang, G. Diankov, H. J. Dai. Narrow graphene nanoribbons from carbon nanotubes. *Nature* **2009**, 458, 877-880.
25. T. Shimizu, J. Haruyama, D. C. Marcano, D. V. Kosinkin, J. M. Tour, K. Hirose, K. Suenaga. Large intrinsic energy bandgaps in annealed nanotube-derived graphene nanoribbons. *Nature Nanotechnology* **2011**, 6, 45-50.
26. Z. J. Qi, J. A. Rodríguez-Manzo, A. R. Botello-Méndez, S. J. Hong, E. A. Stach, Y. W. Park, J. -C. Charlier, M. Drndić, A. T. C. Johnson. Correlating atomic structure and transport in suspended graphene nanoribbons. *Nano Letters* **2014**, 14(8), 4238-4244.
27. L. Tapasztó, G. Dobrik, P. Lambin, L. P. Biró. Tailoring the atomic structure of graphene nanoribbons by scanning tunnelling microscope lithography. *Nature Nanotechnology* **2008**, 3 (7), 397-401.
28. J. W. Bai, X. F. Duan, Y. Huang, Rational fabrication of graphene nanoribbons using a nanowire etch mask. *Nano Letters* **2009**, 9, 2083-2087.
29. M. Sprinkle, M. Ruan, Y. Hu, J. Hankinson, M. Rubio-Roy, B. Zhang, X. Wu, C. Berger, W. A. de Heer. Scalable templated growth of graphene nanoribbons on SiC. *Nature Nanotechnology* **2010**, 5, 727-731.
30. J. Cai, P. Ruffieux, R. Jaafar, M. Bieri, T. Braun, S. Blankenburg, M. Muoth, A. P. Seitsonen, M. Saleh, X. Feng, K. Mullen, R. Fasel. Atomically precise bottom-up fabrication of graphene nanoribbons. *Nature* **2010**, 466, 470-473.
31. N. Mohanty, D. Moore, Z. Xu, T. S. Sreeprasad, A. Nagaraja, A. A. Rodriguez, V. Berry. Nanotomy nased production of transferrable and dispersible graphene-nanostructures of controlled shape and size. *Nature Communications* **2012**, 3, 844.
32. N. G. Chopra, L. X. Benedict, V. H. Crespi, M. L. Cohen, S. G. Louie, A. Zettl. Fully collapsed carbon nanotubes. *Nature* **1995**, 377 (14), 135-138.
33. P. E. Lammert, P. Zhang, V. H. Crespi. Gapping by squashing: metal-insulator and insulator-metal transitions in collapsed carbon nanotubes. *Physical Review Letters* **2000**, 84 (11), 2453-2456.
34. M. S. C. Mazzoni, H. Chacham. Bandgap closure of a flattened semiconductor

- carbon nanotube: A first-principles study. *Applied Physics Letters* **2000**, 76 (12), 1561-1563.
35. J. A. Elliott, J. K. Sandler, A. H. Windle, R. J. Young, M. S. P. Shaffer. Collapse of single-wall carbon nanotubes is diameter dependent. *Physical Review Letters* **2004**, 92 (9), 095501.
36. H. J. Liu, K. Cho. A molecular dynamics study of round and flattened carbon nanotube structures. *Applied Physics Letters* **2004**, 85 (5), 807-809.
37. V. Gadagkar, P. K. Maiti, Y. Lansac, A. Jagota, A. K. Sood. Collapse of double-walled carbon nanotube bundles under hydrostatic pressure. *Physical Review B* **2006**, 73, 085402.
38. M. Motta, A. Moisala, I. A. Kimloch, A. H. Windle. High performance fibres from 'Dog Bone' carbon nanotubes. *Advanced Materials* **2007**, 19, 3721-3726.
39. C. Zhang, K. Bets, S. S. Lee, Z. Sun, F. Mirri, V. L. Colvin, B. I. Yakobson, J. M. Tours, R. H. Hauge. Closed-edged graphene nanoribbons from large-diameter collapsed nanotubes. *ACS Nano* **2012**, 6 (7), 6023-6032.

## Chapter 2

### Preparation and Characterization of Fully Flattened Carbon Nanotubes (FNTs)

Graphene has attracted intense interest because of its intriguing electrical, optical and mechanical properties [1-3]. Although graphene exhibits high carrier mobility of  $> 10,000 \text{ cm}^2\text{V}^{-1}\text{s}^{-1}$  at room temperature, the main issue for the application of graphene in electronics is the fact that graphene is a zero-gap semiconductor. Therefore, the opening of a sizable and well-defined bandgap is a highly important problem for the development of graphene-based electronics. Among the several methods proposed for the opening of the graphene bandgap [4, 5], narrowing the width of graphene to several tens of nanometers is considered to be the most promising approach [6, 7]. At present, there are many reports proposing different techniques for narrowing the graphene width, such as unzipping of CNTs [8, 9], templated growth on SiC [10] and the narrowing of width of graphene by electron beam lithography [11]. Comparing these methods, the ease and scalability of the fabrication approach used to obtain graphene nanoribbons (GNRs) become the most important issues.

The structure of fully flattened CNTs (FNTs) is almost identical to that of GNRs except for the smooth closed edges. FNTs were first experimentally identified by A. Zettl and coworkers during their TEM investigations of multiwall carbon nanotubes (MWCNTs) [12]. In this study, the FNTs (GNR analogs) that are formed by a spontaneous collapse of large-diameter MWCNTs are expected to show a combination of nonzero band gaps and high carrier mobility. Heretofore, no method has been developed for the synthesis of high-quality FNTs with a high yield. Here we have focused on the following two topics: (1) development of a simple and low-cost method for the synthesis of high-quality FNTs and their subsequent characterization and (2) utilization of  $\text{H}_2$  plasma for the purification and an edge structure control of FNTs and investigations of their electrical properties.

## 2.1 Preparation of FNTs

### 2.1.1 Preparation method

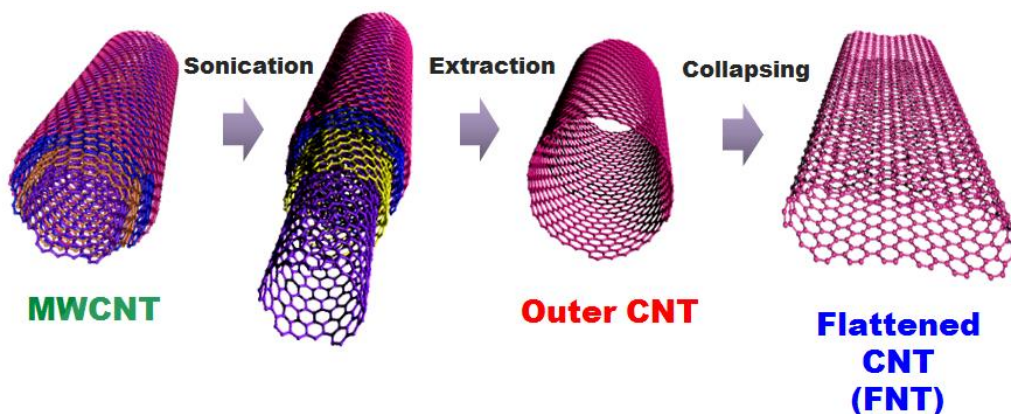


**Figure 2.1** Schematic representation of the production mechanism of FNTs.

FNTs were synthesized by a sonication-based solution phase process, where large-diameter few layers inner MWCNTs were extracted from the intact MWCNTs, and outer CNTs were spontaneously flattened to form FNTs, as shown in Figure 2.1.

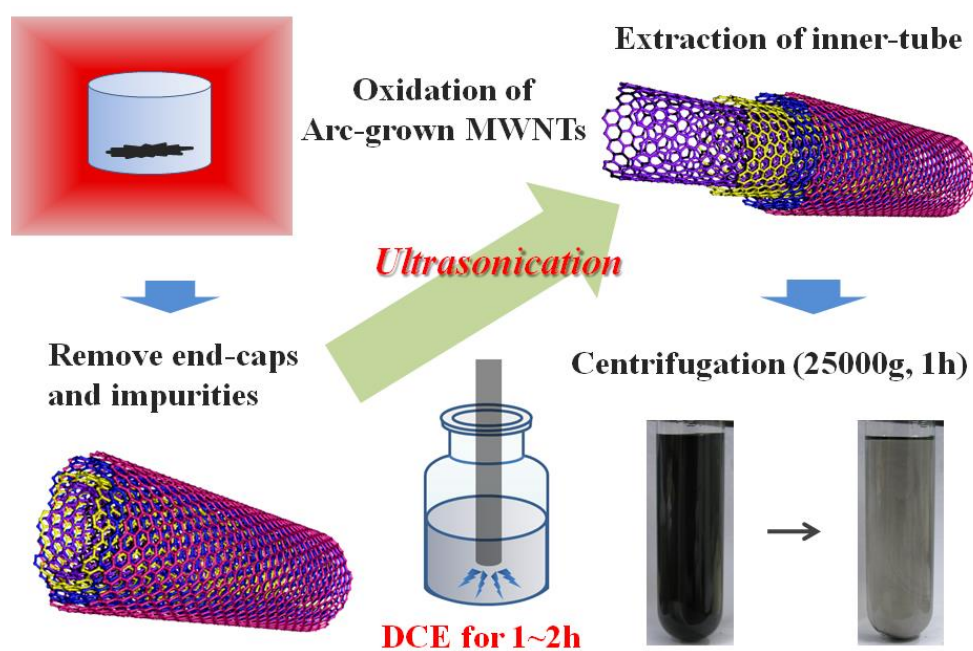


**Figure 2.2** Schematic diagrams of the preparation procedure of FNTs.

We performed a thermal oxidation reaction at 973 K for 30 min under dry air flow to remove the closed edges at both ends of MWCNTs prior to the extraction of large-diameter CNTs. Thermal gravimetric analyses was used to control and monitor the weight loss of MWCNTs during the oxidation process. To ensure the complete opening of closed caps of MWCNTs, we controlled the typical weight loss after the oxidation process about 40%. In the extraction process of large-diameter CNTs, we first used an ultrasonic sonicator for 1 h at 298 K to disperse the MWCNT sample (7 mg) in 1,2-dichloroethane (DCE) or H<sub>2</sub>O (20 mL) with 1% weight per volume (w/v) solution of sodium dodecyl sulfate (SDS). Then we performed obtained centrifuged for 1 h at 25,000 g on the dispersion solution, and collected the supernatant solution.

FNTs were synthesized in a solution process by a unique ultrasonication method. Figure 2.3a illustrates the strong power tip-type ultrasonication (Sonifier 250-450) for the extraction of MWCNTs. A bath-type sonication (Nano Ruptor) was used to disperse FNT powder in weaker power to avoid generating too many defects (Figure 2.3b).



**Figure 2.3** (a) Sonifier 250-450; (b) Nano Ruptor.

### **2.1.2 Transmission electron microscope**

In transmission electron microscope (TEM), the accelerated and focused electron beam is projected on a very thin sample membrane, and the electrons reflect from the sample atoms in different directions, generating solid angle scattering. The scattering angle forms the images on the screen by giving rise to different contrast depending on the samples. TEM observations in this research were performed using a high-resolution field-emission gun TEM (JEM-2100, JEOL) operated at 80 kV at room temperature and under a pressure of  $10^{-6}$  Pa. TEM images were recorded with a charge-coupled device with a typical exposure time of 1 s.



**Figure 2.4** Transmission electron microscope (JEM-2100, JEOL).

The supernatant of the SDS solution was mixed with methanol, and the precipitated FNT was collected by filtration. The obtained FNT powder was dispersed in methanol for use in subsequent experiments. For the second dispersion of FNTs, the dispersion time was not very long to avoid causing too many defects. In that case, FNTs were usually bunched up; therefore, only a limited number of FNTs could be observed. We also found that the surfactant sometimes remained on the FNT surfaces, as shown in Figure 2.5d; therefore, we chose to use DCE as the dispersion solution in the subsequent experiments.

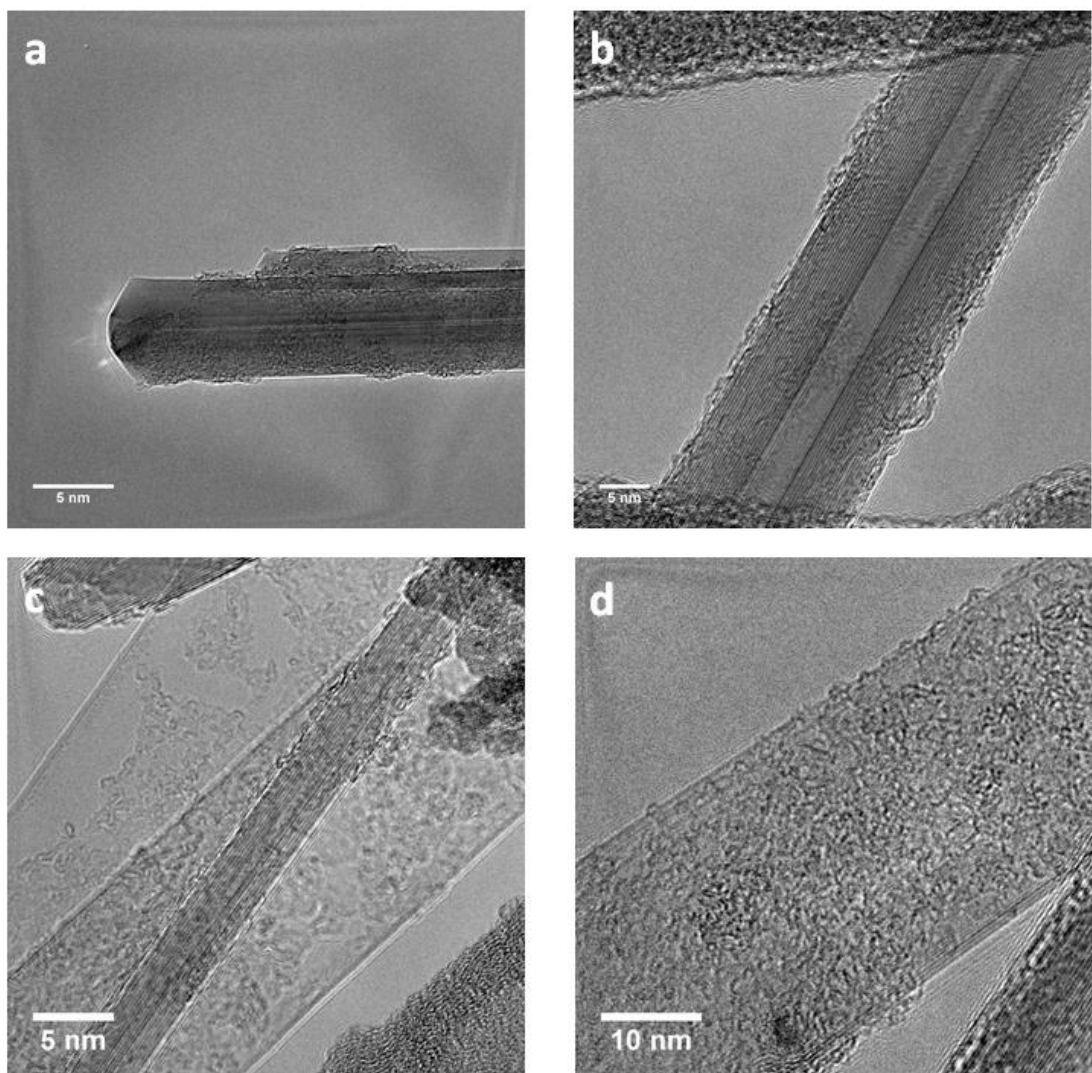


**Figure 2.5** (a) and (b) TEM images of pristine closed ends MWCNTs: straight, high crystallinity without any kinks; TEM images of FNTs prepared in (c) DCE and (d) SDS solution.

## 2.2 Characterization of FNTs

This kind of solution process is a simple and low-cost method for the synthesis of high-quality FNTs with a high yield. As shown in Figure 2.6, at least seven FNTs are present in this  $1.2 \times 1.2 \mu\text{m}$  regime entwined in the carbon membrane, and are marked by yellow dashed lines. The close-up image shows a bilayer FNT with some amorphous carbon on the surface, which results from the collapse of a double-wall CNT.

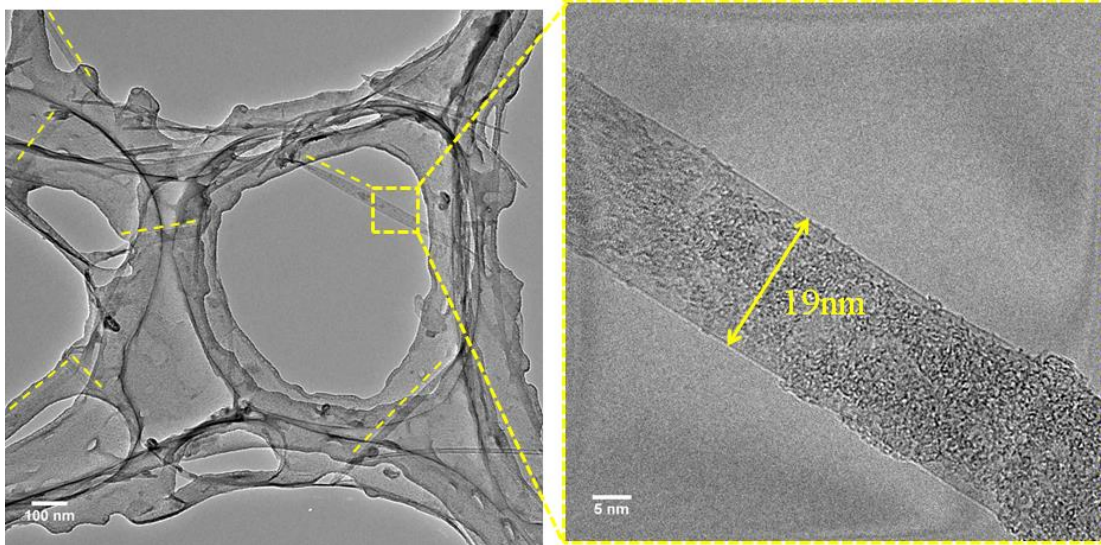


**Figure 2.6** Low magnification TEM images of FNTs on carbon membrane with a close-up image of a 19 nm wide bilayer FNT.

### 2.2.1 AFM characterization of FNTs

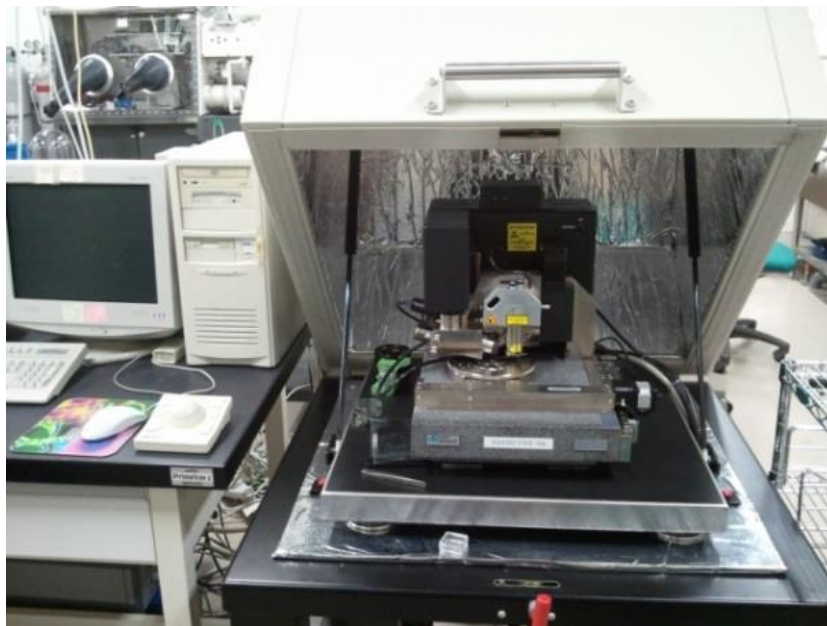


**Figure 2.7** Atomic force microscope (Dimension 3199 SPM, Veeco).

Atomic force microscope (AFM) is a very high-resolution type of scanning probe microscope with resolution on the order of fractions of nanometers. AFM can be

operated in three imaging modes: the contact mode, tapping mode, and noncontact mode. In our work, we always use the tapping mode. In the tapping mode, when the tip approaches the sample surface, the interacting forces are detected by the laser detector. As shown in Figure 2.7, we used AFM (Dimension 3199 SPM, Veeco) to study the thickness, diameter, and length of FNTs.

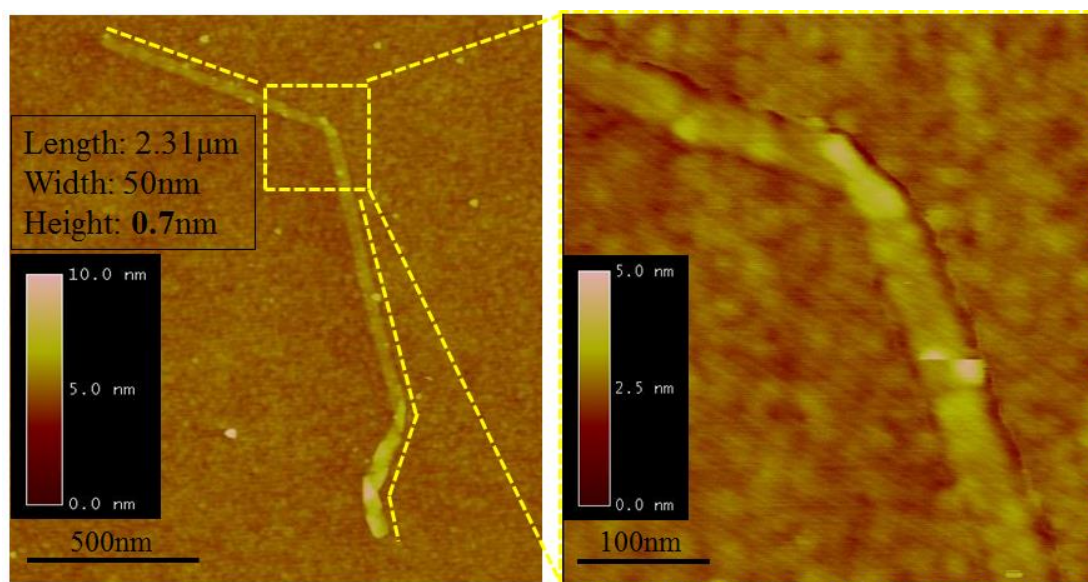


**Figure 2.8** AFM images of a 2.31  $\mu\text{m}$  long, 50 nm wide, 0.7 nm high bilayer FNT with magnified image of twisted part.

In general, FNTs have widths of 10 ~ 50 nm and are 1 ~ 3  $\mu\text{m}$  long; because it is impossible to observe FNTs using an optical microscope, we performed AFM characterization to study the surface morphology of FNTs. FNTs in the DCE solution were dropped onto a Si substrate, and after 10 ~ 20 min, they were dried by  $\text{N}_2$  gas flow. FNT adsorbed on the Si substrate surface was because of van der Waals interactions. Because of the barbell-like cross section of FNT, we should observe a height plane in the surface of FNT, not a round contrast. An AFM image of a typical FNT on Si substrate is presented in Figure 2.8 and shows that FNT was formed by the collapse of a single-wall CNT, as indicated by the height of only 0.7 nm. As is well known, the thickness of a monolayer graphene is approximately 0.34 nm; therefore, the 0.7 nm thick graphitic structure must be because of a bilayer graphene. This 2.31

$\mu\text{m}$  long, 50 nm wide FNT was twisted several times, which has never been found in the original MWCNTs. The magnified images showed that the distorted region was much higher than the other regions. In the straight region of the FNT, a height plane was observed in the middle with a brighter contrast on the edges, indicating the barbell-like cross section of FNTs.

Unlike TEM observations, AFM characterization can also be used to define the layer number of FNTs without damaging the samples. This will be helpful for the subsequent investigation of pristine FNTs by Raman or electrical measurements. Figure 2.9 shows a bilayer FNT and a four-layer FNT with heights of 0.7 nm and 1.5 nm, respectively. The black inset of the height data clearly shows the height plane in the middle and curvature in the edges.

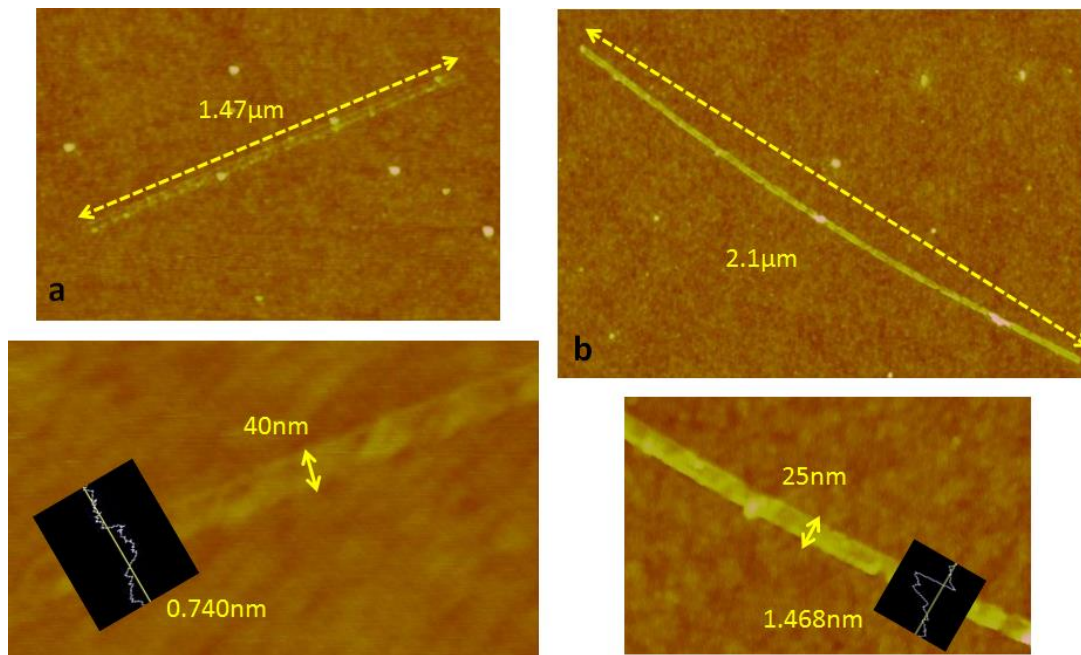


**Figure 2.9** AFM images of (a) a 1.47  $\mu\text{m}$  long, 40 nm wide and 0.740 nm high bilayer FNT; (b) a 2.1  $\mu\text{m}$  long, 25 nm wide and 1.468 nm high four-layer FNT. Insets: height data of the two FNTs.

### 2.2.2 Raman measurement of FNTs

Raman spectroscopy is a spectroscopic technique used to observe vibrational,

rotational, and other low-frequency modes of a system. The laser light interacts with molecular vibrations, phonons, or other excitations that result in the energies of laser photons shifting up and down. Among the various Raman-active vibration modes observed for graphene, the three most distinctive features are the disorder-induced D band (around  $1350\text{ cm}^{-1}$ ), G band (around  $1590\text{ cm}^{-1}$ , caused by the in-plane vibration of carbon atoms) and 2D band (around  $2680\text{ cm}^{-1}$ , double phonon resonance peak). Lab RAM HR-800 (HORIBA JOBIN Yvon) was used to evaluate the purity and structural changes in FNTs with a laser illumination at 633nm or 488nm (Figure 2.10).

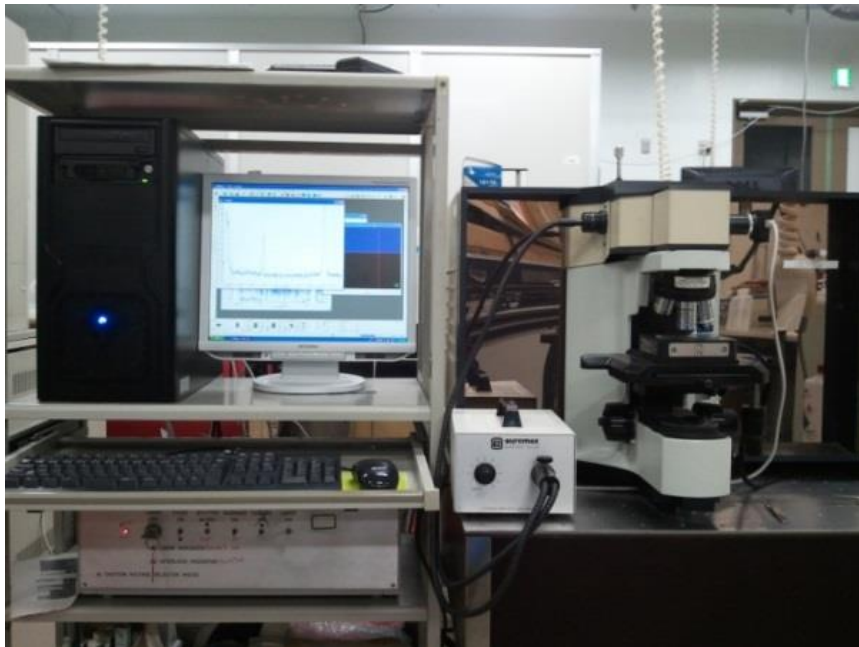


**Figure 2.10** Raman spectrometer (Lab RAM HR-800, HORIBA JOBIN Yvon).

Raman measurement of GNRs shows a G-band at  $1590\text{ cm}^{-1}$  that is common in graphite materials and a 2D-band at  $2680\text{ cm}^{-1}$  with a strong width dependency. It is well-known that for a single-layer graphene, the 2D-band is more prominent than the G-band. When the width of graphene decreases to nanoscale, the intensities of G and 2D features decrease, while the intensity of the D feature increases because of the edge effect [13, 14].

Figure 2.11a showed the AFM image of a 1.8 nm high FNT, which maybe a

six-layer FNT, with the corresponding Raman spectrum shown in Figure 2.11b. An obvious D feature is present because of the edge effect at the nanoscale. The smooth closed edges of FNT make the intensity of the D-band weaker than that in the usual GNRs. The G feature is much stronger than the 2D feature, consistent with the presence of the few-layer graphene.

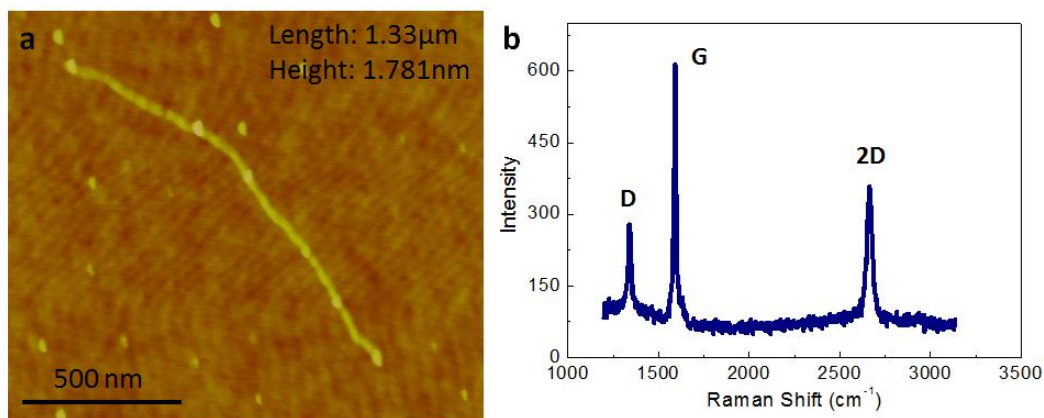


**Figure 2.11** (a) AFM image of a 1.33 μm long, 1.781 nm high FNT; (b) Raman spectrum of the same FNT.

### 2.3 H<sub>2</sub> plasma treatment of FNTs

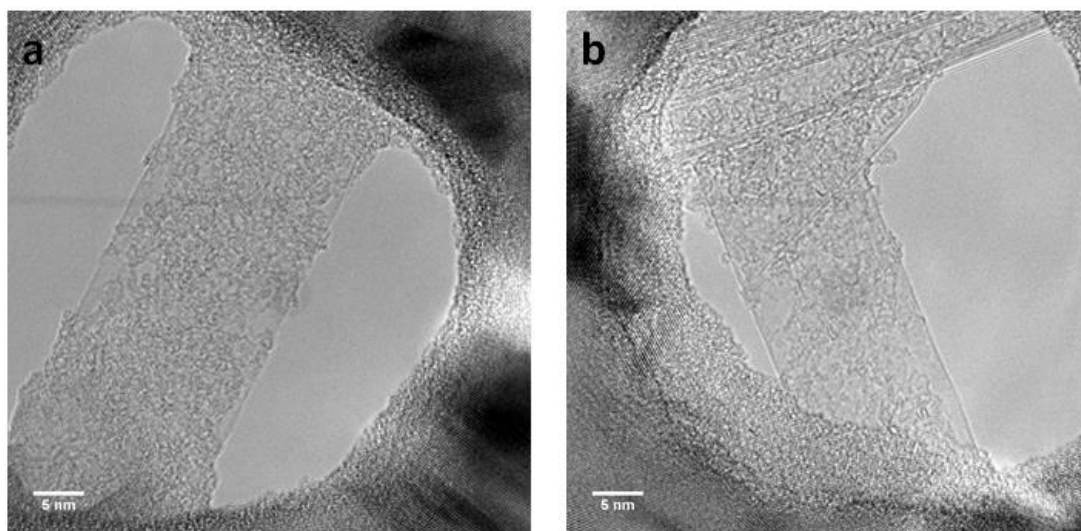


**Figure 2.11** TEM images of two bilayer FNTs with amorphous carbon on the surface.

The original prepared FNTs were usually found with amorphous carbon on the surface,

making it difficult to investigate the details of their structure by TEM (Figure 2.11). We therefore used our home-made H<sub>2</sub> plasma to remove the amorphous carbon and found H<sub>2</sub> plasma can be used to control the edges of FNTs due to the higher energy and much more reactive nature of carbon atoms at the edges.

### 2.3.1 Purification of FNTs

H<sub>2</sub> plasma was controlled in mild conditions to remove the amorphous carbon on the FNT surface without damaging FNTs, as shown in Figure 2.12. The two crossed FNTs were purified by H<sub>2</sub> plasma without causing any visible damage.

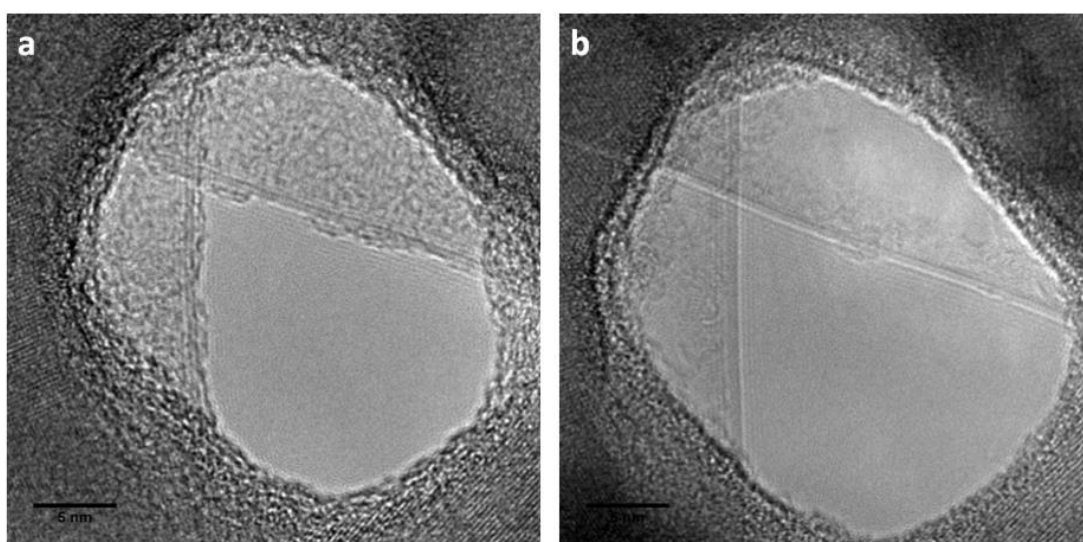


**Figure 2.12** TEM images of two crossed four-layer FNTs (a) before and (b) after H<sub>2</sub> plasma treatment in mild conditions (8 W) for 10 min.

To determine the amount of defects, Raman measurements were performed on the same FNT before and after H<sub>2</sub> plasma purification. Figure 2.13 shows the AFM image of a four-layer FNT (a) and the Raman spectra of this FNT before (b) and after (b) H<sub>2</sub> plasma purification. All the features showed increased intensities after purification because of the removal of the amorphous carbon. There is no obvious increase in the relative intensity of the D feature compared with that of G and 2D features.

Following H<sub>2</sub> plasma purification, FNTs were characterized in detail by CS-TEM.

Figures 2.14a and 2.14b show high-magnification CS-TEM images of a bilayer FNT with a smooth closed edge; the fast Fourier Transform (FFT) image in the inset shows two sets of hexagonal patterns, implying that at least two graphene layers are present.

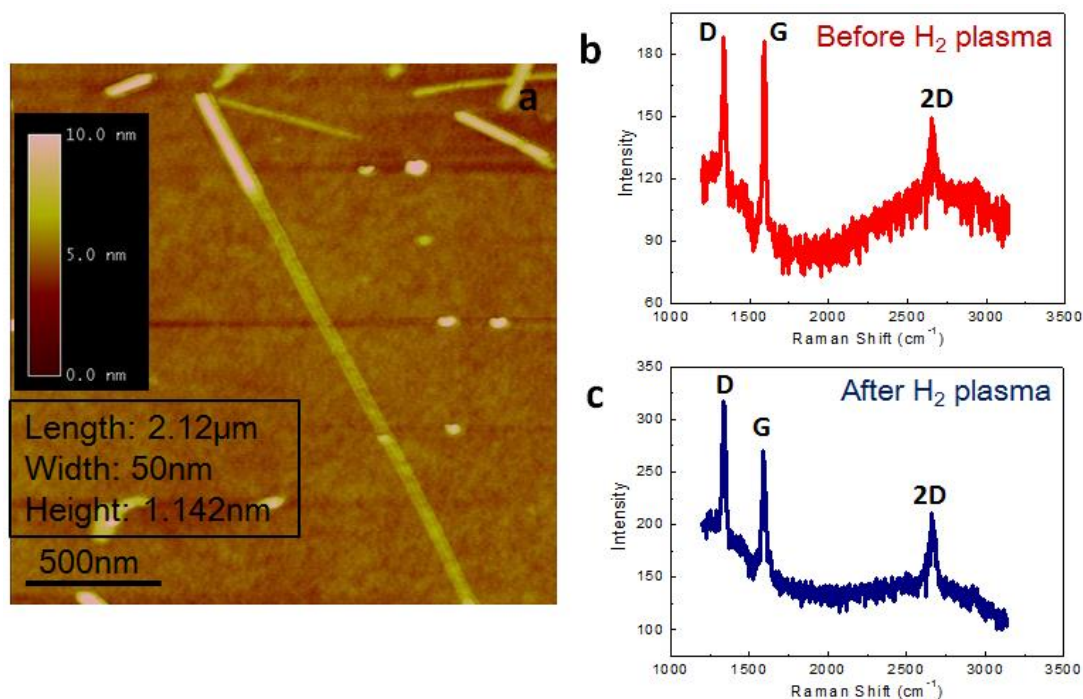


**Figure 2.13** (a) AFM image of a bilayer FNT; Raman spectra of the FNT (b) before and (c) after H<sub>2</sub> plasma purification.

The Moiré pattern originating from a superposition of the hexagonal network of graphene layers is also observed. The TEM image and the diffraction pattern of a 14.2 nm wide, four-layer FNT are given in Figures 2.14c and 2.14d, respectively. The TEM image shows two linear contrasts at both edges, similar to the folded edge of a bilayer graphene. The diffraction results show four sets of hexagonal patterns that are marked by yellow, green, pink, and purple hexagon in the figure. This means that at least four graphene layers are present, consistent with the folded bilayer graphene. Furthermore, the non-arbitrary orientation of the graphene layers is indicated by the two pairs of the hexagonal patterns (green and yellow, purple and pink) with 2 mm symmetry. On account of the relative orientation of the face-to-face graphene layers in SWCNTs, 2 mm symmetry is always observed in the electron diffraction pattern of a single-wall

CNT (SWCNT) under normal incidence [15]. Therefore, we confirmed that the interlayer orientation of CNTs does not change after the sonication process because of the observed 2 mm symmetry of the FFT images

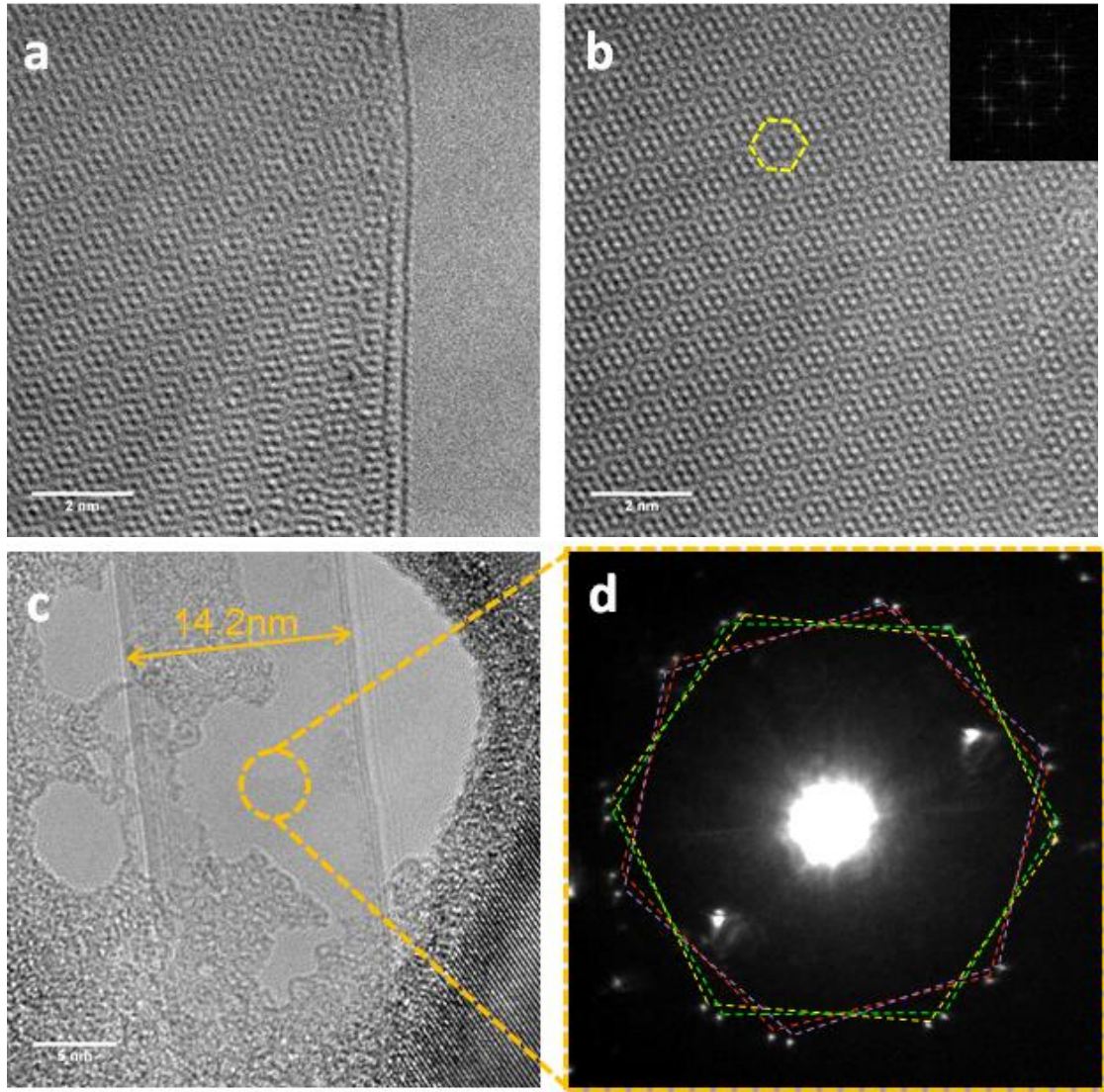
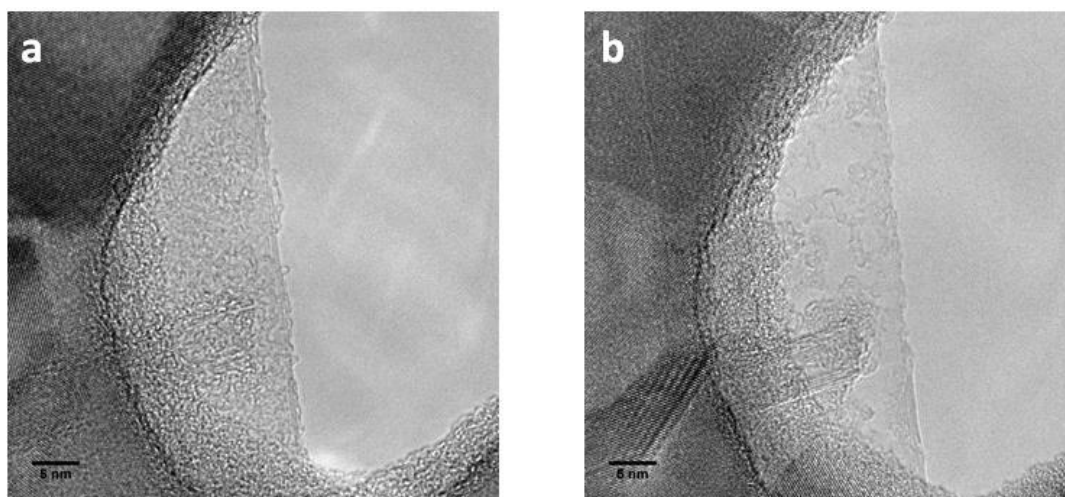


**Figure 2.14** High magnification CS-TEM images of a bilayer FNT with (a) smooth closed edge, (b) clear Moiré pattern and two sets of hexagonal pattern in the inset fast Fourier Transform image; (c) TEM image and (d) diffraction pattern of a four-layer FNT.

### 2.3.2 Edges control of FNTs

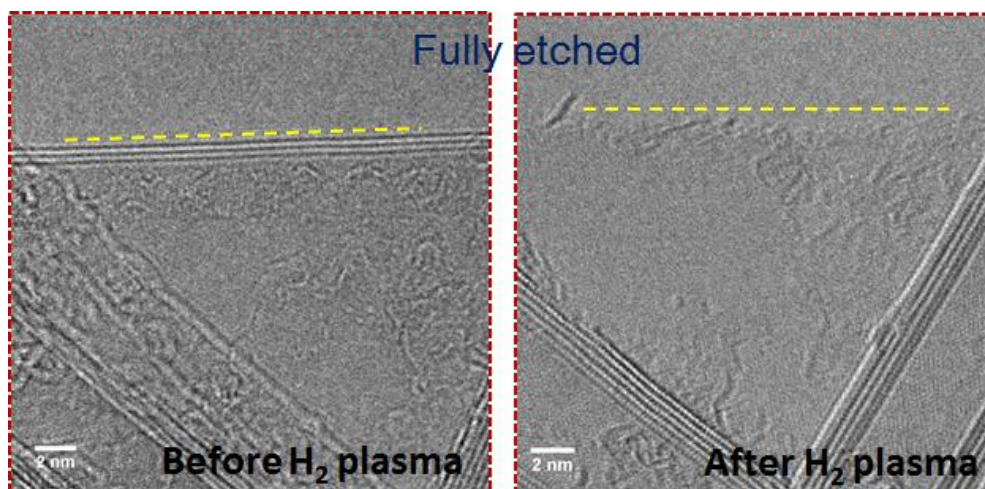
Because FNT has a barbell-like cross section, carbon atoms on the closed edges are

more reactive due to the curvature. That enables the control of the edges of FNTs by the  $H_2$  plasma treatment because the carbon atoms on the edges will preferentially react with  $H^+$  ions. Figure 2.15 shows TEM images of an identical FNT before and after edge control by  $H_2$  plasma, in which amorphous carbon was removed and the edge of the four-layer FNT was etched away.



**Figure 2.15** TEM images of a four-layer FNT (a) and (b) after edge control by  $H_2$  plasma at 10 W for 20 min.

We also investigated the etching ratio by counting the edge etched FNTs present after the application of  $H_2$  plasma. TEM images of identical FNTs before and after  $H_2$  plasma etching show that the total etching ratio was approximately 60%, including full etching and partial etching as shown in Figure 2.16.



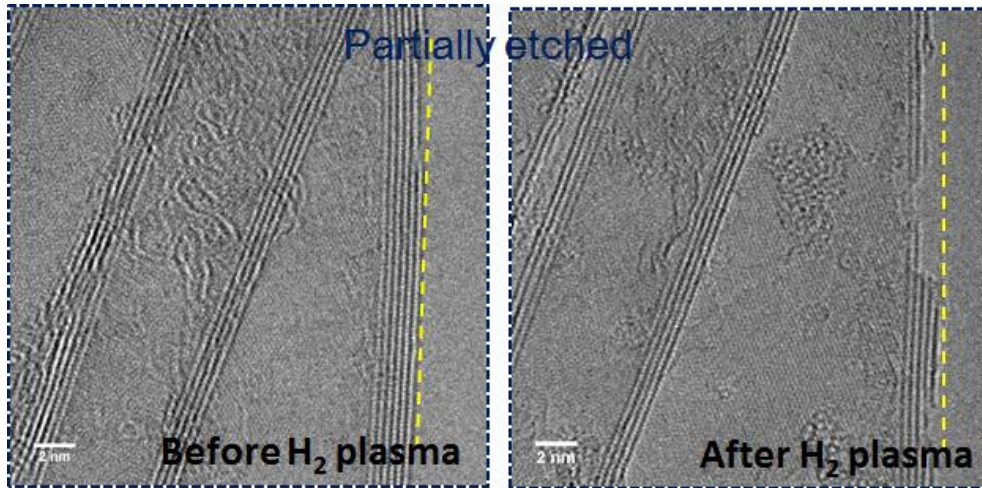


**Figure 2.16** TEM images of identical FNTs before and after edges control by  $H_2$  plasma with an etching ratio about 60%, including fully etching (red) and partially etching (blue).

An edge-etched FNT can be considered as a few-layer GNR with disordered edges. In Figure 2.17, a bilayer GNR (edge-etched FNT) was characterized by CS-TEM in details. The closed-up image shows clear Moiré pattern, and the inset FFT image shows two sets of hexagonal patterns, indicating that the layer number is two.

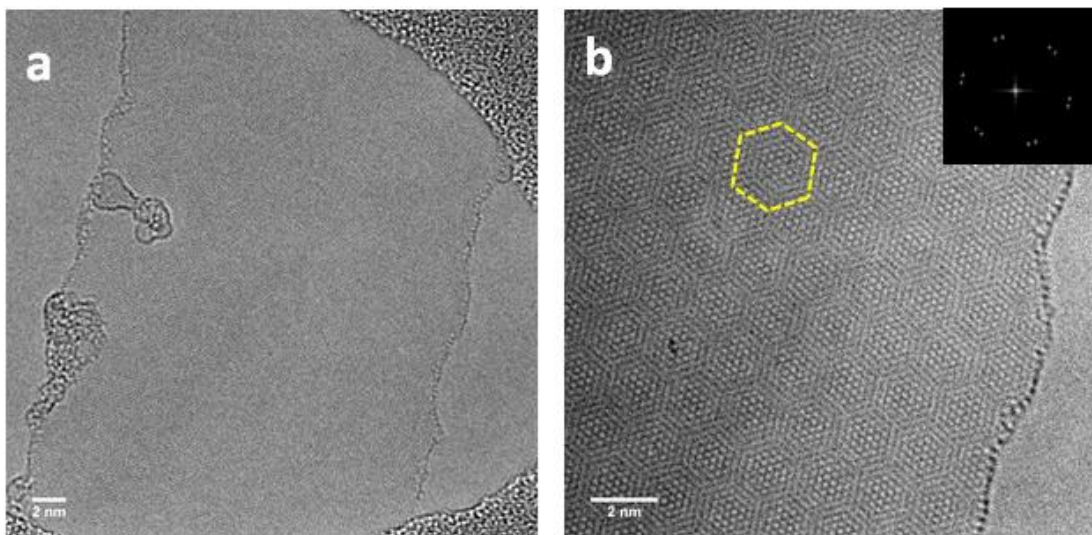


**Figure 2.17** CS-TEM images of (a) a bilayer GNR (edge-etched FNT) and (b) closed-up image with an inset of FFT image.

## 2.3 Electronic characterization of FNTs

### 2.3.1 Preparation of marks

Electron beam lithography uses a focused scanning beam of electrons to draw custom shapes on a surface covered with an electron-sensitive film called photoresist (this process called exposing process). The solubility of the photoresist is changed by electron beam, and then the exposed or non-exposed regions of the photoresist will be selectively removed by a developing process (immersing it in a certain solvent). In this research, electronic contacts (Cr and Au) were made using EBL (ELS-7500EX in Majima lab and ELS-3700NC, ELIONX) and thermal evaporator (metal deposition) shown in Figure 2.18.

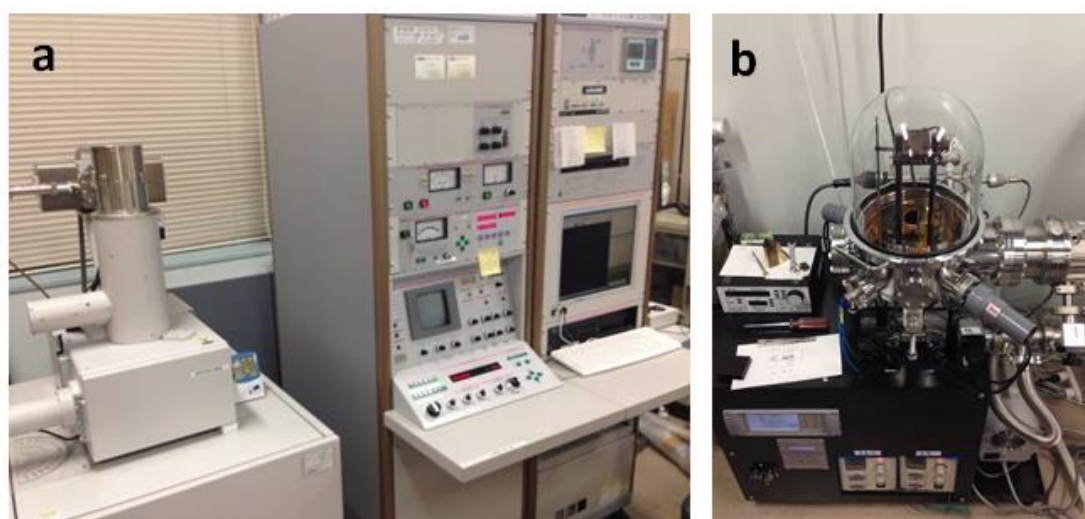


**Figure 2.18** (a) Electron beam lithography (ELS-3700NC); (b) Thermal evaporator.

FNTs are too small to be observed by an optical microscope; therefore, FNTs must be located using visible marks. Here we designed numbered marks for the location of FNTs by AFM. The designed EBL files are shown in Figure 2.19a and 2.19b, with a distance of 150  $\mu\text{m}$  between the two numbered marks and 25  $\mu\text{m}$  between two small marks (Figure 2.19a). The numbers are on the upper left of two opposed squares, as shown in Figure 2.19b. The Au marks were obtained after EBL exposure and metal

deposition of 5 nm Cr and 30 nm Au (Figure 2.19 c and d).

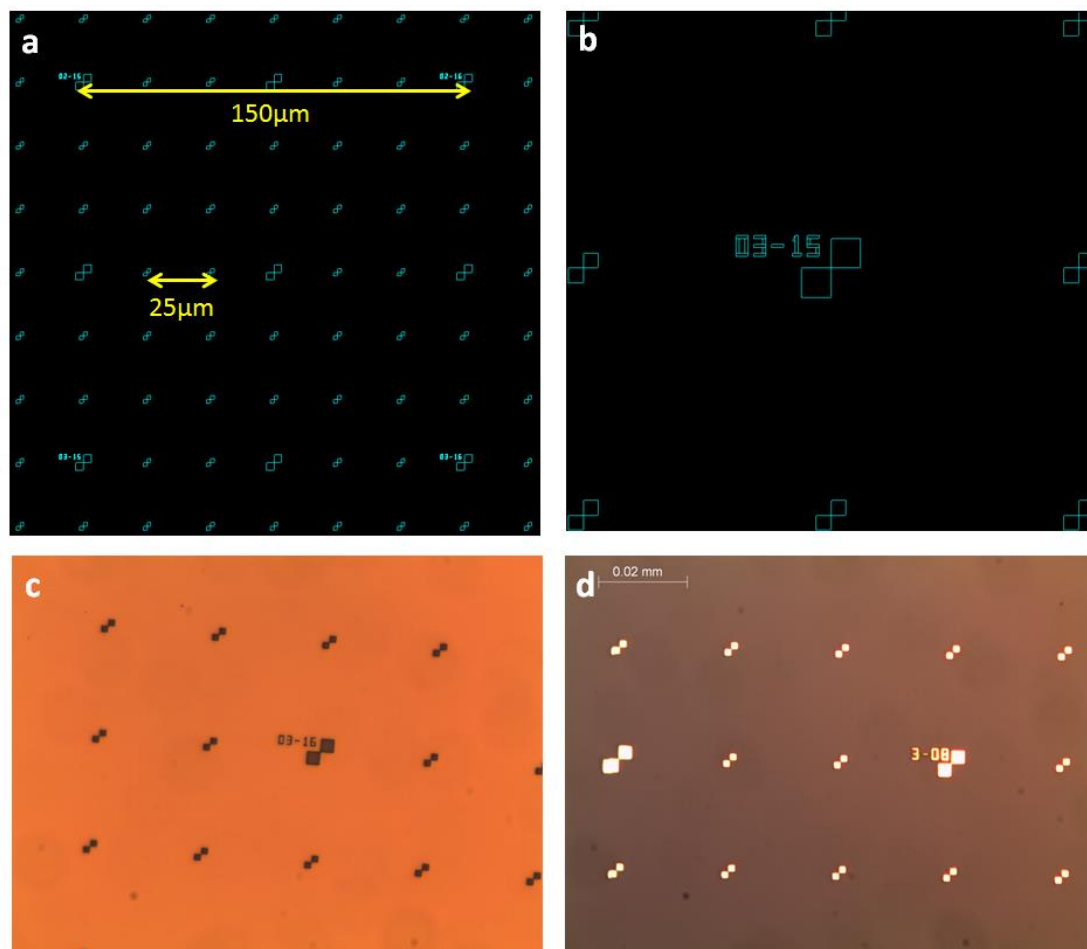


**Figure 2.19** (a) and (b) EBL design files of marks and numbers in different size and distance; Optical microscopy images of marks (c) after EBL exposure and development and (d) after metal deposition of Cr and Au.

### 2.3.3 Preparation of FNTs devices

FNT solution was dropped onto the marked SiO<sub>2</sub>/Si substrate, and FNTs were adsorbed onto the SiO<sub>2</sub> surface by van der Waals forces. AFM was then used to locate FNTs by marks, as shown in Figure 2.20. There are three FNTs near Mark 3-20, and coordinates of these three FNTs can be obtained by measuring the distance between FNTs and the marks. According to the AFM observation, the three FNTs may be in an eight-layer (four-wall CNT collapsing) structure, and the brighter part may be folded

parts, as judged from the double height.

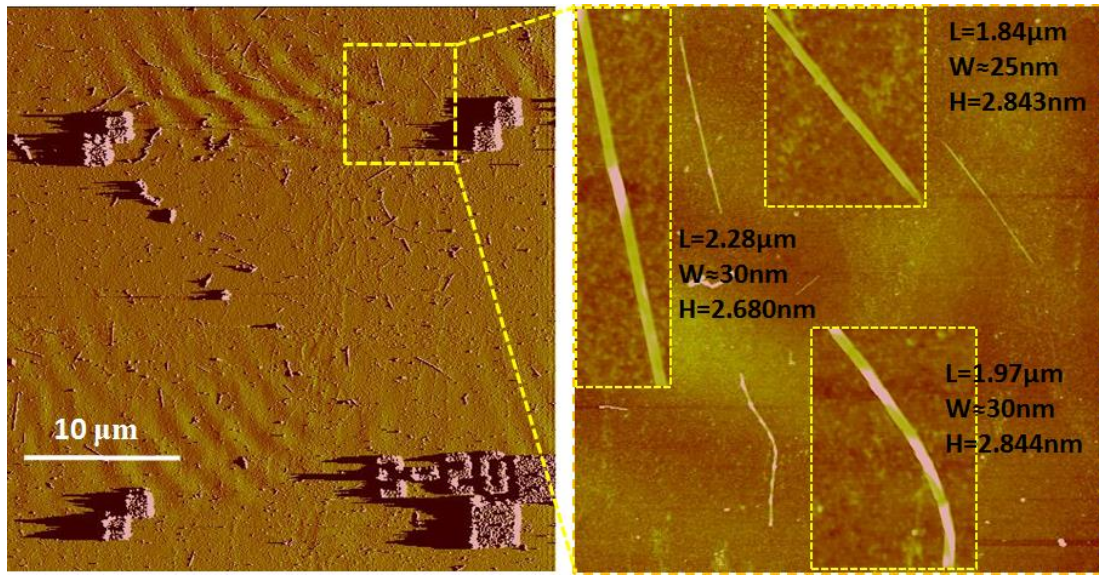


**Figure 2.20** AFM images of FNTs near Mark 3-20: closed-up image shows three FNTs having similar height about 2.8 nm, length about 2 μm and width about 30 nm, which indicated FNTs may be formed by four-wall CNTs; insets show the surface morphology of these three FNTs.

The electrode pattern was designed for EBL exposure according to their length. Two-terminal and four-terminal devices can be fabricated using FNTs shorter than 2 μm and 2.5 μm, respectively. The electrode channel was usually controlled to 300 ~ 800 nm.

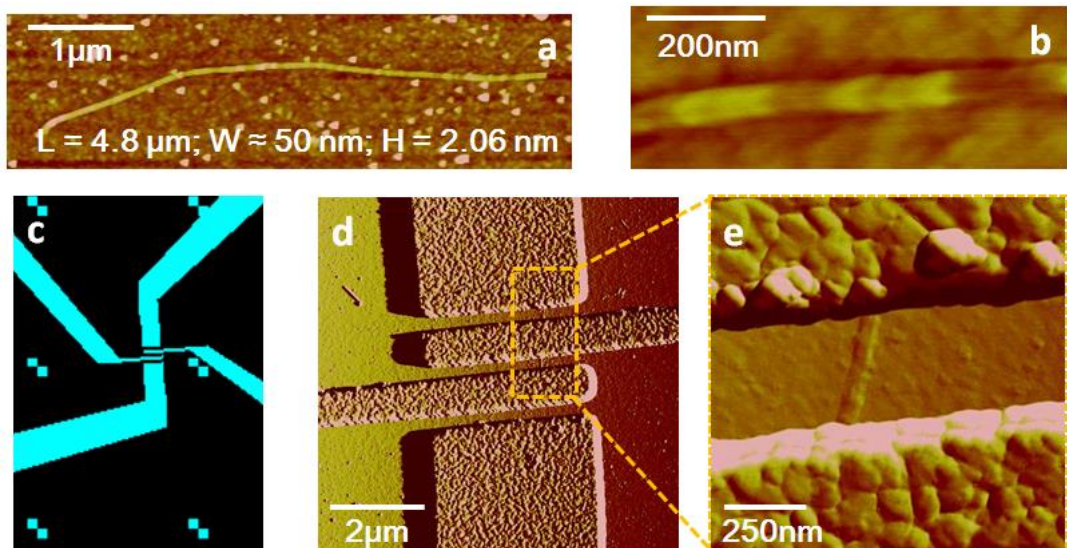


**Figure 2.21** (a) AFM image of a 4.8  $\mu\text{m}$  long, 50 nm wide and 2.06 nm high FNT (may be six-layer, collapsed by a triple-wall CNT); (b) Closed-up AFM image of the FNT with clear surface morphology; (c) EBL design file image of the FNT for a four-terminal device; (d) and (e) the prepared four-terminal FNT device was characterized by AFM with channel with about 300 nm.

As shown in Figure 2.21, a 4.8  $\mu\text{m}$  long and 50 nm wide six-layer FNT (a triple-wall CNT collapsing, judging from the height of approximately 2.1 nm) was used to make a four-terminal device. Using the EBL design pattern in Figure 2.21c, EBL exposure and development was performed and electronic contacts were made by metal deposition of 5 nm Cr and 45 nm Au. The prepared device was also observed by AFM (Figure 2.21d), and the closed-up image (Figure 2.21e) showed that FNT bridged two electrodes in a 300 nm wide channel.

### 2.3.4 Electrical measurement of FNTs devices

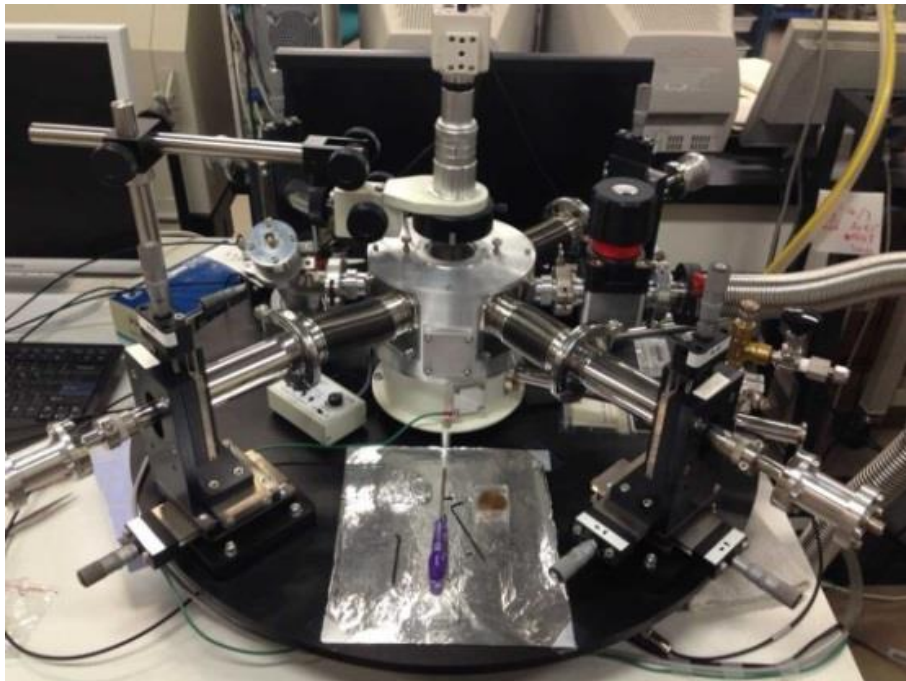


**Figure 2.22** Vacuum probe station (JANIS).

Electronic structures are strongly affected by the geometry of nanocarbon materials,

particularly for GNRs. The electrical properties of GNRs strongly depend on their edge structures, making it very important to study the electrical properties of FNTs and GNRs. We obtained transfer and output characteristics of FNTs and GNRs devices using vacuum probe station (E-400EBS (SHIMASZU) in Majima lab and JANIS, ST-500-1-4TX) and semiconductor parameter analyzer (B1500 (Agilent) in Majima lab and KEITHLEY 4200-SCS). Devices can be measured under a pressure of  $10^{-6}$  mbar from 4 K to 450 K (by applying liquid  $N_2$  or He and controlled heater) with a back gate bias.

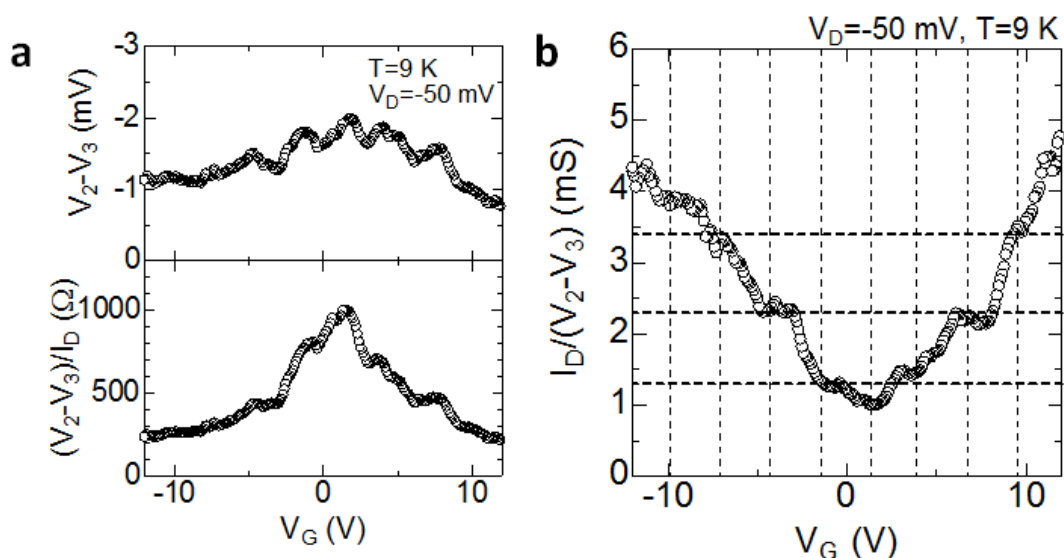


**Figure 2.23** (a) Potential and resistance, (b) conductance of a few-layer FNT measured as a function of gate voltage at 9 K with a drain bias voltage of 50 mV.

All the electrical measurements in this experiment were performed on the back-gated FNTs on highly doped Si substrates with a 300 nm thick  $SiO_2$  gate dielectric. The so-prepared FNTs devices were used to obtain transport and output characteristics using a vacuum probe station. Four-probe measurements were performed to reduce the influence of contact resistance. Figure 2.23 shows an example of transport characteristics of a few-layer FNT device with a FNT channel length of 300 nm for four-probe measurement at 9 K. The device exhibits typical ambipolar transport behavior with a Dirac point, showing both hole and electron

accumulation regime at low gate voltages (-12 ~ 12 V). It should be mentioned that since the MWCNTs are supposed to be metallic and to show no gate-voltage dependence, our results confirm that the measured CNT is not MWCNT but FNT. In Figure 2.23a, the potential drop between the inner two electrodes ( $V_2$  and  $V_3$ ) is 1 ~ 2 mV at a 50 mV drain bias, where most potential drop should be derived from the contact at the electrode/FNT interface. The conductance curve in Figure 2.23b showed the characteristic “V” shape at 9 K with several conductance shoulders. We note that these conductance shoulders, originating from subband of FNT, are observed in both electron and hole branches with nearly the same conductance values and an equal spacing.

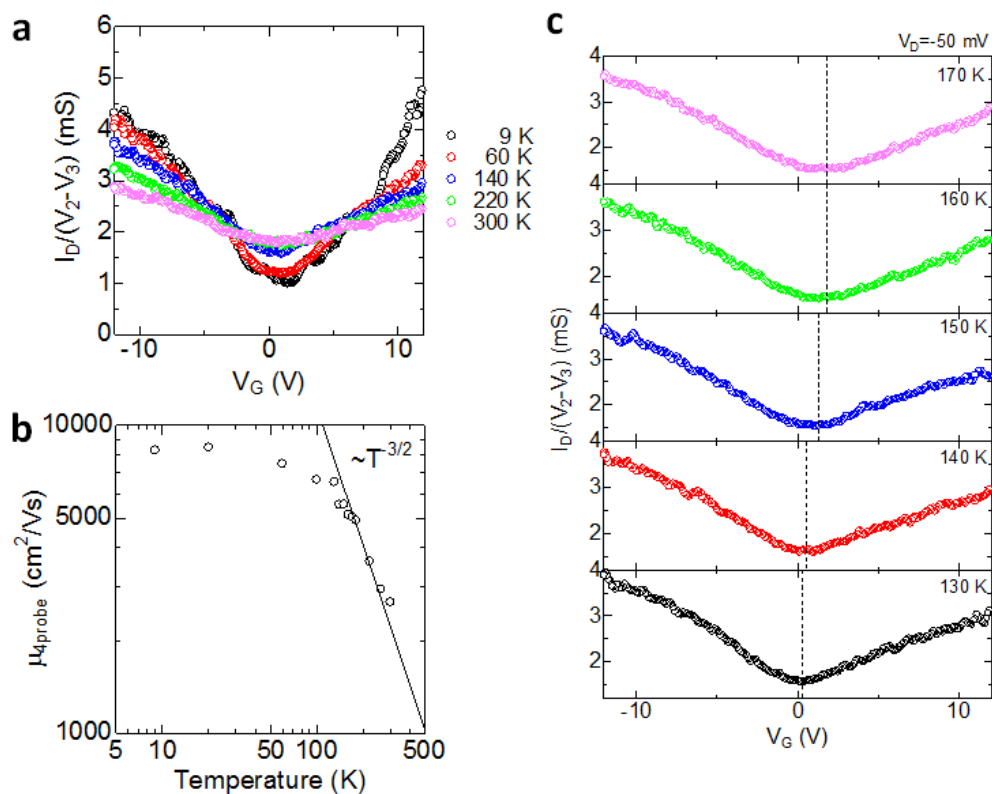


**Figure 2.24** (a) Transfer characteristics of a few-layer FNT measured at different temperature with a drain bias voltage of 50 mV; (b) Mobility plotted as a function of temperature with a fitting line of  $T^{-3/2}$ ; (c) Charge neutrality point at 130 ~ 170 K.

To evaluate the transconductance of FNTs, we have investigated the mobility at

different temperatures using the following formulae:  $\sigma = en\mu$  and  $n = C_{OX}V_G/e$ , where  $\sigma$  (S) is the conductance,  $e$  (C) is the unit charge,  $n$  ( $\text{cm}^{-2}$ ) is the sheet carrier density,  $\mu$  ( $\text{cm}^2/\text{Vs}$ ) is the mobility, and  $C_{OX}$  ( $\text{F}/\text{cm}^2$ ) is the gate capacitance per area. The mobility values calculated from Figure 2.24a at 300 K and 9 K are approximately  $2600 \text{ cm}^2/\text{Vs}$  and  $8300 \text{ cm}^2/\text{Vs}$ , respectively. We also found that mobility measured in a four-probe measurement is much larger than that obtained in a two-probe measurement because of the reduction in current mobility by contact resistance. In Figure 2.24b, mobility is plotted as a function of temperature and fit to  $T^{-3/2}$  temperature dependence. When temperature is higher than 150 K, mobility is proportional to  $T^{-3/2}$  because of the phonon scattering effect. Furthermore, the charge neutrality point (the Dirac point) shifted toward positive gate bias direction around 150 ~ 160 K in Figure 2.24c, which may indicate that charge neutrality is disturbed by phonon scattering.

## 2.4 Conclusions

In this part of my work, we developed a simple and low-cost method for the synthesis of high-quality FNTs and characterized the obtained FNTs using AFM, TEM, and Raman measurements. The AFM images showed a clear height plane in the middle regions of FNTs and two higher edges, indicating the barbell-like cross section of FNTs. An obvious D feature, due to the edge effect at the nanoscale, was observed in the Raman spectrum of an isolated FNT. In addition, the observed G feature is much stronger than the 2D feature, consistent with a few-layer graphene. A general width of FNTs of approximately 10 ~ 50 nm was obtained in TEM observations. Furthermore,  $\text{H}_2$  plasma was used for purification in mild conditions, and edges control of FNTs was performed with an etching ratio of approximately 60%. The electronic characteristics of fewer-layer FNTs exhibited typical ambipolar transport behavior with a Dirac point. We also observed the conductance shoulders originating from FNT subband at 9 K and found that the mobility changed at different temperature because of the phonon scattering effect.

## References

1. K. S. Novoselov, A. K. Geim, S. V. Morozov, D. Jiang, M. I. Katsnelson, I. V. Grigorieva, S. V. Dubobos, A. A. Firsov. Two-dimensional gas of massless Dirac fermions in graphene. *Nature* **2005**, 438, 197-200.
2. S. Bae, H. Kim, Y. Lee, X. Fu, J. -S. Park, Y. Zheng, J. Balakrishnan, T. Lei, H. R. Kim, Y. Song, et al. Roll-to-roll production of 30-inch graphene films for transparent electrodes. *Nature Nanotechnology* **2010**, 5, 574-578.
3. J. S. Bunch, A. M. van der Zande, S. S. Verbridge, I. W. Frank, D. M. Tanenbaum, J. M. Parpia, H. G. Craighead, P. L. McEuen. Electromechanical resonators from graphene sheets. *Science* **2007**, 315,490-493.
4. T. Ohta, A. Bostwick, T. Seyller, K. Horn, E. Rotenberg. Controlling the electronic structure of bilayer graphene. *Science* **2006**, 313 (5789), 951-954.
5. S. Y. Zhou, G. -H. Gweon, A. V. Fedorov, P. N. First, W. A. de Heer, D. -H. Lee, F. Guinea, A. H. Castro Neto, A. Lanzara. Substrate-induced bandgap opening in epitaxial graphene. *Nature Materials* 2007, 6, 770-775.
6. M. Y .Han, B. Ozyilmaz, Y. B. Zhang, P. Kim. Energy band-gap engineering of graphene nanoribbons. *Physical Review Letters* **2007**, 98, 206805.
7. Y. W. Son, M. L. Cohen, S. G. Louie. Energy gaps in graphene nanoribbons. *Physical Review Letters* **2006**, 97, 216803.
8. D. V. Kosynkin, A. L. Higginbotham, A. Sinitskii, J. R. Lomeda, A. Dimiev, B. K. Price, J. M. Tour. Longitudinal unzipping of carbon nanotubes to form graphene nanoribbons. *Nature* **2009**, 458, 872-875.
9. L. Y. Jiao, L. Zhang, X. R. Wang, G. Diankov, H. J. Dai. Narrow graphene nanoribbons from carbon nanotubes. *Nature* **2009**, 458, 877-880.
10. M. Sprinkle, M. Ruan, Y. Hu, J. Hankinson, M. Rubio-Roy, B. Zhang, X. Wu, C. Berger, W. A. de Heer. Scalable templated growth of graphene nanoribbons on SiC. *Nature Nanotechnology* **2010**, 5, 727-731.
11. J. W. Bai, X. F. Duan, Y. Huang. Rational fabrication of graphene nanoribbons using a nanowire etch mask. *Nano Letters* **2009**, 9, 2083-2087.

12. N. G. Chopra, L. X. Benedict, V. H. Crespi, M. L. Cohen, S. G. Louie, A. Zettl. Fully collapsed carbon nanotubes. *Nature* **1995**, 377, 135-138.
13. D. Bischoff, J. Guttinger, S. Droscher, T. Ihn, K. Esslin, C. Stampfer. Raman spectroscopy on etched graphene nanoribbons. *Journal of Applied Physics* **2011**, 109, 073710.
14. L. M. Malard, M. A. Pimenta, G. Dresselhaus, M. S. Dresselhaus. Raman spectroscopy in graphene. *Physics Reports* **2009**, 473 (5-6), 51-87.
15. L. -C. Qin. Electron diffraction from carbon nanotubes. *Reportson Progressin Physics* **2006**, 69, 2761-2821.
16. Y. -M. Lin, V. Perebeinos, Z. Chen, P. Avouris. Electrical observation of subband formation in graphene nanoribbons. *Physical Review B* **2008**, 78, 161409.

## Chapter 3

### Synthesis and TEM Structural Characterization of C<sub>60</sub>-Flattened CNT Nanopeapods

In the past several decades, the discoveries of novel kinds of carbon nanostructure (fullerenes [1], carbon nanotubes [2] and nanopeapods [3]) have promoted the advantage of nanoscience, such as the discovery of nanopeapod [3] has attracted intense interests. Plenty of studies on the structure of peapods have been done and nanopeapods exhibited varieties of atoms or molecules in 1D arrangements, such as sulfide [4], rare earth metal atoms [5, 6], C<sub>60</sub> [7], C<sub>70</sub> [8] and endohedral metallofullerenes [9]. These atoms and molecules have been carried out in the inner space of CNTs, making a new kind of hybrid nanostructures on the basis of CNTs [10]. Intense investigation of nanopeapods has produced in significant findings including bandgap modulation by control of field effect transistor characteristics [11], formation of atomic nanowire in CNTs [5, 6] and encapsulated molecules [12]. This obviously clarifies the consequence of identifying and preparing of a new type of carbon nanostructures.

The synthesis of FNTs that possess the unique shaped inner space using solution-based extraction of large-diameter CNTs from MWCNTs [13] was described in Chapter 2. FNTs are formed by the spontaneously flattening of large-diameter (most outer) CNTs, when the inner CNTs were extracted from MWCNTs. This is caused by the mutual effect of upper and lower walls of CNTs induced by the van der Waals force. Thus a unique low-dimensional inner space is provided by FNTs, which have a completely different inner space with cylindrical inner space of CNTs and a barbell-like cross section. Atoms or molecules are allowed to align not only in a 1D fashion but also in a 2D fashion inside of this new kind of nanospace (Figure 3.1), and a brand new kind of FNT-based hybrid nanostructure is created, FNT peapods, for example. In this chapter we demonstrated the synthesis of FNTs-based C<sub>60</sub>

nanopeapods ( $C_{60}@FNT$ ) and the structural characterization of low-dimensional  $C_{60}$  arrays on the basis of TEM observations.

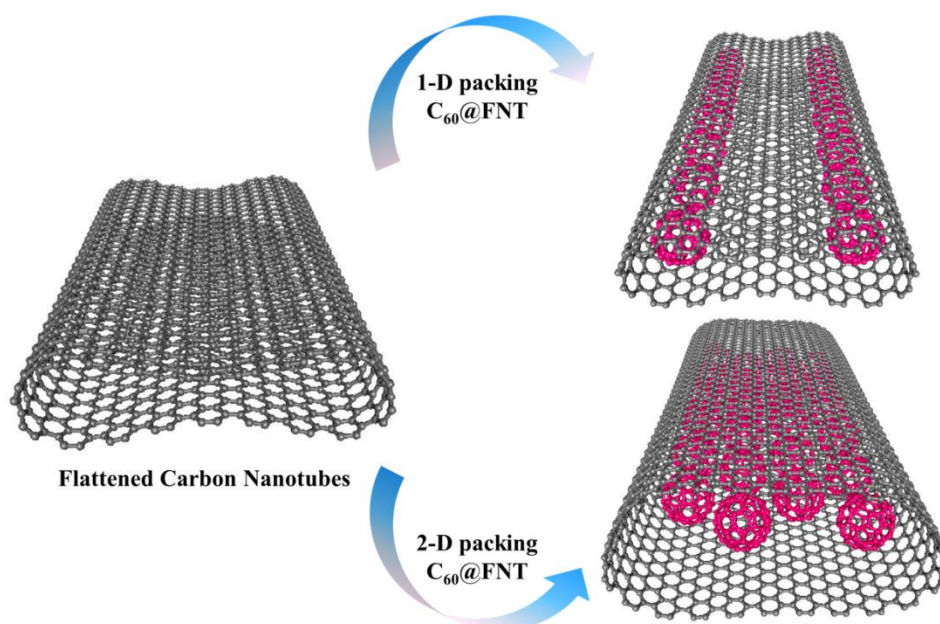


**Figure 3.1** Schematic diagram of the nanospace of FNT which enable atoms or molecules to aligned of not only in a 1D fashion but also in a 2D fashion.

### 3.1 Preparation of FNTs and inner space investigation

#### 3.1.1 Preparation of FNTs

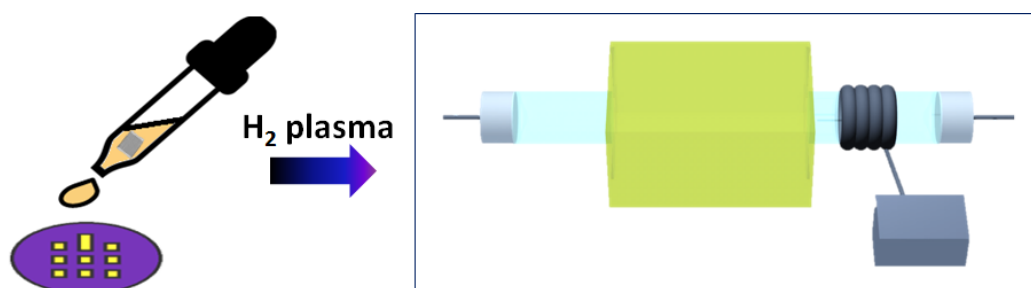


**Figure 3.2** Schematic diagrams of a Si grid and home-made H<sub>2</sub> plasma.

Details of the preparation of FNTs were described in Chapter 2. In brief, open-ended MWCNTs were sonicated in DCE or 1% (w/v) SDS solution typically for 1 h;

high-quality FNTs are prepared by this solution based method in a relatively high yield. The thus-prepared FNTs were dispersed in DCE and then dropped onto the TEM grid. The TEM grid is a kind of Si membrane grid as shown in Figure 3.2. To remove the residual solvent, the sample was subsequently heated at 473 K for 1 h under vacuum. Since the outer surface of FNTs was attached with amorphous carbon, the sample was subjected to H<sub>2</sub> plasma treatment in mild-condition for surface cleaning (Figure 3.3).

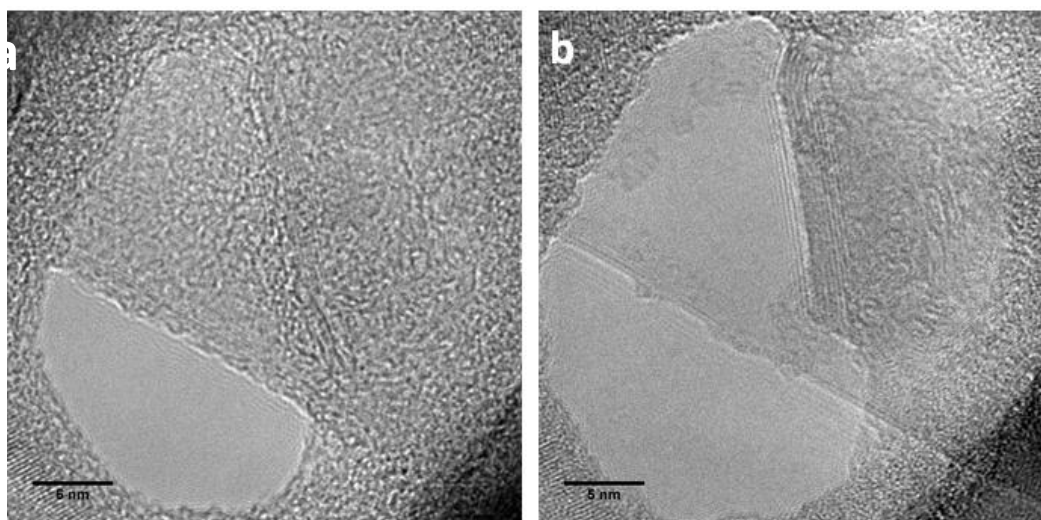


**Figure 3.3** TEM images of an identical FNT (a) before and (b) after 10 min H<sub>2</sub> plasma treatment.

### 3.1.2 Investigation of inner space of FNTs

FNTs were assembled on the TEM grid, purified by H<sub>2</sub> plasma, and TEM observation was performed to investigate the structural details. We performed high-angle annular dark-field scanning transmission electron microscopy (HAADF-STEM) observations and electron energy loss spectroscopy (EELS) measurements using an aberration corrected-TEM (JEOL-ARM200F), fitted with an EELS detector (Gatan Image Filter) and CEOS image and probe aberration correctors, operating at 80 kV.

In figures 3.4a and 3.4b, a six-layer FNT (formed by the flattening of a triple-wall CNT) without C<sub>60</sub> intercalation on the Si grid is showed by a high resolution TEM

image and a close-up image, respectively. Three linear contrasts at one edge of the FNT are showed in the close-up TEM image. A three-layer graphene was found the similar linear contrasts on the folded edge, where the lattice fringe of (002) graphene is observed [14]. Figure 3.4d shows the corresponding HAADF-STEM image, and the positions of EELS measurements are showed in Figure 3.4c by circles on the edge (position 1, blue circle) and flat region (position 2, red circle).

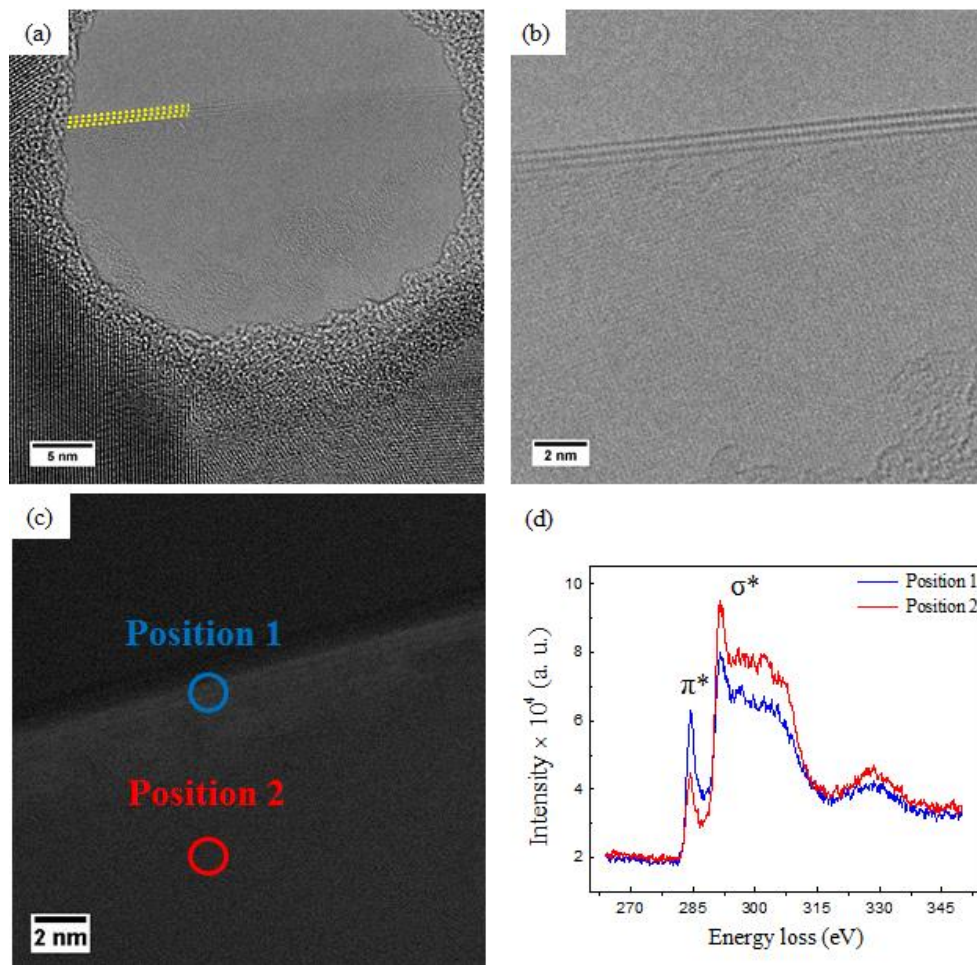


**Figure 3.4** (a) High resolution TEM image and (b) close-up images of a six-layer FNT (formed by the flattening of a triple-wall CNT) on a Si grid without  $C_{60}$  encapsulation; (c) The corresponding HAADF-STEM image of the same FNT. The positions of EELS measurement are showed by circles: blue circle, position 1, the edge; red circle, position 2, the middle flat region. (d) Typical EELS spectra recorded from position 1 and 2.

Typical EELS spectra of the FNT are showed in Figure 3.4d, recording from the edge (blue) and middle flat region (red), respectively. As can be seen clearly, the carbon K (1s) absorption edge is approximately at 285 eV. Sharp  $\pi^*$  peaks and large humps in the  $\sigma^*$  region (approximately 299 eV) were observed in the carbon K edge in the two spectra. These transitions can be distributed to the electronic transitions from the carbon 1s core orbital to the valence  $\pi^*$  and  $\sigma^*$  bands. The  $\pi^*$  and  $\sigma^*$  peaks are observed in spectral shapes, and this is typical for the  $sp^2$  hybridization of carbon atoms in FNTs. It is important to note that the  $\sigma^*$  fine structure in the flat region (red) of the FNT is more rounded than that in the edge (blue), but the intensity of the  $\pi^*$  peak is much weaker. The obtained results are in agreement with previous reports in which the intensity of the  $\pi^*$  peak is changed because of the different p-orbital directions on the rounded edge and the changing of  $\sigma^*$  fine structure is caused by the difference in curvature [15]. These results provide convincing proof for the barbell-like cross section of FNTs with unique low-dimensional hollow inner space.

## 3.2 Encapsulation of $C_{60}$ in FNTs

### 3.2.1 Encapsulation conditions

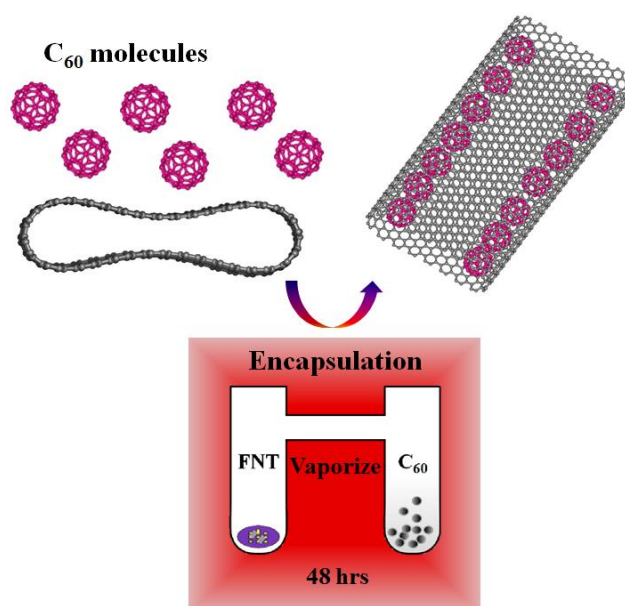


**Figure 3.5** Schematic diagram of the encapsulation process.

A clean Pyrex ampoule containing the clean open-ended FNTs and C<sub>60</sub> powder was sealed under high vacuum of 10<sup>-7</sup> Torr, and settled in an electric furnace at 723 ~ 773 K for 48 h or more (Figure 3.5). In the vacuum sealing process, we also performed 473 ~ 523 K heating for several hours to remove the solvent residue in C<sub>60</sub> power.

We studied the encapsulation temperatures from 673 K to 823 K and encapsulation times from 12 h to 72 h and found that the filling ratio was almost the same for the 723 ~ 773 K temperature range and an encapsulation time longer than 48 h. Similar structures are shown in Figures 4.6a and 4.6b, in which FNTs were covered with C<sub>60</sub> molecules and amorphous carbon, at 723 K for 48 h and at 773 K for 65 h, respectively.

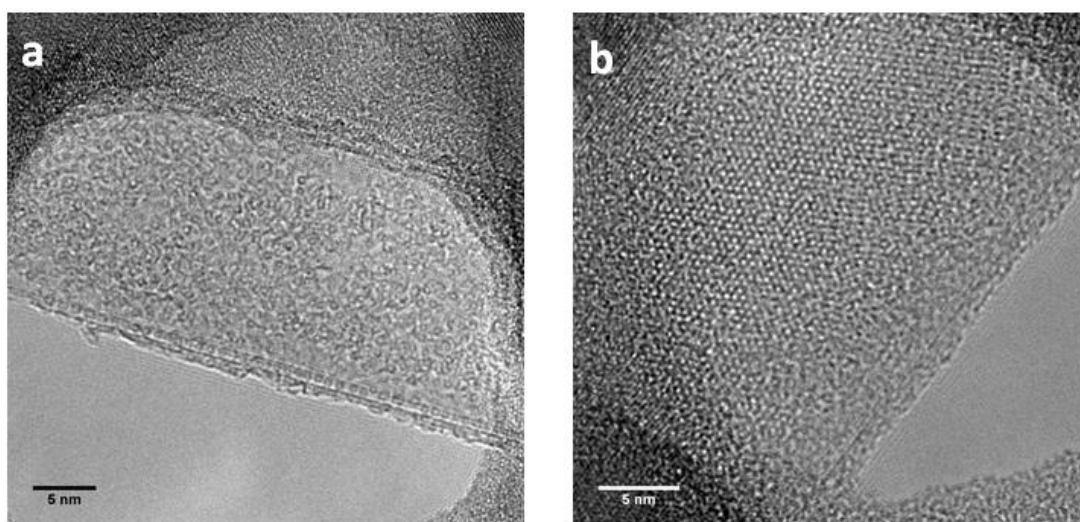


**Figure 3.6** TEM images of FNT after C<sub>60</sub> encapsulation at different conditions: (a) 723 K for 48 h; (b) 773 K for 65 h.

### 3.2.2 H<sub>2</sub> plasma treatment

Prior to detailed analysis of structures, H<sub>2</sub> plasma treatment and vacuum heating are performed in mild conditions to remove adsorbate of the outer surface of FNTs, such as amorphous carbon and C<sub>60</sub> molecules. This cleaning process guarantees that the observed C<sub>60</sub> molecules by TEM are only encapsulated C<sub>60</sub>.

The conditions of this H<sub>2</sub> plasma treatment have to be chosen with great care. As

shown in Figure 3.7,  $C_{60}$ @FNTs may be rare or are damaged after  $H_2$  plasma treatment. Usually,  $H_2$  plasma treatment works well, and subsequently, when we control the conditions at 8 W for 10 min, clean  $C_{60}$ @FNTs will be obtained.

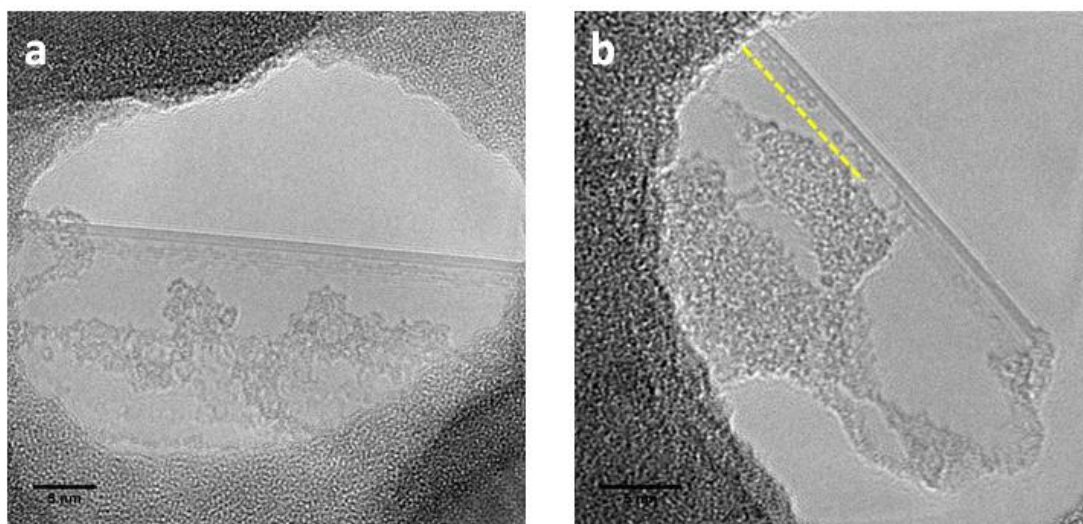


**Figure 3.7** TEM images of  $C_{60}$ @FNTs after (a) 10 W, 15 min and (b) 8 W, 15 min  $H_2$  plasma treatment.

### 3.3 Structure analysis

#### 3.3.1 One dimensional packing

In figures 3.8a and 3.8b, FNTs after  $C_{60}$  doping are showed by a high resolution TEM image and a close-up image respectively. The closed edges of FNT are clearly observed by the linear contrasts at the edges. Because the closed-edge is rounded structure, along the electron beam direction, the density of carbon atoms in the middle flat region is weaker than that at the closed edge, leading to the observation of strong linear contrasts at the edge of FNT. Circular contrasts aligned in 1D fashion are clearly observed along the edge of FNT, as shown in the figures. The circular contrasts are figured out as the encapsulated  $C_{60}$  molecules aligned in line. Inter circular distance of the molecules is 1.0 nm on average, and this is similar to the  $C_{60}$ - $C_{60}$  intermolecular distance that was reported in normal  $C_{60}$  peapods [7, 8].

Moreover, contrast from the circles is similar to that from the tubule walls, so the constituent atoms are probably carbon rather than a heavier element.

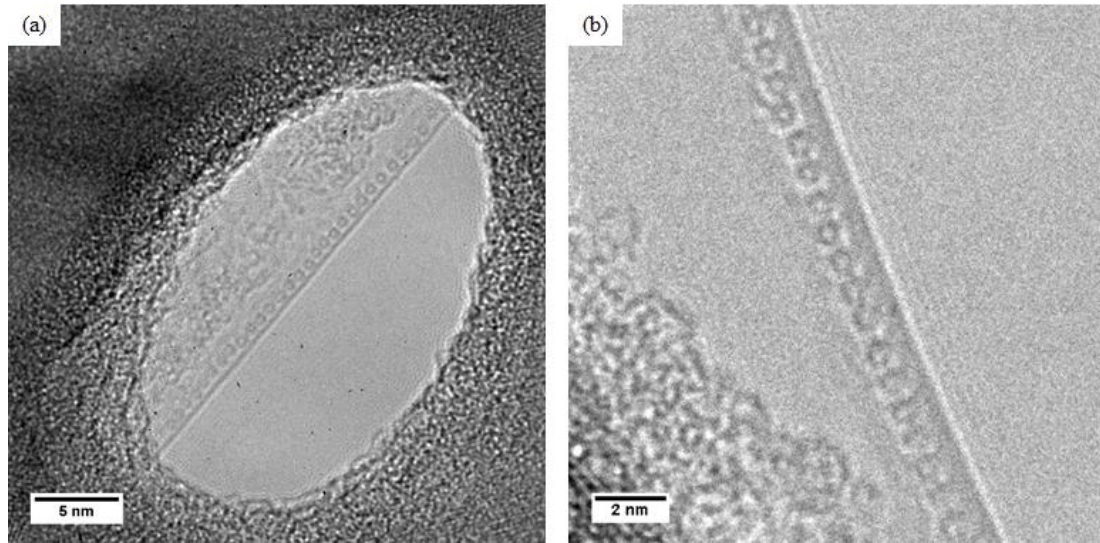


**Figure 3.8** (a) High resolution TEM image of a two-layer FNT (formed by the flattening of a single-wall CNT) on Si grid with  $C_{60}$  intercalation; (b) Close-up TEM image of a four-layer FNT (formed by the flattening of a double-wall CNT) on Si grid after  $C_{60}$  doping.

To verify the validity of the suggested  $C_{60}$ @FNT structure, TEM image simulations were performed on the basis of the multi-slice method. Along the electron beam direction samples are divided into several slices in this method, and a 2D plane is used for the projection of the electrostatic potential within each slice [16]. The propagation of the electron wave through these planes is treated using the small angle approximation. The unit cell was divided into 10 slices in this calculation. We set the defocus value to 73 nm, spherical aberration coefficient to 0.9 mm, beam convergence to 1.0 mrad, and defocus spread to 5 nm, respectively. The structural model was restricted to half of the FNT with one edge for computational efficiency. The structural model and the corresponding simulated TEM image of  $C_{60}$ @FNTs are showed in Figures 3.9a and 3.9c, respectively. It is clear that the simulated image accurately represents the main characteristics of the structure of observed  $C_{60}$ @FNT. As shown in the simulated image, a clear linear contrast is observed at the edge region

and circular contrasts are aligned in one-dimensionally along the rounded edge. The relative intensities are almost same in the linear and circular contrasts represented in the simulated image. Thus, the proposed structural model is identified with the real structure, and C<sub>60</sub>-FNT nanopeapod is successfully produced with 1D alignment of C<sub>60</sub> molecules along the rounded edge of FNT.

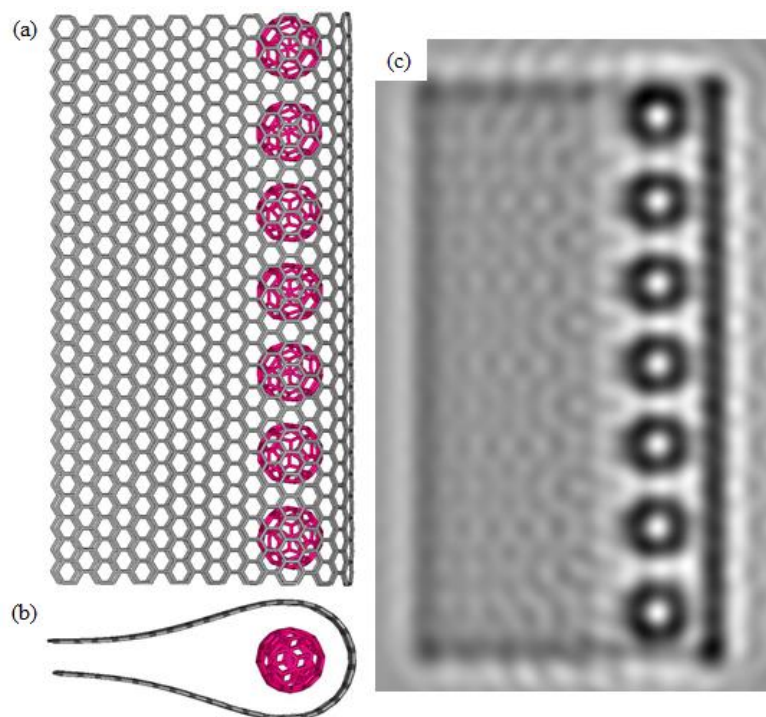


**Figure 3.9** Structural model of a one edge FNT with C<sub>60</sub> molecules in linear alignment at the edge: (a) top view, (b) cross section; (c) corresponding simulated TEM image.

### 3.3.2 Two dimensional packing

Moreover, it was found that the inner nanospace provided by FNTs can allow the alignment of molecules in a 1D fashion and in a 2D fashion. The attractive van der Waals interaction between the tube walls of CNTs induces the spontaneous deformation of large-diameter CNTs, which caused the flattening of FNTs [13, 17]. Since the van der Waals interaction is not too strong, the wall-to-wall van der Waals interaction in FNTs is similar in magnitude to further interaction between C<sub>60</sub>

molecules and walls of FNTs. Thus both the edge and middle flat area regions of FNTs can be doped with  $C_{60}$  molecules intercalation. This enables the alignment of  $C_{60}$  molecules in a 2D fashion that is strictly differ from the  $C_{60}$  molecules aligned in one-dimensional in normal nanopeapods.

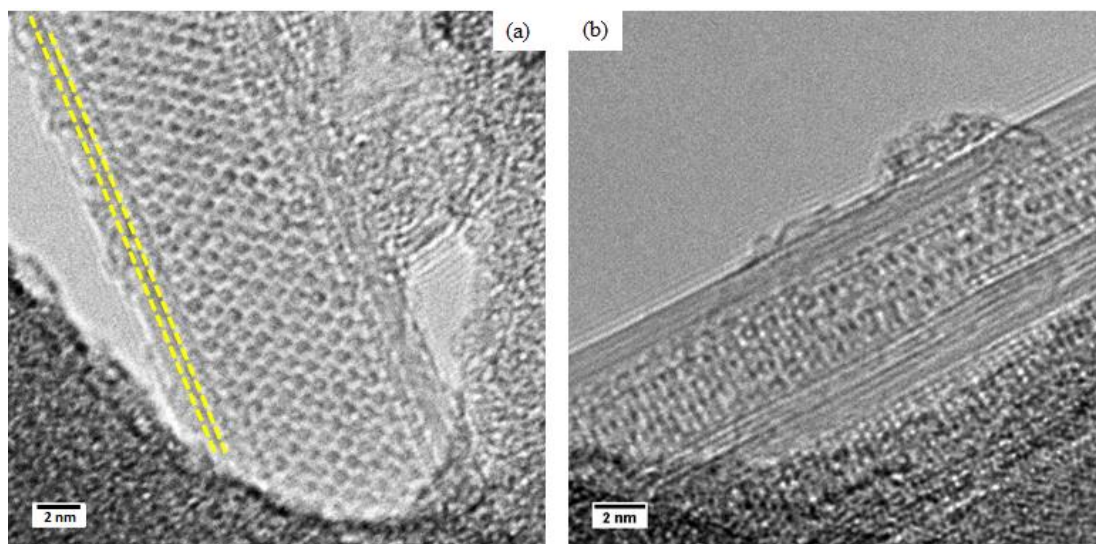


**Figure 3.10** (a) High resolution TEM image of a four-layer FNT (formed by the flattening of a double-wall CNT) with  $C_{60}$  molecules packed in 2D fashion inside. (b) High resolution TEM image of a MWCNT with  $C_{60}$  molecules packed in 3D inside.

FNT with full  $C_{60}$  intercalation is showed by a TEM image in Figure 3.10a, and  $C_{60}$  molecules are arranged in a 2D fashion. The FNT in Figure 3.10a has a width of approximately 10 nm. The observed tube should not be a large-diameter CNT but a FNT because the threshold diameter of the flattening of a double-wall CNT is approximately 4 nm, much smaller than the width of observed structure [18]. The edges of the four-layer FNT (deformation of a double-wall CNT) show parallel linear contrasts, and 10 columns of circular contrast are observed in side of the FNT with approximately diameter of 0.7 nm in each circular contrast. In addition, a distance of approximately 0.3 nm from the FNT walls is observed in the edge columns of  $C_{60}$  (Figure 3.10a). Inter circular contrast has a distance about 1.02 nm on average. The inner circular distance shows a standard deviation about 0.011, and this identifies with the  $C_{60}$  molecular size [8]. As s comparison figure, a TEM image of  $C_{60}$ @MWCNT is

showed in Figure 3.10b. In this MWCNT (four-wall CNT), 3D packing  $C_{60}$  molecules are clearly observed. The 3D arrangement of  $C_{60}$  is feasible in this MWCNT with a diameter of the inner CNT larger than 4 nm.

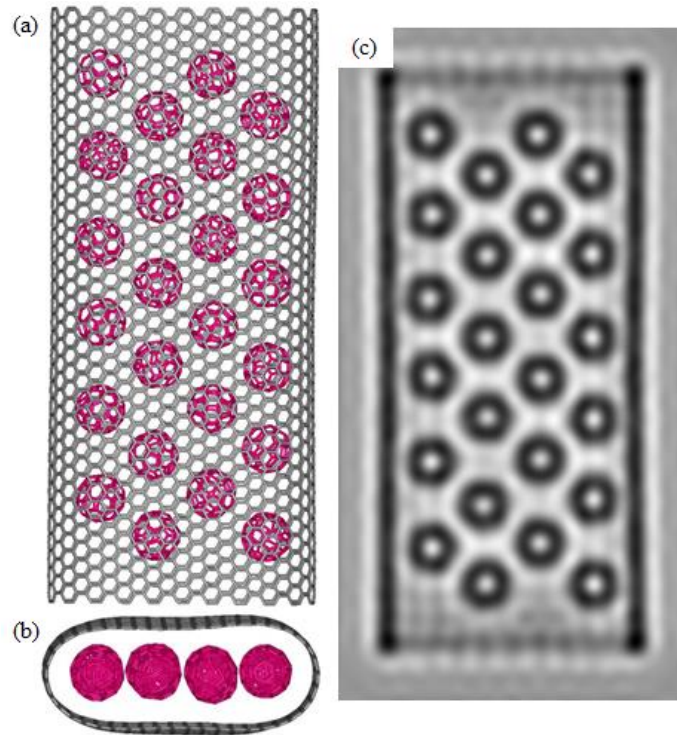


**Figure 3.11** Structural model of a FNT with 2D arrangement of  $C_{60}$  molecules encapsulation: (a) top view, (b) cross section; (c) corresponding simulated TEM image.

Inspection of the figure shows that the complicated image contrasts inside of the MWCNT are caused by the expressively overlap of circular contrasts with each other. Because the  $C_{60}$  molecules pack in 3D fashion, at the largest 4 ~ 5 encapsulated  $C_{60}$  molecules are observed along the electron beam direction [8]. This causes that the image contrast in Figure 3.10b is complicated overlap. Therefore the clear array of circular contrasts observed in Figure 3.10a is assigned to occur from the  $C_{60}$  molecules packed in 2D fashion inside the FNT.

According to the observed structure showed in Figure 3.10a, a possible structure model of  $C_{60}@FNT$  has been formulated in Figure 3.11a. To simplify a smaller width

FNT is applied in the structural model. As well known that the face-centered-cubic (fcc) structure of bulk  $C_{60}$  is the stable crystal structure at room temperature, therefore, 2D packed  $C_{60}$  molecules in the structure model are same with the structure of the (111) plane of the fcc structure. The simulated TEM image on basis of the structure model is showed in Figure 3.11c. It is clearly showed that the observed image is accurately reproduced by the simulated image, supporting the validity of our formulated structural model.

### 3.3.3 Other kinds of packing

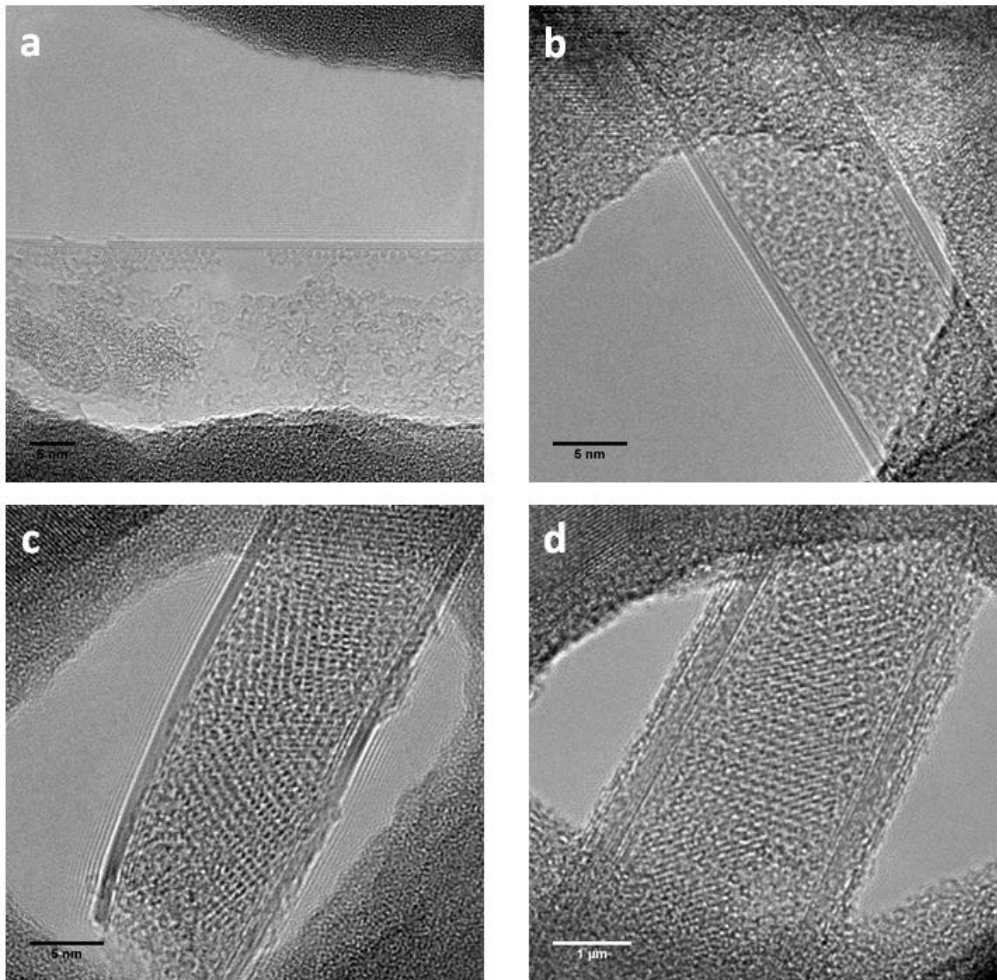


**Figure 3.12** TEM images of different kinds of  $C_{60}$  molecules packing inside FNTs: (a) a four-layer FNT (formed by the flattening of a double-wall CNT) with  $C_{60}$  intercalation on the edge part in two or three lines, between 1D and 2D packing; (b)

$C_{60}$  molecules and amorphous carbon packed randomly in 2D inside a six-layer (formed by the flattening of a triple-wall CNT); (c) and (d) a six-layer FNT and a few-layer FNT with 3D packing  $C_{60}$  molecules intercalation.

In addition to the 1D or 2D packing mentioned above, in some rare cases, we also observed other types of  $C_{60}$  molecules packing inside FNTs. Figure 3.12a shows a TEM image of a four-layer FNT (formed by the flattening of a double-wall CNT) with  $C_{60}$  encapsulation in two or three lines on the edge region. This can be considered as an intermediate molecular packing that is between 1D and 2D. We also found that the  $C_{60}$  molecules and amorphous carbon mixed together inside FNT and formed a random 2D-like packing shown in Figure 3.12b. Figures 3.12c and 3.12d show  $C_{60}$  molecules packed in a 3D structure as the overlap between circle contrasts can be clearly observed. However, these types of packing were very rarely observed, and their detailed structures were difficult to analyze.

### 3.4 Conclusions

In this part of my work, FNTs and  $C_{60}$  fullerenes are composited as a new type of hybrid nanostructures with unique structures. The validity of rounded hollow space at the close edges of FNTs was identified by the TEM observations and EELS measurements. A brand new hybrid material ( $C_{60}$ @FNTs), where  $C_{60}$  molecules are aligned in 1D fashion at the closed edges of FNTs, is provided by the intercalation of  $C_{60}$  molecules into the edge space. Furthermore,  $C_{60}$  molecules packed in a 2D fashion has been originally realized in the middle flattened region of FNTs. We performed TEM observations and image simulation on the basis of the multi-slice method to study these structures. This new type of nanocarbon materials exhibit quite fascinating structures on the basis of TEM observations. Additionally, the experimental results declare that FNTs can be intercalated with various atoms and molecules, enabling the potential of preparing new kinds of novel hybrid materials on the basis of FNTs.

## References

1. H. W. Kroto, J. R. Heath, S. C. O'Brien, R. F. Curl, R. E. Smalley. C<sub>60</sub>: Buckminsterfullerene. *Nature* **1985**, 318, 162-163.
2. S. Iijima, T. Ichihashi. Single-shell carbon nanotubes of 1-nm diameter. *Nature* **1993**, 363, 603-605.
3. P. M. Ajayan, S. Iijima. Capillarity-induced filling of carbon nanotubes. *Nature* **1993**, 361, 333-334.
4. Z. Y. Wang, K. K. Zhao, H. Li, Z. Liu, Z. J. Shi, J. Liu, K. Suenaga, S. K. Joung, T. Okazaki, Z. X. Jin, et al. Ultra-narrow WS<sub>2</sub> nanoribbons encapsulated in carbon nanotubes. *Journal of Materials Chemistry* **2011**, 21, 171-180.
5. R. Kitaura, R. Nakanishi, T. Saito, H. Yoshikawa, K. Awaga, H. Shinohara. High-yield synthesis of ultrathin metal nanowires in carbon nanotubes. *Angewandte Chemie International Edition* **2009**, 48, 8298-8302.
6. R. Kitaura, N. Imazu, K. Kobayashi, H. Shinohara. Fabrication of metal nanowires in carbon nanotubes via versatile nano-template reaction. *Nano Letters* **2008**, 8, 693-699.
7. B. W. Smith, M. Monthieux, D. E. Luzzi. Encapsulated C<sub>60</sub> in carbon nanotubes. *Nature* **1998**, 396, 323-324.
8. K. Hirahara, S. Bandow, K. Suenaga, H. Kato, T. Okazaki, H. Shinohara, S. Iijima. Electron diffraction study of one-dimensional crystals of fullerenes. *Physical Review B* **2001**, 64, 115420.
9. K. Hirahara, K. Suenaga, S. Bandow, H. Kato, T. Okazaki, H. Shinohara, S. Iijima. One-dimensional metallofullerene crystal generated inside single-walled carbon nanotubes. *Physical Review Letters* **2000**, 85, 5384-5387.
10. R. Kitaura, H. Shinohara. Carbon-nanotube-based hybrid materials: nanopeapods. *Chemistry – An Asian Journal* **2006**, 1, 646-655.
11. T. Shimada, T. Okazaki, R. Taniguchi, T. Sugai, H. Shinohara, K. Suenaga, Y. Ohno, S. Mizuno, S. Kishimoto, T. Mizutani. Ambipolar field-effect transistor behavior of Gd@C<sub>82</sub> metallofullerene peapods. *Applied Physics Letters* **2002**, 81,

4067-4069.

12. J. Lee, H. Kim, S. J. Kahng, G. Kim, Y. W. Son, J. Ihm, H. Kato, Z. W. Wang, T. Okazaki, H. Shinohara, et al. Bandgap modulation of carbon nanotubes by encapsulated metallofullerenes. *Nature* **2002**, 415, 1005-1008.
13. D. H. Choi, Q. Wang, Y. Azuma, Y. Majima, J. H. Warner, Y. Miyata, H. Shinohara, R. Kitaura. Fabrication and characterization of fully flattened carbon nanotubes: a new graphene nanoribbon analogue. *Scientific Reports* **2013**, 3, 1617.
14. K. Kim, Z. Lee, B. D. Malone, K. T. Chan, B. Alemán, W. Regan, W. Gannett, M. F. Crommie, M. L. Cohen, A. Zettl. Multiply folded graphene. *Physical Review B* **2011**, 83, 245433.
15. K. Suenaga, E. Sandré, C. Colliex, C. J. Pickard, H. Kataura, S. Iijima. Electron energy-loss spectroscopy of electron states in isolated carbon nanostructures. *Physical Review B* **2001**, 63, 165408.
16. J. M. Cowley, A. F. Moodie. The Scattering of Electrons by Atoms and Crystals. I. A New Theoretical Approach. *Acta Crystallographica* **1957**, 10, 609-619.
17. J. A. Elliott, J. K. W. Sandler, A. H. Windle, R. J. Young, M. S. P. Shaffer. Collapse of single-wall carbon nanotubes is diameter dependent. *Physical Review Letters* **2004**, 92, 095501.
18. C. Zhang, K. Bets, S. S. Lee, Z. Sun, F. Mirri, V. L. Colvin, B. I. Yakobson, J. M. Tour, R. H. Hauge. Closed-edged graphene nanoribbons from large-diameter collapsed nanotubes. *ACS Nano* **2012**, 6, 6023-6032.

## Chapter 4

### **Fabrication and In-situ TEM Characterization of Freestanding Graphene Nanoribbons Devices**

Graphene nanoribbon (GNR), the one-dimensional counterpart of graphene, is one of the most remarkable examples of size- and structure-dependent properties [1]. Theoretical works on GNRs have pointed out that GNRs possess width-dependent bandgap and peculiar structure-dependent edge states [2]. The existence of a sizable bandgap in the narrow GNRs, which is not the case in the zero-gap graphene semiconductor, has attracted a great deal of attention because of possible application of GNRs in future nanoelectronic devices [3-8]. The spin-polarized gapless edge state appears at the zigzag edge of GNRs; this has also attracted significant attention because of possible spin-dependent transport and all-carbon magnet [9, 10].

However, experimental investigations of structure-dependent properties of GNRs are not straightforward. Electronic transport measurements on GNRs prepared by lithographical patterning or hydrogen etching have been performed and have successfully shown that the transport gap is roughly dependent on GNR width [1, 11]. However, the observed gap is a transport gap and not an intrinsic bandgap, and the observed transport gap is strongly influenced by the roughness of edge structure and substrate underneath. In addition, characterization of the precise atomic structure of GNRs is difficult, leading to difficulty in understanding GNR's properties on the basis of their structure [12-14]. Complete understanding of structure-dependent properties of GNRs has been desired to explore the possibility of the use of GNRs in nanoelectronic and nanospintronic devices.

The purpose of this part of the work is to develop an experimental technique for the investigation of intrinsic structure-dependent properties of GNRs. For this purpose, a seamless combination of precise structural characterization and electronic property measurement is essential. To realize such a combination, our strategy is to use TEM

for structural characterization and substrate-free suspended GNRs to investigate the intrinsic properties. Figure 4.1 shows a schematic representation of our approach. A substrate-free GNR suspended between electrodes is mounted on the top of our homemade TEM holder for in-situ structure and electronic property characterization. This procedure leads to a direct correlation between the atomic structure of GNRs and their transport properties.

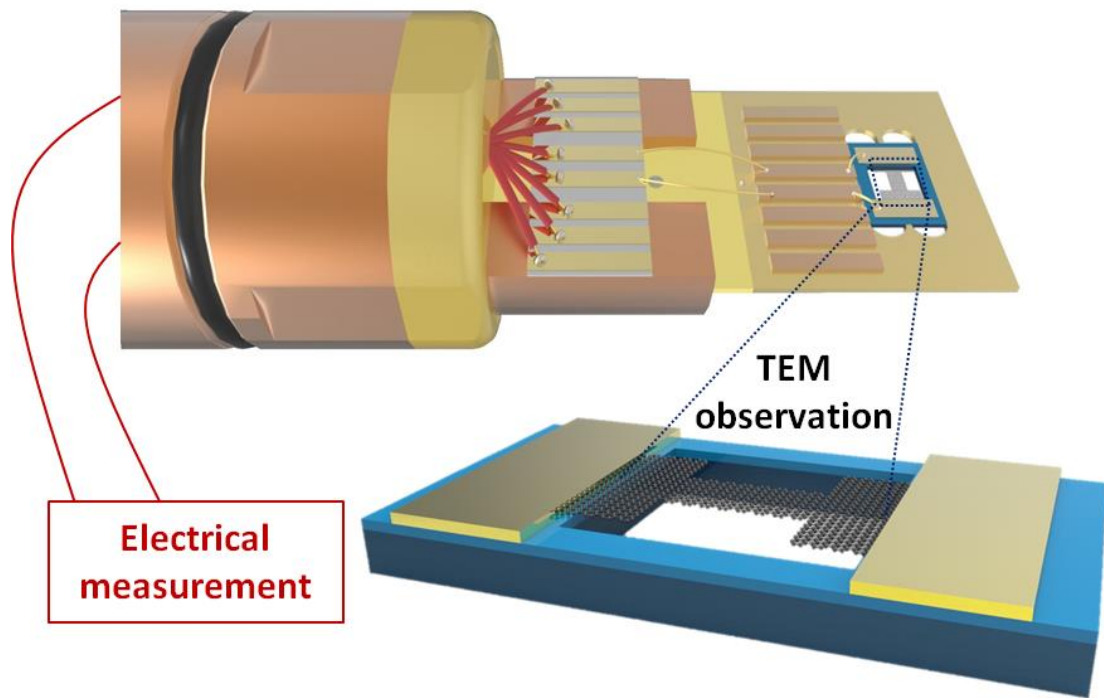


**Figure 4.1** Schematic representation of our approach showing how to combine the TEM observation and electrical measurement.

## 4.1 Fabrication of freestanding graphene devices

### 4.1.1 Preparation of graphene

To obtain high-quality graphene, we have performed CVD at 1323 K using methane as a carbon source and copper as a substrate [15]. We used Ar as carrying gas, pure H<sub>2</sub> for 1 h annealing, and Ar/H<sub>2</sub>/CH<sub>4</sub> as the carbon source for the 2 h of reaction. The crystallinity and grain size of the obtained graphene varied from 10 to 100 $\mu$ m, as

shown in the scanning electron microscope (SEM, JSM-6340F, JEOL) image (Figure 4.2a).

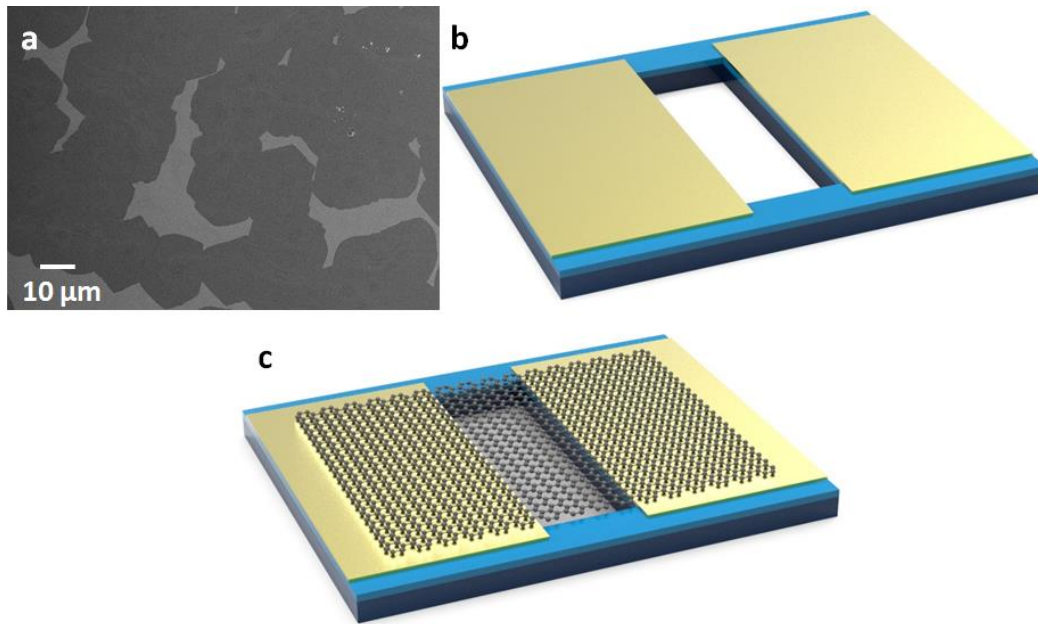


**Figure 4.2** (a) A typical SEM image of the CVD-grown graphene on copper with a grain size about 20 μm; The schematic diagram of (b) pre-fabricated substrate with possessing electrodes and a penetrating hole, (c) the CVD-grown graphene covered the electrodes and hole.

After CVD growth, the copper substrate was dissolved in  $\text{FeNO}_3$  solution for more than 3 h and washed in purified water for several hours. Graphene was then directly transferred onto a pre-fabricated substrate with electrodes and a penetrating hole, as shown in Figures 4.2b and 4.2c.

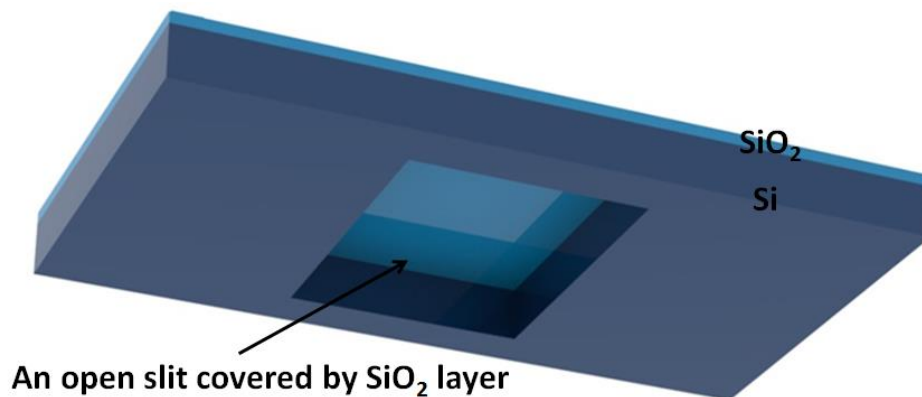


**Figure 4.3** The schematic diagram of the special Si substrate with an open slit covered by a SiO<sub>2</sub> layer.

Alternatively, the obtained graphene was transferred to another type of special substrate (Figure4.3).

We also used graphene prepared by mechanical exfoliation of Kish graphite in the experiment. The exfoliated graphene was transferred onto a Si substrate with an open slit covered by a SiO<sub>2</sub> layer (Figure 4.3) by a deterministic transfer method (Figure 4.4) [16]. Kish graphite was first peeled off from Nitto tape and then pasted on PDMS. Following this, monolayer or few-layer graphene were located on PDMS by an optical microscope, and the layer-numbers were verified by Raman measurements.

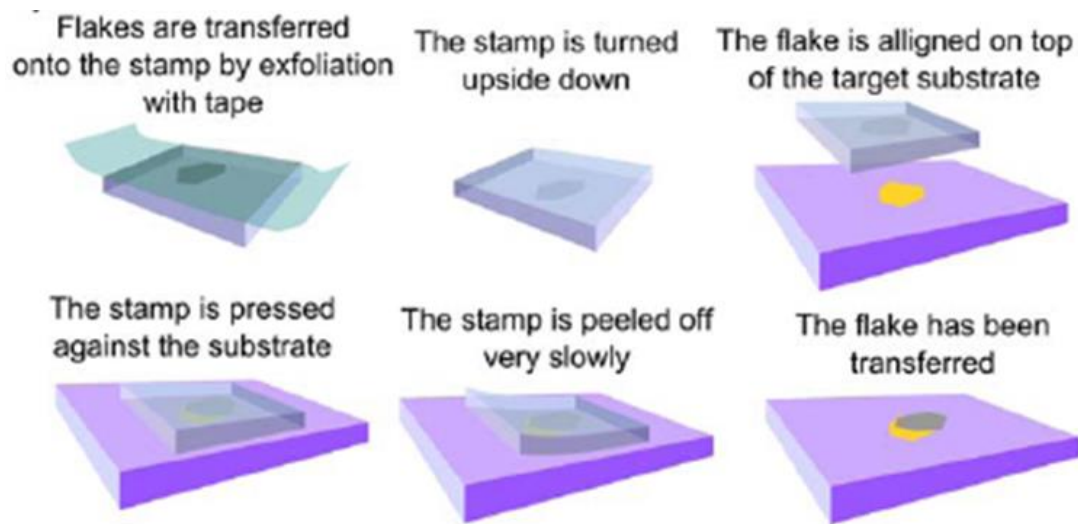


**Figure 4.4** Diagram of the steps involved in the deterministic transfer of anatomically thin flake onto a user-defined location [16].

Graphene can be observed by an optical microscope because of its 2.3% absorbance. We used optical microscope (DM2500M, Leica) to locate CVD-grown and exfoliated graphene on SiO<sub>2</sub>/Si substrates. In addition, the optical microscope was used to verify the developing conditions and electrode morphology. Monolayer graphene will be transferred to the special substrate and just bridged the slit, as shown in Figure 4.5b.

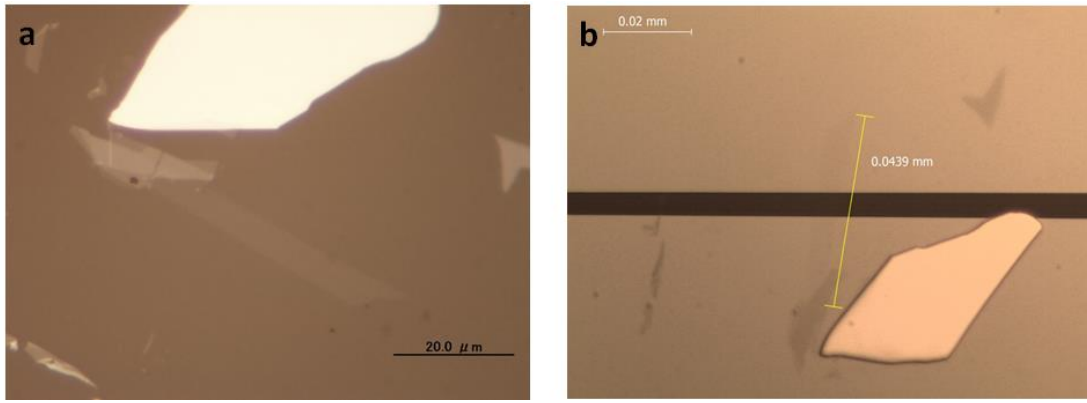


**Figure 4.5** Optical microscopy images of (a) an exfoliated monolayer graphene on PDMS and (b) the monolayer graphene after transferred onto the special substrate (the black part is the slit).

#### 4.1.2 Patterning on graphene

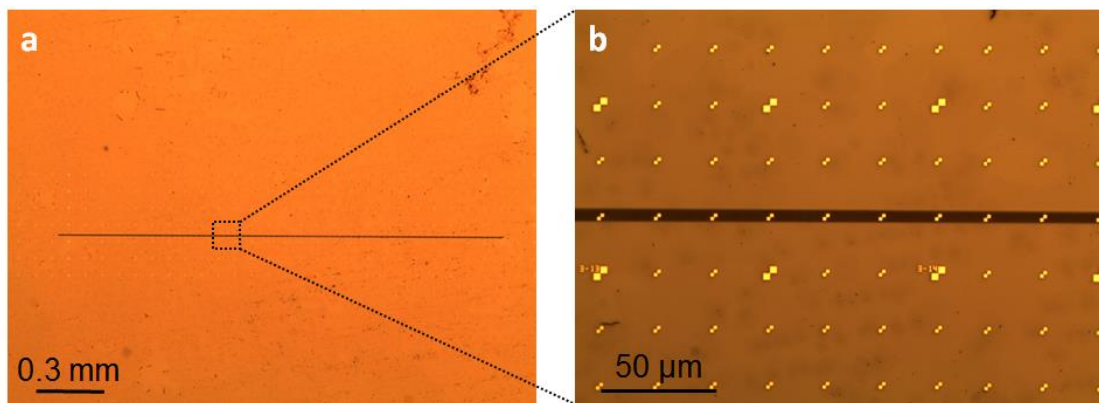


**Figure 4.6** Optical microscopy images of (a) CVD-grown graphene after transferred and (b) close-up graphene on the marked substrate.

Usually, CVD-grown graphene is wafer size (Figure 4.6) and cannot be used directly for devices.

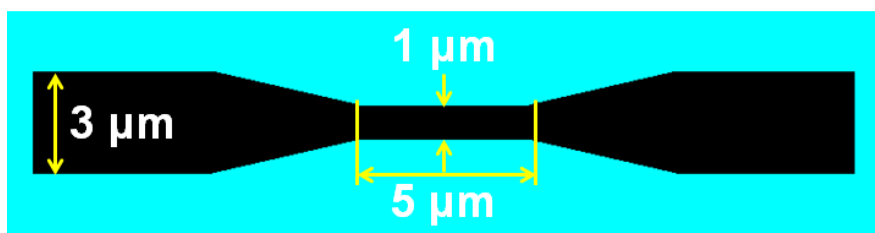


**Figure 4.7** EBL design for patterning graphene.

Prior to the transfer of the CVD-grown graphene onto special substrates, marks were prepared following EBL exposure and the deposition of Cr/Au. We used marks to locate the graphene bridged in the slit in one grain without impurities.

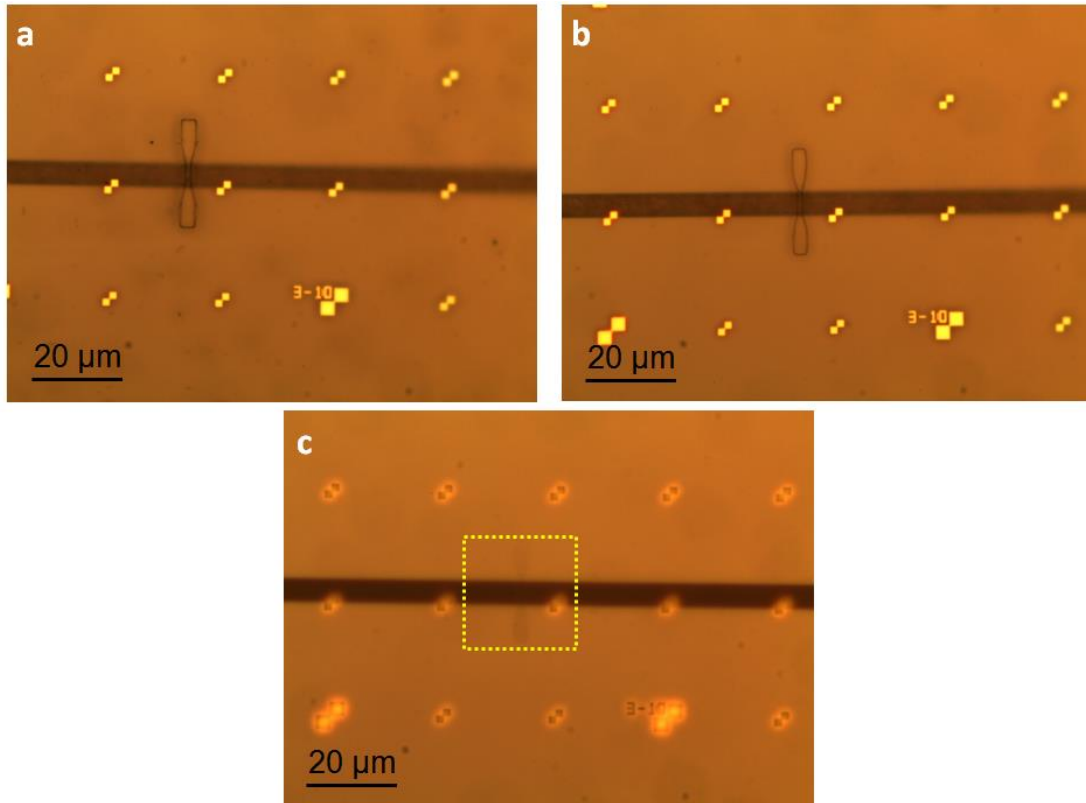


**Figure 4.8** Optical microscopy images of CVD-grown graphene after (a) EBL, (b) O<sub>2</sub> plasma and (c) removing the photoresist.

Sometimes, the shape of exfoliated graphene is not suitable for a certain device design. In that case, graphene must be patterned to enable the fabrication of devices. Graphene was then patterned by EBL exposure using the design shown in Figure 4.7. After exposure and development, graphene was covered by the photoresist in a pattern (Figure 4.8a). The substrate was then treated by O<sub>2</sub> plasma for 5 min to remove the graphene without photoresist protection (Figure 4.8b), and patterned graphene was obtained after removing the photoresist (Figure 4.8c).

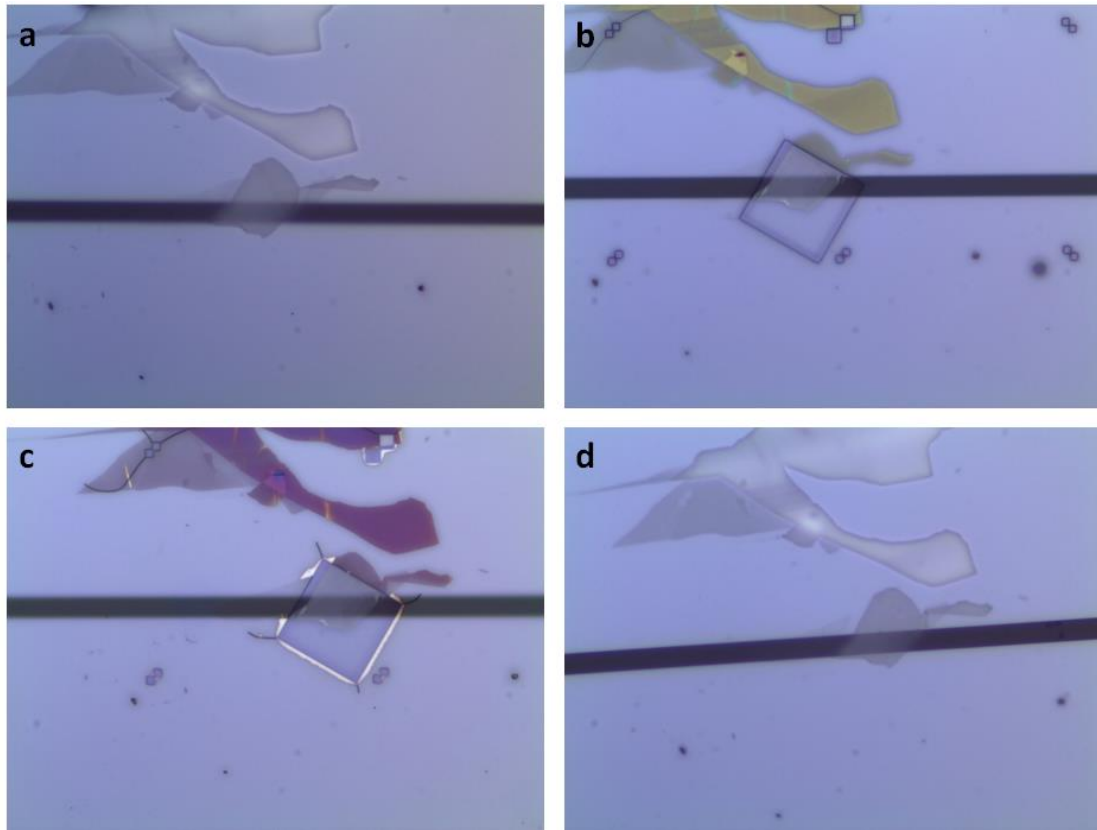


**Figure 4.9** Optical microscopy images of (a) an exfoliated graphene (light grey) connected with a graphite flake (dark grey); (b) The exposed graphite part in the square; (c) After 8 min O<sub>2</sub> plasma etching; (d) Patterned graphene after removing photoresist and disconnected with graphite flake.

For the exfoliated graphene, as shown in Figure 4.9a, the targeted graphene is connected with a graphite flake, making the fabrication of a three-terminal device challenging. We therefore used EBL exposure to protect the targeted graphene by photoresist and etched the graphite flake by O<sub>2</sub> plasma (Figure 4.9b and 4.9c). We then modified the graphene to make it suitable for making a three-terminal device (Figure 4.9d).

## 4.2 Fabrication of graphene devices

We used EBL to design and fabricate patterned electrodes on graphene. For CVD-grown graphene, after patterning, two-terminal electrodes were fabricated after

EBL exposure and deposition of 5nm Cr and 100nm Au (Figure 4.10a). Between five and nine devices can be obtained in one substrate.

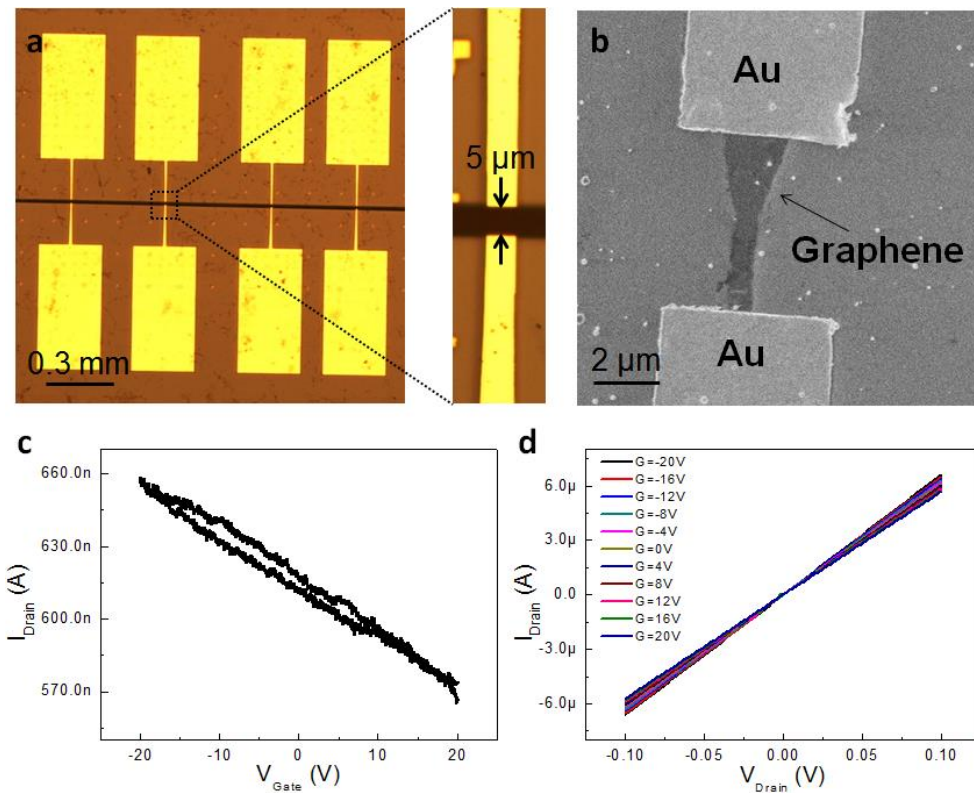


**Figure 4.10** (a) optical microscopy image and (b) SEM image of the patterned CVD-grown graphene with 5 nm Cr and 100 nm Au electrodes. (c) and (d) Transfer and output curves of the graphene device,  $V_{SD} = 10$  mV.

Transfer and output properties (Figure 4.10c and 4.10d) were measured for each CVD-grown graphene device, and usually, p-type metallic behavior was observed with a resistance of  $10 \sim 15$  k $\Omega$ , which is reasonable for an approximately  $1 \mu\text{m}$  wide graphene ribbon.

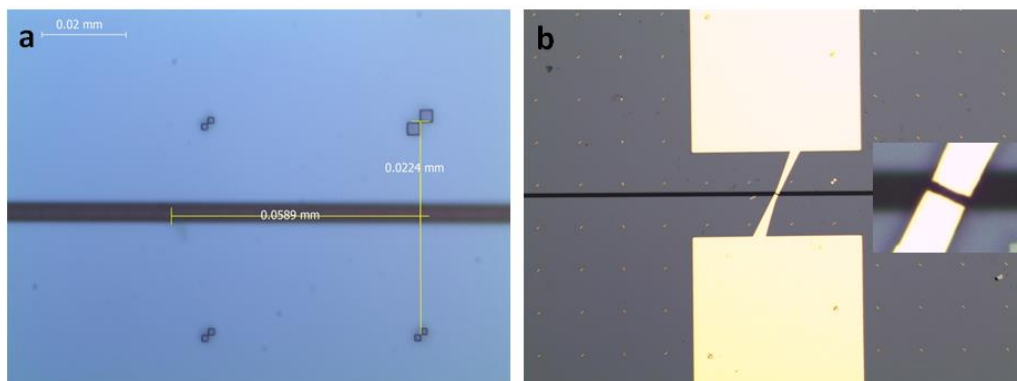


**Figure 4.11** Optical microscopy images of (a) an exfoliated graphene located by photoresist marks and (b) 5 nm Cr and 100 nm Au electronic contacts made on this graphene with a gap of 2  $\mu\text{m}$  (inset).

For exfoliated graphene, marks were first exposed on the substrate. After the development, we use this type of photoresist mark to locate graphene (Figure 4.11a) and then write the electrodes' pattern. As mentioned above, electronic contacts were made by deposition of 5nm Cr and 100nm Au (Figure 4.11b). Electrical measurement shows ambipolar transport behavior and shifted Dirac points because of the doping effect of the Si substrate (Figure 4.12).

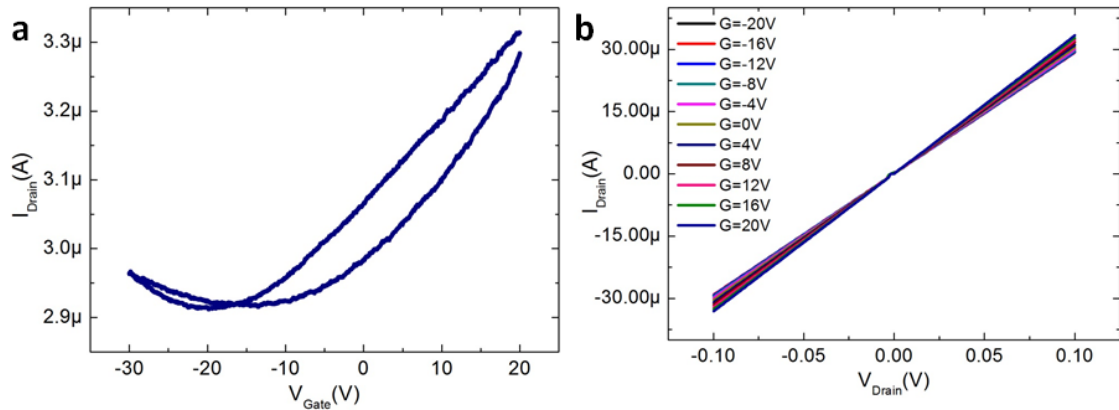


**Figure 4.12** Transfer (a) and output (b) curves of an exfoliated graphene devices,  $V_{SD} = 10 \text{ mV}$ .

## 4.3 Preparation of freestanding structures

### 4.3.1 Laser etching

CVD-grown graphene was transferred onto a pre-fabricated substrate with electrodes and a penetrating hole (Figure 4.2c); a high-power laser was used to cut graphene to less than 10 $\mu\text{m}$  wide (Figure 4.13), and hydrogen plasma was used to purify graphene because amorphous carbon accumulated very soon at high temperature during laser etching.

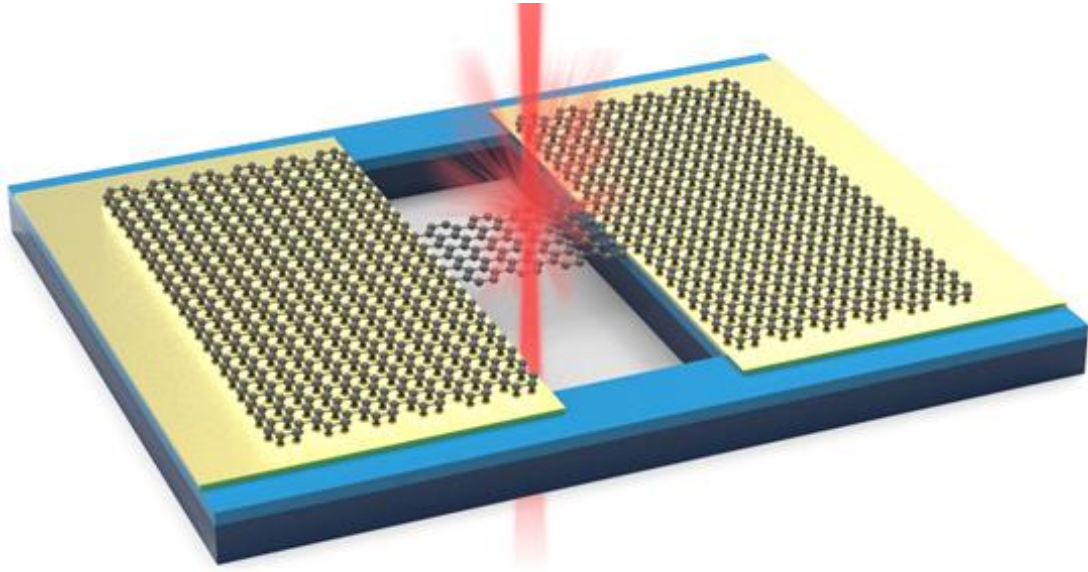


**Figure 4.13** Schematic diagram of laser etching on CVD-grown graphene.

Figure 4.14a shows a typical TEM image of graphene suspended between electrodes; this structure was prepared with CVD-grown monolayer graphene through a transfer onto the pre-fabricated substrate. Dark contrasts at both sides in the TEM image correspond to the pre-patterned Pt electrodes, and weak contrast arising from graphene is observed between the electrodes; dark spots on the graphene arise from residues of Cu used in CVD growth. The electron diffraction pattern (Figure 4.14b) of suspended graphene shows sharp spots with six-fold symmetry, clearly demonstrating the successful transfer of monolayer graphene. Figure 4.14c shows a TEM image obtained after narrowing of the suspended graphene by high-power laser irradiation. As seen in Figure 4.14c, graphene width is narrowed down to  $10\mu\text{m}$ , and edges of the shaped graphene are rolled up, leading to linear contrasts at the edge region. The rolling up is probably caused by vibration of edges due to the laser-induced high temperature. Figure 4.14d shows an I-V curve of the narrowed graphene with the linear relation between I and V, giving resistivity of approximately  $9.0\times 10^{-7}\ \Omega\cdot\text{m}$ . The obtained resistivity is comparable with the reported values (approximately  $2.0\times 10^{-7}\ \Omega\cdot\text{m}$ ) obtained using two-terminal devices [20].

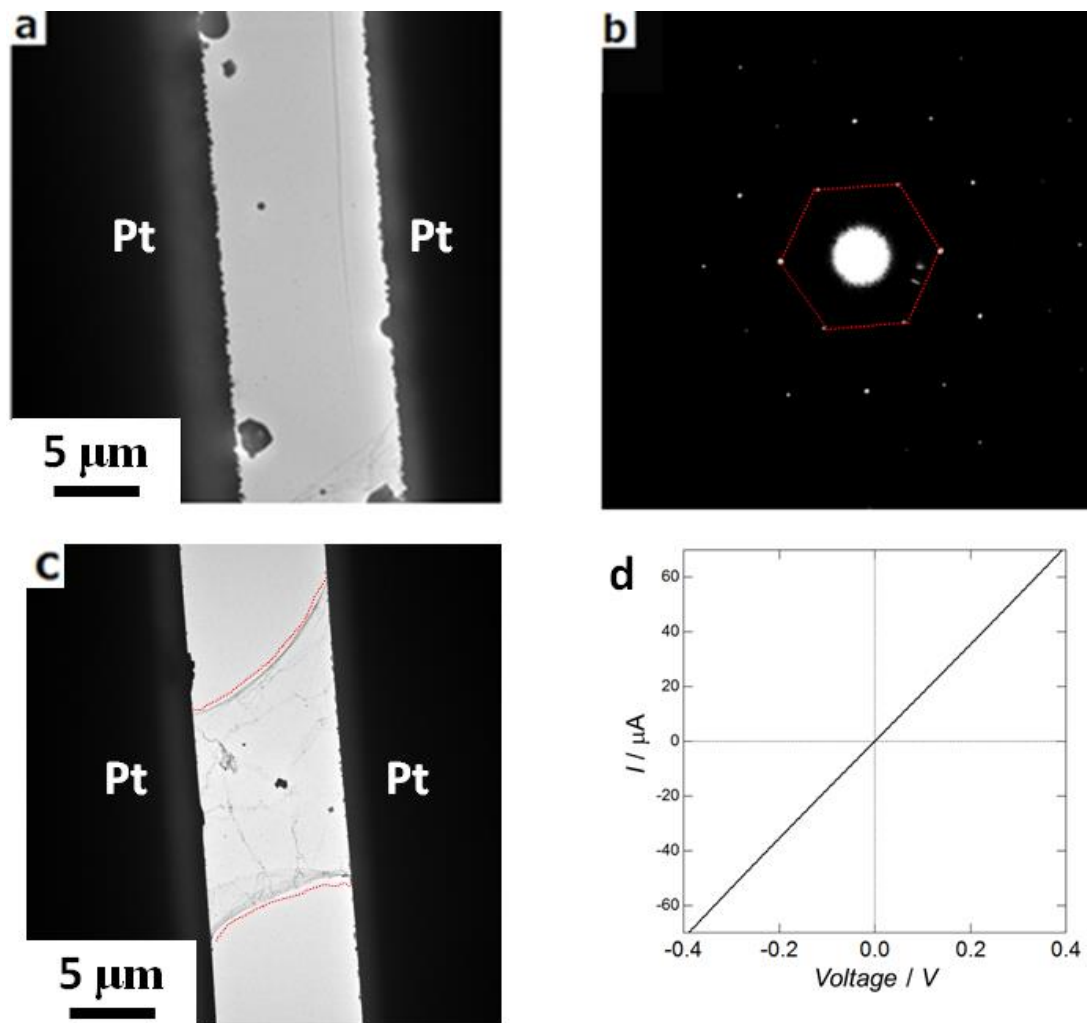


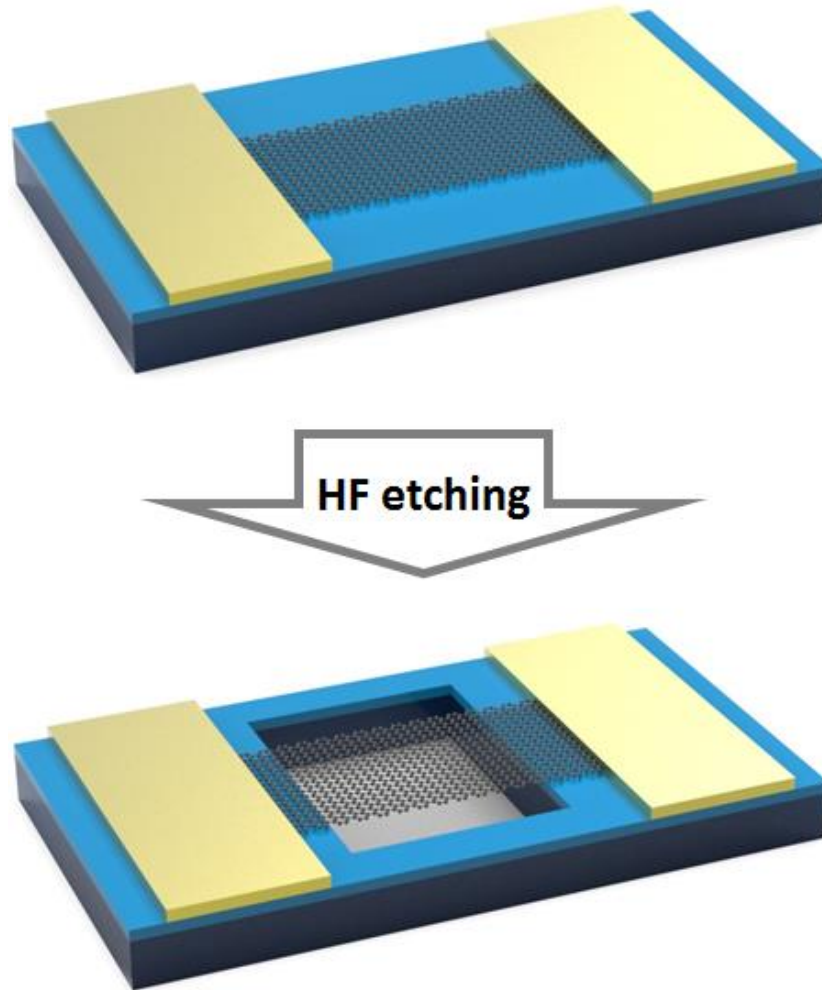
**Figure 4.14** (a) TEM image of a CVD-grown graphene after transferred onto a pre-fabricated substrate and (b) corresponding diffraction pattern; (c) a 10  $\mu\text{m}$  wide graphene bridged two electrodes after laser etching; (d) I-V curve of the freestanding graphene devices in (c).

### 4.3.2 HF etching

For graphene devices fabricated on the special substrates (Figure 4.3), regardless of whether the graphene is CVD-grown or exfoliated,  $\text{SiO}_2$  underneath graphene will be etched away (Figure 4.15) by the buffered HF solution ( $\text{HF} : \text{NH}_4\text{F} = 1 : 5$ ).

However, we found that graphene could be very easily damaged during the solution process because of the surface tension. We must therefore protect graphene in the experiment using a protective agent that is superior to the Au bar or photoresist used

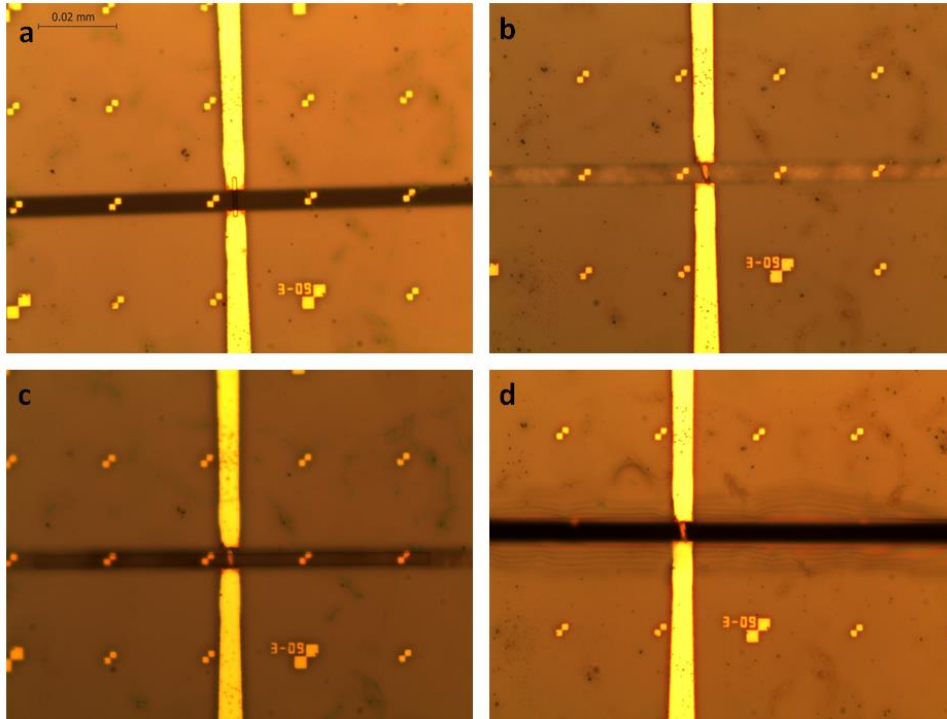
as the protection.



**Figure 4.15** Schematic diagram of graphene device before and after HF etching.

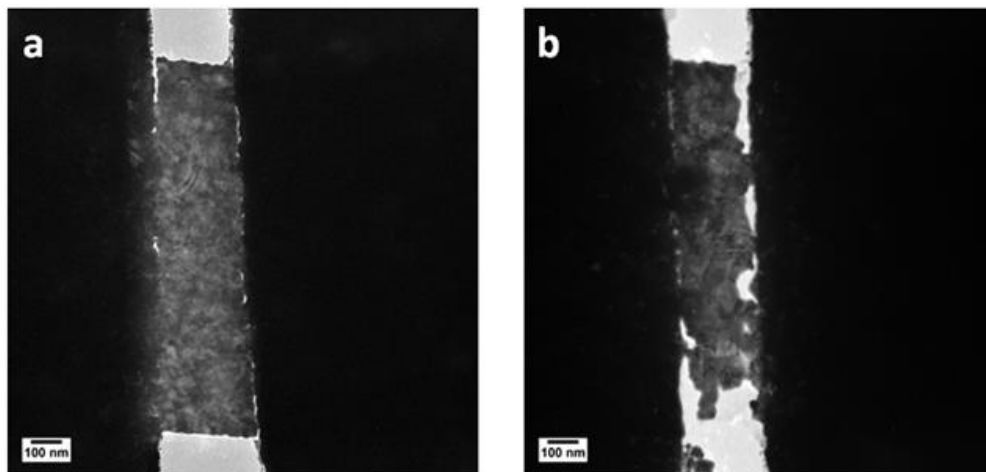
An Au bar was used to protect CVD-grown graphene in the HF etching process. The Au bar was patterned by EBL, and 10 ~ 20 nm thick Au film was deposited, following which the whole substrate was immersed into buffered HF solution for 5min (Figure 4.16).

After getting this type of freestanding structure, TEM observation was performed to determine the structure, and the Au bar could be evaporated by applying a current, as shown in Figures 4.17a and 4.17b. However, it is very easy to damage the graphene immediately after the Au bar is removed because the current is too large for graphene at that point, as shown in Figures 4.17c and 4.17d.



**Figure 4.16** Optical microscopy images of a CVD-grown graphene device: (a) Au bar window after EBL; (b) 10 nm thick Au bar; (c) A  $3 \times 100 \mu\text{m}$  window on the slit after EBL; (d) The freestanding structure (the graphene ribbon covered by Au bar) after 5 min HF etching.

Sometimes, the Au bar has already disconnected from the two electrodes after HF etching, as shown in Figure 4.18, because of the surface tension in the solution process. Current flow was directly applied to these devices to clean the surface and remove Au particles on the surface.



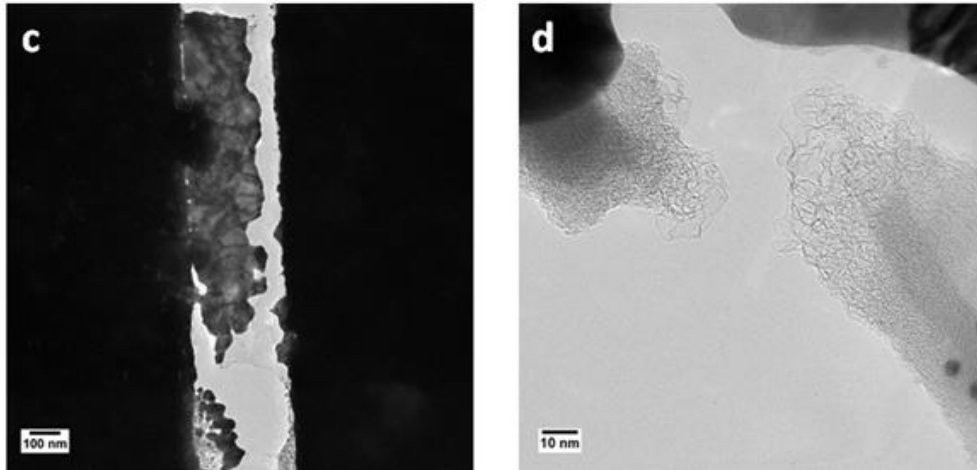


**Figure 4.17** TEM images of freestanding structure of (a) CVD-grown graphene with Au bar protection; (b) Au started melting after applying current flow; (c) Au bar disconnected with two electrodes and graphene was on the bottom part; (d) graphene was broken down after Au was removed.

In general, the Au bar is not easy to remove without damaging graphene. Therefore, we used photoresist to replace the Au bar in the experiment, and the photoresist could be easily removed. The success ratio was very low when we used acetone to remove the photoresist because of surface tension. We therefore chose  $H_2$  plasma in mild conditions to remove the photoresist without damaging graphene.

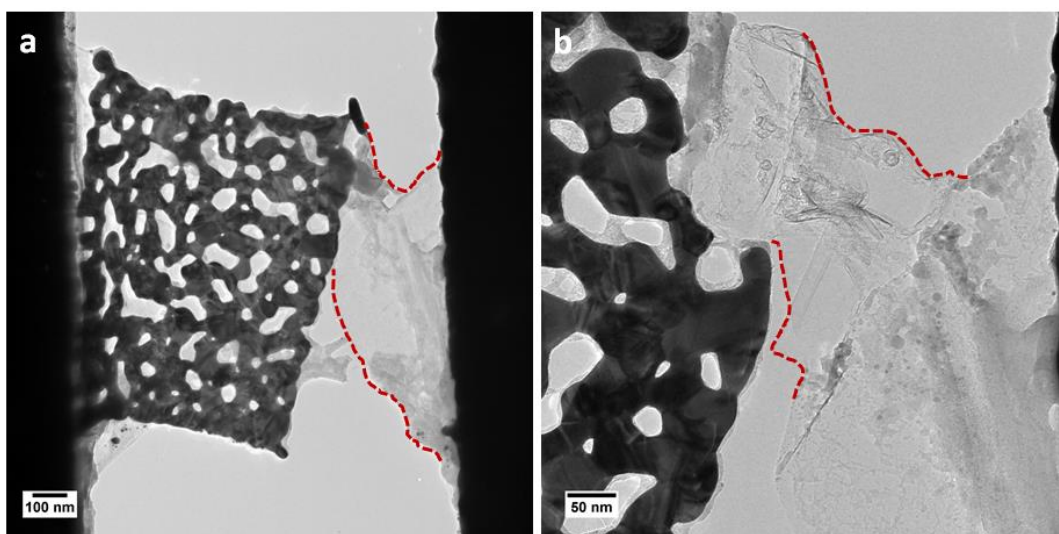


**Figure 4.18** TEM images of freestanding CVD-grown graphene with Au bar (a) after

HF etching and (b) after current annealing.

We used spin coating to deposit an approximately 500 nm thick PMMA film on the surface of a substrate and then gently placed the substrate on the surface of the buffered HF solution without immersing the substrate in the solution for 10 min. In this case, HF only reacted with SiO<sub>2</sub> on the slit part from the back side and graphene was fully protected by PMMA from the top side.

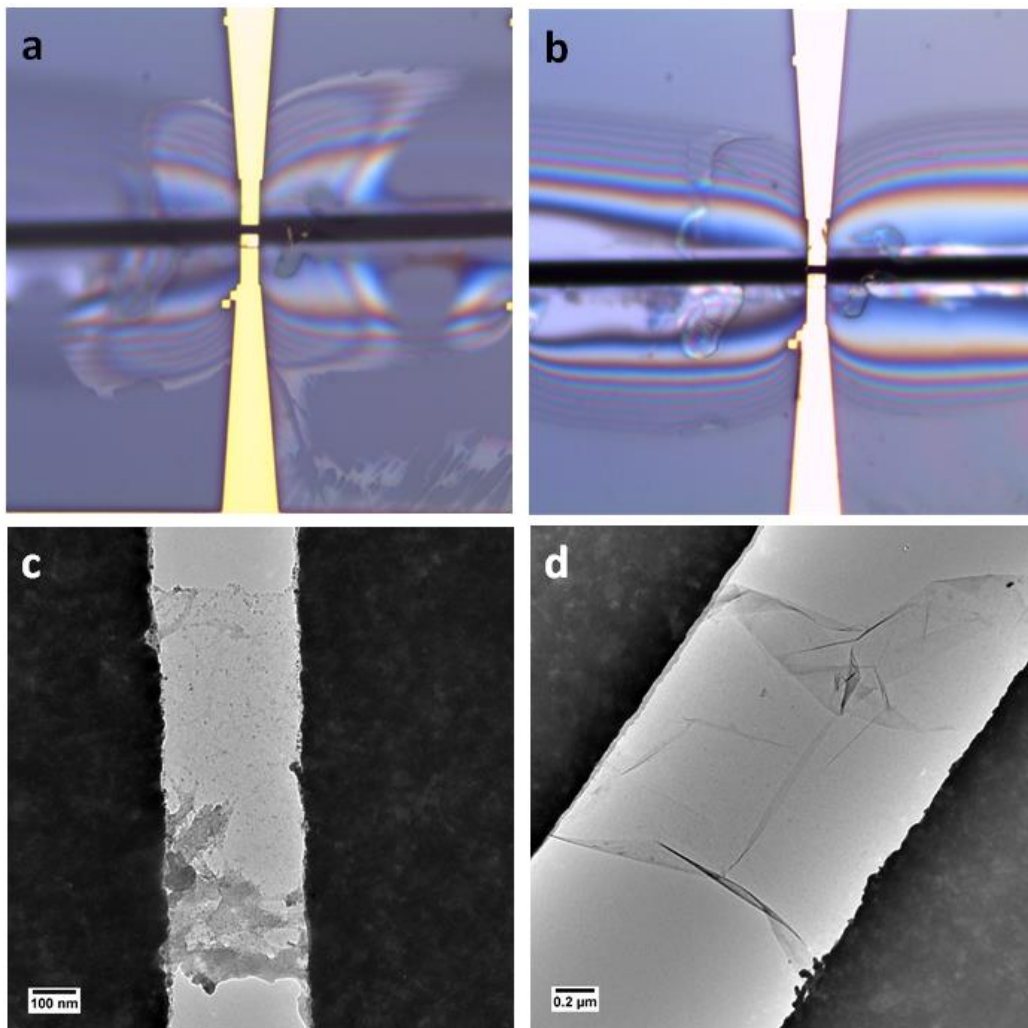


**Figure 4.19** Optical microscopy images of an exfoliated graphene device (a) after 10 min HF etching with PMMA protection and (b) PMMA was removed after 60 min H<sub>2</sub> plasma treatment; TEM images of freestanding (c) CVD-grown graphene and (d) exfoliated graphene structures by PMMA protection method.

As shown in Figure 4.19, this approach increased the success ratio to more than 50%. Because we do not want graphene to be damaged during H<sub>2</sub> plasma treatment, the conditions and the time of the treatment will be controlled. The treatment may result in some PMMA residues remaining on the graphene; these residues will be removed in the subsequent procedure.

## 4.4 In-situ TEM characterization of freestanding structures

### 4.4.1 Preparation for in-situ TEM characterization

To study the correlation between edge structures and electrical properties of GNRs, it is necessary to perform electrical measurements inside TEM. Therefore a home-developed TEM holder was used to conduct these experiments (Figure 4.20).

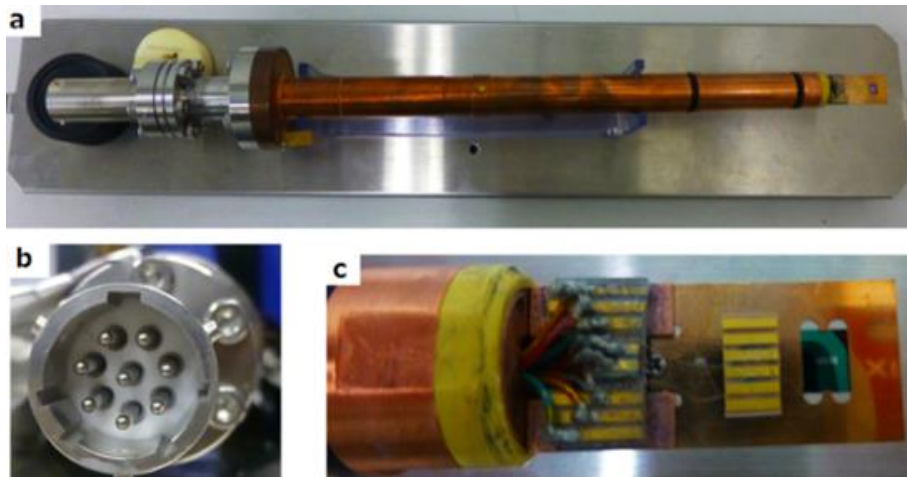


**Figure 4.20** (a) The home-developed TEM holder for in-situ TEM characterization; (b) The bottom connector; (c) The top electrodes pads with a fixed substrate on the copper chip.

The prepared freestanding devices on Si substrates were fixed on the copper chip and connected with eight electrodes pads on the holder by a wire-bonder (WEST-BOND). The eight pads are connected with eight terminals in the bottom connector by electrical wires inside of the holder. We used a nanovoltmeter and a

AC/DC current source (KEITHLEY-2400) for the characterization of electronic properties.

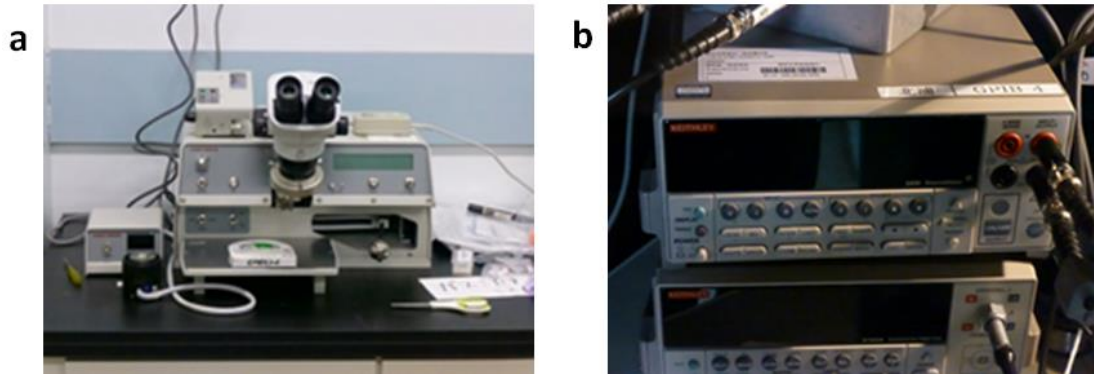


**Figure 4.21** (a) Wire-bonder (WEST-BOND); (b) Constant-current/voltage source (KEITHLEY-2400).

#### 4.4.2 Focused electron beam sculpting

The prepared freestanding graphene device was assembled in our home-developed TEM holder by wire-boding for in-situ characterization. The freestanding graphene was gradually sculpted by a focused electron beam in TEM, and current was applied between the source and drain to keep Joule heating that can avoid the accumulation of amorphous carbon and remove the impurity on the graphene surface. During this process, width-dependent resistance, I-V, and conductance differential properties were investigated in TEM. We observed a significant increase in resistance and found that semiconducting behavior became more dominant with decreasing GNR width.

The exfoliated graphene used in this experiment was tested by Raman spectroscopy to identify the number of layers, and usually, a monolayer of graphene will be used in the following experiment. A typical TEM image of the prepared freestanding graphene is presented in Figure 4.22a and shows a 432 nm wide monolayer graphene with some photoresist residues and amorphous carbon on the surface. These photoresist residues and amorphous carbon will be removed in the subsequent Joule heating, which also reduced contact resistance. During the cleaning process by Joule

heating, the graphitization of amorphous carbon was observed and the graphitized materials formed small graphene islands. The cleaned freestanding graphene devices were further patterned by focused TEM electron beam at an acceleration voltage of 120 kV or 200 kV and progressively sculpted to widths less than 10 nm by knock-on damage of carbon atoms under electron beam irradiation [21, 22]. During the sculpting, Joule heating was continued to prevent the electron beam-induced amorphous carbon contamination [23] and the healing of atomic defects [24].

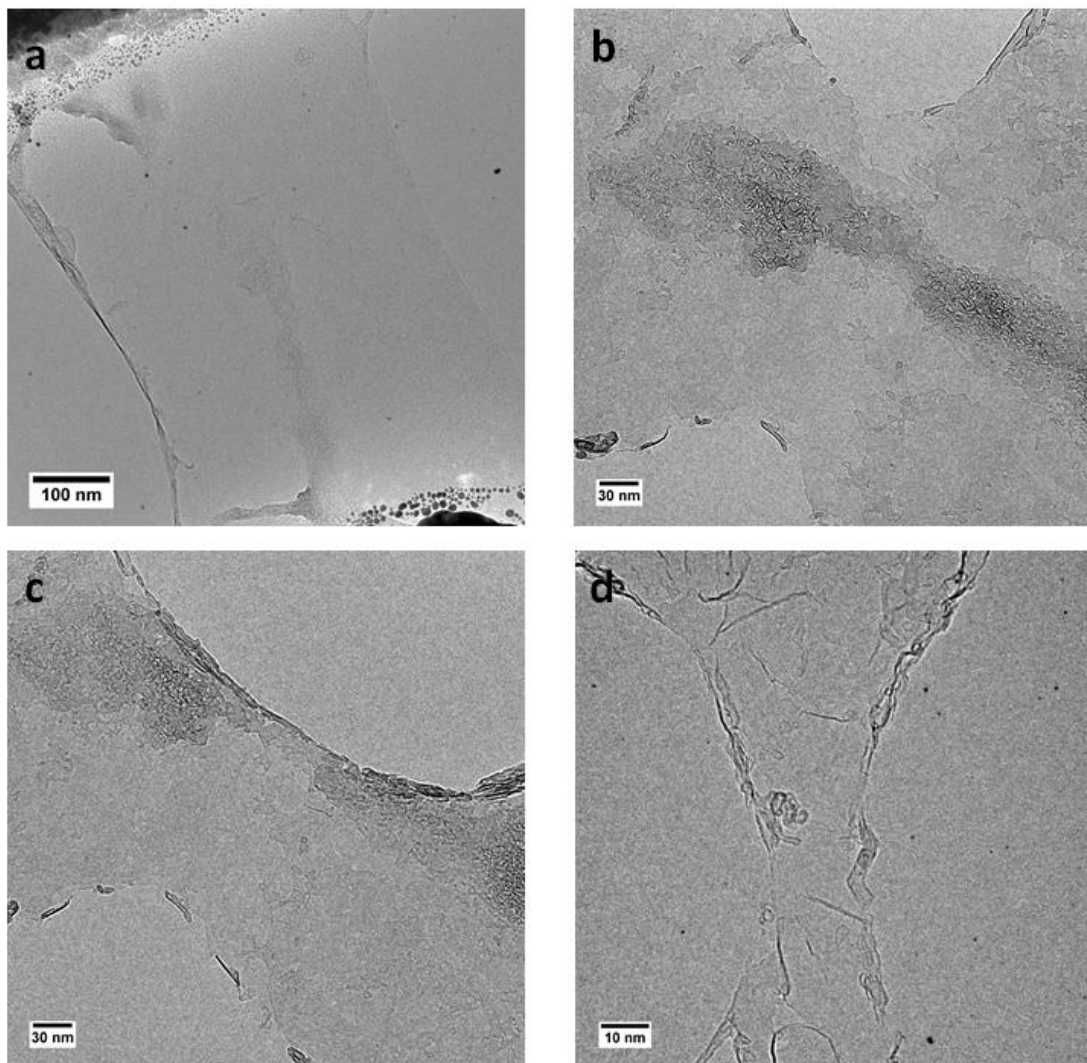


**Figure 4.22** TEM images of a freestanding exfoliated graphene after several steps electron beam sculpting: (a) original structure, (b) (c) (d) beam sculpting from two edges until the width reduced to 18.8 nm.

As we can see in Figure 4.22d, the surface of the graphene is clean with some folded region, in particular, around the edges. The closed-up image shown in Figure 4.23a clearly demonstrates the appearance of lattice fringe without amorphous contaminations, indicating that Joule heating have contributed to realize the clean surface. The Fourier-transformed image of Figure 4c shows spots with 6-fold symmetry, and d-value of the spots corresponds to (110) plane of graphene (0.21 nm).

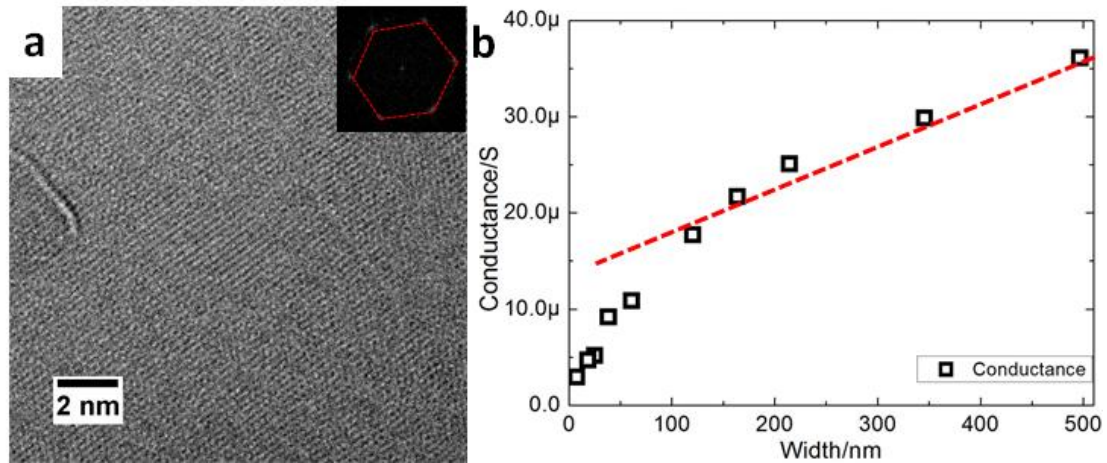


**Figure 4.23** (a) A close-up TEM image of the freestanding graphene after patterning to nanoribbon with an inset of corresponding FFT image; (b) Conductance as a function of width from 5 nm to 500 nm, red line: fitting line of the metallic behavior.

In the narrowing-down process, we measured low-bias conductance as a function of width from 500 to 5 nm (Figure 4.23b). Large-width region in Figure 4.23b is almost linear, and the slope of the liner region gives conductivity of the suspended graphene, 700 S/m, which is consistent to reported conductivity of two-terminal device of graphene. The deviation from the straight line is prominent at small-width region, indicating that conductivity of graphene is reduced by bandgap when width of graphene is smaller than ca. 150 nm. Theoretical calculation of armchair GNR bandgap using a first principle many-body Green's function approach under GW approximation has shown that the bandgap,  $E_g$ , is described by the following formula,  $E_g = a/(w+2.4+\delta)$ , where  $a$  and  $\delta$  are parameters ranges from 14.6 ~ 44.4 eVÅ and 1.8 ~ 2.9 Å, respectively, and  $w$  corresponds to width of GNR [25]. Based on this

equation, width of 150 nm yields  $E_g$  of 9.7 ~ 29.5 meV. We measured conductance using bias voltage ( $V_b$ ) of 10 mV at room temperature, and the low-bias conductance can be affected when GNR's bandgap is comparable to  $V_b$  and thermal energy of room temperature (26 meV) [26]. The observed deviation from the linear relation therefore results from successful observation of intrinsic bandgap of the GNR.

#### 4.4.3 Joule heating and electrical measurement

Combination of electron-beam sculpting and Joule-heating-induced vaporization of carbon atoms has led successful fabrication of an ultra-narrow graphene with width of 1.6 nm. Electron-beam sculpting alone cannot yield the ultra-narrow structure because spatial drift of a sample during the sculpting disturbs precise positioning of the sample. Figure 4.24a shows a TEM image of the ultra-narrow graphene. The narrowest part of the graphene is much narrower than remaining parts, and the remaining parts can be considered as electrodes connected to the narrowest part. In this case, electronic transport is dominated by the 1.6 nm wide structure. Figure 4.24b shows the current and differential conductance as a function of bias voltage, in which the differential conductance of the GNR is in close proximity to zero when the bias voltage is near zero. It was noticed that the value of  $dI/dV$  at zero bias voltage is not zero, which might be contributed by the back gate leak current (about  $10^{-12}$  A) from substrate.

Observation of nonlinear transport characteristics is one of approaches to probe the transport gap of GNRs [27]. In the transport gap regime, transport through the GNR at finite bias voltage shows a strong nonlinear I-V characteristic when gate voltage is near the charge neutrality point of the GNR, and the transport gap can be estimated as half of nonlinear gap ( $\Delta V$ ) [27]. The  $\Delta V$  is estimated to be 800 meV based on the I-V curve shown in Figure 4.24b, indicating that the 1.6 nm wide structure has a transport gap of about 400 meV. The observed transport gap of 400 meV is the largest among GNRs measured through transport measurements. The GW calculation have shown that 1.6 nm armchair GNRs and zig-zag GNR have bandgap of 740 ~ 2100 meV and 1200 meV [25], respectively, which are larger than the observed value. In our

experiment, length of the GNR is short and large graphene part connected to the GNR may affect electronic structure of the channel part, which probably affects the transport gap measurement.

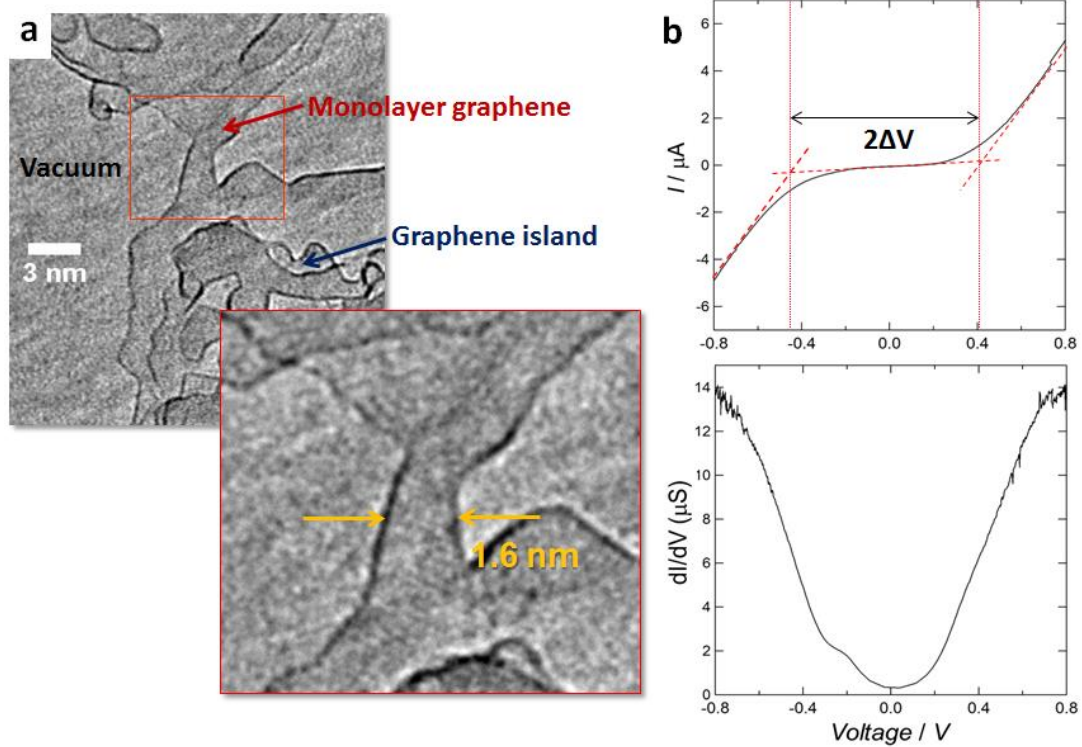


**Figure 4.24** (a) TEM images of a 1.6 nm wide graphene nanostructure; (b) I-V curve and differential conductance of this 1.6 nm structure with a nonlinear regime  $\Delta V \approx 800$  meV.

In addition to the structure discussed above, we obtained other types of structures due to the reconstruction at high temperature, as shown in Figures 4.25a and 4.25b. A 0.4 nm wide nanostructure was obtained, showing dark contrast on the edges and some encapsulated structures at both ends (Figure 4.25a). The differential conductance curve shows that this is still a metallic structure, similar to a very thin metallic single-wall CNT.

The final structure shown in Figure 4.25b is a 7.8 nm wide ribbon structure with fullerenes and folded graphene region on the edges. This structure still exhibited metallic properties in the differential conductance curve, which may be caused by the

influence of the complicated edge structures. The folded graphene and fullerene encapsulated edges may increase the conductance and limit the bandgap opening. However, detailed studies of structures and transport properties for these types of composite structures are too difficult.

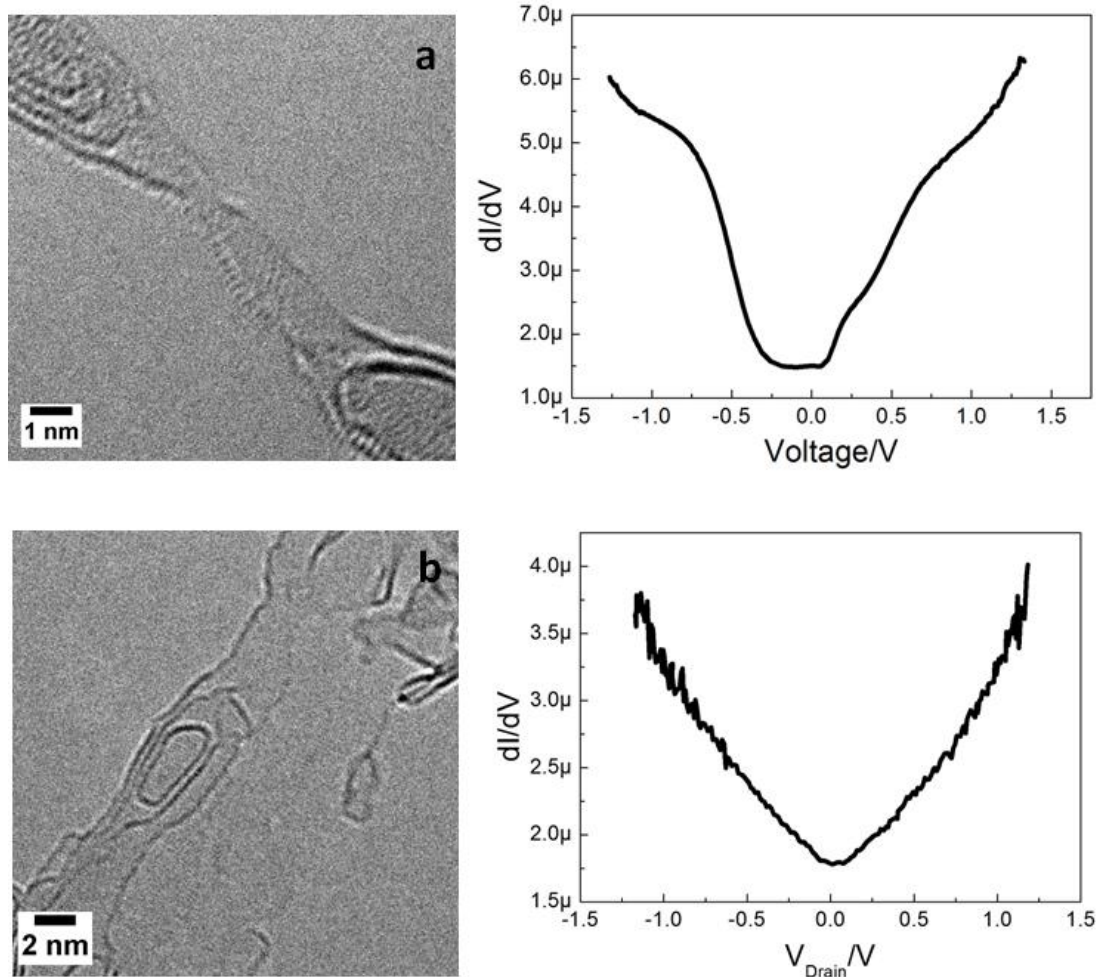


**Figure 4.25** TEM image and differential conductance of (a) a 0.4 nm wide structure and (b) a 7.8 nm wide structure.

## 4.5 Conclusions

In this part of my work, we reported two types of new experimental techniques to fabricate freestanding graphene devices. Using electron beam sculpting and Joule heating in TEM,  $\sim 10$  nm wide GNR structures can be obtained. In the narrowing down process, the conductance of GNRs behaved nonlinearly as a function of width,

indicating the opening of the bandgap. I-V and conductance differential characteristics were performed with a known structure. In this work, the thinnest structure obtained was approximately 1.6 nm wide, with an estimated transport gap of approximately 400 meV. The observed transport gap of 400 meV is the largest among GNRs measured through transport measurements, and this method can be used to study the intrinsic electronic properties of GNRs. The presented methodology could be used in the future to correlate the electronic properties with known structures in other two-dimensional materials such as transition metal dichalcogenides.

## References

1. M. Y. Han, B. Ozyilmaz, Y. Zhang, P. Kim. Energy band-gap engineering of graphene nanoribbons. *Physical Review Letters* **2007**, 98 (20), 206805.
2. Y. -W. Son, M. L. Cohen, S. G. Louie. Energy gaps in graphene nanoribbons. *Physical Review Letter* **2006**, 97, 216803.
3. D. H. Choi, Q. Wang, Y. Azuma, Y. Majima, J. H. Warner, Y. Miyata, H. Shinohara, R. Kitaura. Fabrication and characterization of fully flattened carbon nanotubes: A new graphene nanoribbon analogue. *Scientific Reports* **2013**, 3, 1617.
4. J. W. Bai, X. F. Duan, Y. Huang. Rational fabrication of graphene nanoribbons using a nanowire etch mask. *Nano Letters* **2009**, 9, 2083-2087.
5. D. V. Kosynkin, A. L. Higginbotham, A. Sinitskii, J. R. Lomeda, A. Dimiev, B. K. Price, J. M. Tour. Longitudinal unzipping of carbon nanotubes to form graphene nanoribbons. *Nature* **2009**, 458, 872-875.
6. L. Y. Jiao, L. Zhang, X. R. Wang, G. Diankov, H. J. Dai. Narrow graphene nanoribbons from carbon nanotubes. *Nature* **2009**, 458, 877-880.
7. M. Sprinkle, M. Ruan, Y. Hu, J. Hankinson, M. Rubio-Roy, B. Zhang, X. Wu, C. Berger, W. A. de Heer. Scalable templated growth of graphene nanoribbons on SiC. *Nature Nanotechnology* **2010**, 5, 727-731.
8. J. Cai, P. Ruffieux, R. Jaafar, M. Bieri. T. Braun, S. Blankenburg, M. Muoth, A. P. Seitsonen, M. Saleh, X. Feng, K. Mullen, R. Fasel. Atomically precise bottom-up fabrication of graphene nanoribbons. *Nature* **2010**, 466, 470-473.
9. K. Nakada, M. Fujita, G. Dresselhaus, M. S. Dresselhaus. Edge state in graphene ribbons: Nanometer size effect and edge shape dependence. *Physical Review B* **1996**, 54 (24), 17954-1961.
10. Y. -T. Zhang, H. Jiang, Q. Sun, X. C. Xie. Spin polarization and giant magnetoresistance effect induced by magnetization in zigzag graphene nanoribbons. *Physical Review B* **2010**, 81, 165404.
11. X. Li, X. Wang, L. Zhang, S. Lee, H. Dai. Chemically derived, ultrasmooth graphene nanoribbon semiconductors. *Science* **2008**, 319, 1229-1232

12. Z. J. Qi, J. A. Rodríguez-Manzo, A. R. Botello-Méndez, S. J. Hong, E. A. Stach, Y. W. Park, J.-C. Charlier, M. Drndić, A. T. C. Johnson. Correlating atomic structure and transport in suspended graphene nanoribbons. *Nano Letters* **2014**, 14(8), 4238-4244.
13. B. Sommer, J. Sonntag, A. Ganczarczyk, D. Braam, G. Prinz, A. Lorke, M. Geller. Electron-beam induced nano-etching of suspended graphene. *Scientific Reports* **2014**, 5, 7781.
14. O. Hod, G. E. Scuseria. Electromechanical properties of suspended graphene nanoribbons. *Nano Letters* **2009**, 9(7), 2619-2622.
15. C. M. Orofeo, H. Hibino, K. Kawahara, Y. Ogawa, M. Tsuji, K. Ikeda, S. Mizuno, H. Ago. Influence of Cu metal on the domain structure and carrier mobility in single-layer graphene. *Carbon* **2012**, 50, 2189-2196.
16. A. Castellanos-Gomez, M. Buscema, R. Molenaar, V. Singh, L. Janssen, H. S J van der Zant, G. A Steele. Deterministic transfer of two-dimensional materials by all-dry viscoelastic stamping. *2D Materials* **2014**, 1, 011002.
17. B. Song, G. F. Schneider, Q. Xu, G. Pandraud, C. Dekker, H. Zandbergen. Atomic-scale electron-beam sculpting of near-defect-free graphene nanostructures. *Nano Letters* **2011**, 11, 2247-2250.
18. J. Y. Huang, F. Ding, B. Yakobson, P. Lu, L. Qi, J. Li. In situ observation of graphene sublimation and multi-layer edge reconstructions. *PNAS* **2009**, 106 (25), 10103-10108.
19. B. Westenfelder, J. C. Meyer, J. Biskupek, S. Kurasch, F. Scholz, C. E. Krill, U. Kaiser. Transformations of carbon adsorbed on graphene substrates under extreme heat. *Nano Letters* **2011**, 11, 5123-5127.
20. Q. Wang, X. Guo, L. Cai, Y. Cao, L. Gan, S. Liu, Z. Wang, H. Zhang, L. Li. TiO<sub>2</sub>-decorated graphenes as efficient photoswitches with high oxygen sensitivity. *Chemical Science* **2011**, 2, 1860-1864.
21. B. Song, G. F. Schneider, Q. Xu, G. Pandraud, C. Dekker, H. Zandbergen. Atomic-scale electron-beam sculpting of near-defect-free graphene nanostructures. *Nano Letters* **2011**, 11, 2247-2250.

22. Y. Lu, C. A. Merchant, M. Drndic, A. T. C. Johnson. In situ electronic characterization of graphene nanoconstrictions fabricated in a transmission electron microscope. *Nano Letters* **2011**, 11, 5184-5188.
23. J. C. Meyer, F. Eder, S. Kurasch, V. Skakalova, J. Kotakoski, H. J. Park, S. Roth, A. Chuvilin, S. Eyhusen, G. Benner, A. V. Krasheninnikov, U. Kaiser. Accurate measurement of electron beam induced displacement cross sections for single-layer graphene. *Physical Review Letters* **2012**, 108, 196102.
24. T. Gao, Y. Gao, C. Chang, Y. Chen, M. Liu, S. Xie, K. He, X. Ma, Y. Zhang, Z. Liu. Atomic-scale morphology and electronic structure of manganese atomic layers underneath epitaxial graphene on SiC (0001). *ACS Nano* **2012**, 6, 6562–6568.
25. L. Yang, C. -H. Park, Y. -W. Son, M. L. Cohen, S. G. Louie. Quasiparticle energies and band gaps in graphene nanoribbons. *Physical Review Letters* **2007**, 99, 186801.
26. M. Y. Han, P. Kim. Graphene nanoribbon devices at high bias. *Nano Convergence* **2014**, 1, 1.
27. M. Y. Han, J. C. Brant, P. Kim. Electron transport in disordered graphene nanoribbons. *Physical Review Letters* **2010**, 104, 056801.

## Conclusions

To achieve a simple and low-cost preparation of GNRs, we developed a solution-based method for the synthesis of high-quality FNTs (GNR analogs) and characterized the obtained FNT using AFM, TEM, and Raman measurements. The AFM images showed a clear height plane in the middle regions of FNTs and two higher edges, indicating the barbell-like cross section of FNTs. An obvious D feature due to the edge effect at the nanoscale was observed in the Raman spectrum of an isolated FNT. The observed G feature was much stronger than the 2D feature, consistent with a few-layer graphene structure. In general, TEM observations showed that FNTs with widths of approximately 10 ~ 50 nm were obtained. In addition, the utilization of H<sub>2</sub> plasma for purification in mild conditions and edges control of FNTs were performed with an etching ratio of approximately 60%. The electronic characteristics of fewer-layer FNTs exhibited typical ambipolar transport behavior with a Dirac point. We also observed the conductance shoulders originating from FNT subband at 9 K and mobility changes at different temperatures due to the phonon scattering effects.

FNTs provide unique inner space with a barbell-like cross section that is dramatically different from CNTs. FNTs and C<sub>60</sub> fullerenes are composited as a new type of hybrid nanostructures with unique structures. The validity of rounded hollow space at the close edges of FNTs was identified by the TEM observations and EELS measurements. A brand new hybrid material (C<sub>60</sub>@FNTs), where C<sub>60</sub> molecules are aligned in one-dimensional fashion at the closed edges of FNTs, is provided by the intercalation of C<sub>60</sub> molecules into the edge space. Furthermore, C<sub>60</sub> molecules packed in a two-dimensional fashion has been originally realized in the middle flattened region of FNTs. We performed TEM observations and image simulation on the basis of the multi-slice method to study these structures. This new type of nanocarbon materials exhibit quite fascinating structures on the basis of TEM observations. Additionally, the experimental results declare that FNTs can be intercalated with various atoms and molecules, enabling the potential of preparing new kinds of novel

hybrid materials on the basis of FNTs.

To investigate the intrinsic properties of GNRs, we demonstrated two types of new experimental technologies to fabricate freestanding graphene and GNRs devices. Utilization of electron beam sculpting and Joule heating in TEM, ~10 nm wide GNR structures can be obtained. In the narrowing down process, the conductance of GNRs behaved nonlinearly as a function of width, which indicated the opening of bandgap. Output and conductance differential characteristics were performed with a known structure. In this work, the thinnest structure was approximately 1.6 nm wide, with an estimated transport gap of approximately 400 meV. The observed transport gap of 400 meV is the largest among GNRs measured through transport measurements, and this method can be used to study the intrinsic electronic properties of GNRs. The presented methodology could be used in the future to correlate electronic properties with a known structure in two-dimensional materials such as transition metal dichalcogenides.

## Acknowledgments

First and foremost, I would like to express my sincerely gratitude to my supervisor, Prof. Hisanori Shinohara. He supported me not only by his supervision and his insight in science, but also by sharing his non science-related ideas. He helped me come up with the thesis topic and guided my research direction. I specially thank him for confidence, trust, and his encouragement in every early-bird meetings. His invaluable support and care made it possible to complete this study.

Very special thanks go out to Assoc. Prof. Ryo Kitaura for the valuable suggestions and enjoyable discussions in weekly meetings. He provided me with scientific and technical supports and became not only a mentor but also a friend. During the most difficult times in the experiment, he supported me on preparing the in-situ TEM related equipment and on the very long CS-TEM observation. I doubt that I will never be able to convey my appreciation fully, but I owe him my gratitude.

I further extend my appreciations to Assoc. Prof. Yasumitsu Miyata (currently in Tokyo Metropolitan University) and Asst. Prof. Haruka Omachi for their help. They gave me many valuable suggestions on preparing this study. I also thank the former postdocs Dr. Jinying Zhang and Dr. Zhiyong Wang for their help.

Moreover, I must give my appreciation to Prof. Yutaka Majima and Asst. Prof. Yasuo Azuma in Tokyo Institute of Technology. They gave the supplement of EBL and probe station for the basic experiment of this study. I thank Assoc. Prof. Kosuke Nagashio in the University of Tokyo, who guided me on the specific technique on dry transfer of graphene. I should also thank the technical assistant from Dr. Shigeo Arai and Dr. Yuta Yamamoto for the CS-TEM support.

Dozens of people have helped and taught me immensely in Shinohara Lab. The cultural diversity of the group always gave me refreshing support. Special thanks to Ms. Miho Fujihara who was my tutor in the first year in Japan and helped a lot in Japanese culture and my experiments; Mr. Daeheon Choi who taught me the basic methods of the FNT-related experiments; Mr. Shoji Suzuki who contributed in the in-situ TEM experiment; Mr. Yuki Sasaki who helped a lot of times in the plasma and

CVD process; and Mr. Yusuke Nakanishi who helped me a lot in the official documents and other things during the preparation of doctoral defense. I also thank Ms. Chen Zhao, Dr. Yun Sun, Dr. Hongen Lim and Mr. Sihan Zhao for their help in the experiment and studying Japanese and daily life.

Many thanks also to all my friends and colleagues who made my life so full and happy by their warm friendship and understanding during those past years. They always give me the confidence and encouragement.

I also gratefully acknowledge that the scholarship provided by the China Scholarship Council supported my study in Japan.

My special thanks to my parents for their loving support and encouragement. Furthermore, I want to thank my husband, Dr. Yongpeng Tang, for his support all the time.

Finally, I thanks to all of you who have contributed to this study.

*Qing Wang*

Nagoya University

July, 2015

## List of Publications

### Main publications

1. Fabrication and in-situ TEM characterization of freestanding graphene nanoribbons and their devices

Q. Wang, R. Kitaura, S. Suzuki, Y. Yamamoto, S. Arai, H. Shinohara

Submitted to ACS Nano.

2. Synthesis and TEM structural characterization of C<sub>60</sub>-flattened carbon nanotube nanopeapods

Q. Wang, R. Kitaura, Y. Yamamoto, S. Arai, H. Shinohara

*Nano Research* **2014**, 7 (12), 1843.

### Reference publications

1. N-methylation of amines with methanol at room temperature

V. N. Tsarev, Y. Morioka, J. Caner, Q. Wang, R. Ushimaru, A. Kudo, H. Naka, S. Saito

*Organic letters* **2015**, 17, 2530.

2. Synthesis of refractory conductive niobium carbide nanowires within the innerspace of carbon nanotube templates

K. Kobayashi, R. Kitaura, Q. Wang, I. Wakamori, H. Shinohara, S. Anada, T. Nagase, T. Saito, M. Kiyomiya, H. Yasuda

*Applied Physics Express* **2014**, 7, 015101.

3. Photocatalytic application of nanosized CdS immobilized onto functionalized MWCNTs

D. Chronopoulos, N. Karousis, S. Zhao, Q. Wang, H. Shinohara, N. Tagmatarchis

*Dalton Transactions* **2014**, 43, 7429.

4. Fabrication and characterization of fully flattened carbon nanotubes: a new graphene nanoribbon analogue

D. Choi, Q. Wang, Y. Azuma, Y. Majima, Y. Miyata, J.H. Warner, H. Shinohara, R. Kitaura

*Scientific Reports* **2013**, 3, 1617.